Biopsy needles localization and tracking methods in 3d medical ultrasound with ROI-RANSAC-KALMAN

Yue Zhao

N° d'ordre : 2014ISAL0015 Année 2014°

THÈSE

Biopsy Needles Localization and Tracking Methods in 3D Medical Ultrasound with ROI-RANSAC-KALMAN

Délivrée par

L'INSTITUT NATIONAL DES SCIENCES APPLIQUEES DE LYON

Pour obtenir

DIPLÔME DE DOCTORAT

École doctorale:

MECANIQUE, ENERGETIQUE, GENIE CIVIL, ACOUSTIQUE

Soutenue publiquement le 05 Février 2014 par

Yue ZHAO

Jury

Directeurs de thèse :

Christian CACHARD	Professeur des Universités, Université Claude Bernard, Lyon I
Hervé LIEBGOTT	Maître de Conférences, HDR, Université Claude Bernard, Lyon I

Rapporteurs:

Pascal HAIGRON	Professeur des Universités, Université de Rennes I
Jean-Marc GIRAULT	Maître de Conférences, HDR Université François-Rabelais, Tours

Examinateurs:

Didier VRAY	Professeur des Universités, INSA de Lyon
Laurent SARRY	Professeur des Universités, Université Clermont-Ferrand

INSA Direction de la Recherche - Écoles Doctorales – Quinquennal 2011-2015

SIGLE	ECOLE DOCTORALE	NOM ET COORDONNEES DU RESPONSABLE
CHIMIE	**CHIMIE DE LYON** **http://www.edchimie-lyon.fr** Insa : R. GOURDON	M. Jean Marc LANCELIN Université de Lyon – Collège Doctoral Bât ESCPE 43 bd du 11 novembre 1918 69622 VILLEURBANNE Cedex Tél : 04.72.43 13 95 directeur@edchimie-lyon.fr
E.E.A.	**ELECTRONIQUE, ELECTROTECHNIQUE, AUTOMATIQUE** **http://edeea.ec-lyon.fr** Secrétariat : M.C. HAVGOUDOUKIAN eea@ec-lyon.fr	M. Gérard SCORLETTI Ecole Centrale de Lyon 36 avenue Guy de Collongue 69134 ECULLY Tél : 04.72.18 65 55 Fax : 04 78 43 37 17 Gerard.scorletti@ec-lyon.fr
E2M2	**EVOLUTION,ECOSYSTEME, MICROBIOLOGIE, MODELISATION** **http://e2m2.universite-lyon.fr** Insa : H. CHARLES	Mme Gudrun BORNETTE CNRS UMR 5023 LEHNA Université Claude Bernard Lyon 1 Bât Forel 43 bd du 11 novembre 1918 69622 VILLEURBANNE Cédex Tél : 06.07.53.89.13 e2m2@ univ-lyon1.fr
EDISS	**INTERDISCIPLINAIRE SCIENCES-SANTE** **http://www.ediss-lyon.fr** Sec : Samia VUILLERMOZ Insa : M. LAGARDE	M. Didier REVEL Hôpital Louis Pradel Bâtiment Central 28 Avenue Doyen Lépine 69677 BRON Tél : 04.72.68.49.09 Fax :04 72 68 49 16 Didier.revel@creatis.uni-lyon1.fr
INFOMATHS	**INFORMATIQUE ET MATHEMATIQUES** **http://infomaths.univ-lyon1.fr** Sec :Renée EL MELHEM	Mme Sylvie CALABRETTO Université Claude Bernard Lyon 1 INFOMATHS Bâtiment Braconnier 43 bd du 11 novembre 1918 69622 VILLEURBANNE Cedex Tél : 04.72. 44.82.94 Fax 04 72 43 16 87 infomaths@univ-lyon1.fr
Matériaux	**MATERIAUX DE LYON** **http://ed34.universite-lyon.fr** Secrétariat : M. LABOUNE PM : 71.70 –Fax : 87.12 Bat. Saint Exupéry Ed.materiaux@insa-lyon.fr	M. Jean-Yves BUFFIERE INSA de Lyon MATEIS Bâtiment Saint Exupéry 7 avenue Jean Capelle 69621 VILLEURBANNE Cedex Tél : 04.72.43 83 18 Fax 04 72 43 85 28 Jean-yves.buffiere@insa-lyon.fr
MEGA	**MECANIQUE, ENERGETIQUE, GENIE CIVIL, ACOUSTIQUE** **http://mega.ec-lyon.fr** Secrétariat : M. LABOUNE PM : 71.70 –Fax : 87.12 Bat. Saint Exupéry mega@insa-lyon.fr	M. Philippe BOISSE INSA de Lyon Laboratoire LAMCOS Bâtiment Jacquard 25 bis avenue Jean Capelle 69621 VILLEURBANNE Cedex Tél :04.72 .43.71.70 Fax : 04 72 43 72 37 Philippe.boisse@insa-lyon.fr
ScSo	**ScSo*** **http://recherche.univ-lyon2.fr/scso/** Sec : Viviane POLSINELLI Brigitte DUBOIS Insa : J.Y. TOUSSAINT	M. OBADIA Lionel Université Lyon 2 86 rue Pasteur 69365 LYON Cedex 07 Tél : 04.78.77.23.86 Fax : 04.37.28.04.48 Lionel.Obadia@univ-lyon2.fr

*ScSo : Histoire, Géographie, Aménagement, Urbanisme, Archéologie, Science politique, Sociologie, Anthropologie

Abstract

In medical examinations and surgeries, minimally invasive technologies are getting used more and more often. Some specially designed surgical instruments, like biopsy needles, or electrodes are operated by radiologists or robotic systems and inserted in human's body for extracting cell samples or delivering radiation therapy. To reduce the risk of tissue injury and facilitate the visual tracking, some medical vision assistance systems, as for example, ultrasound (US) systems can be used during the surgical procedure.

We have proposed to use the 3D US to facilitate the visualization of the biopsy needle, however, due to the strong speckle noise of US images and the large calculation load involved as soon as 3D data are involved, it is a challenge to locate the biopsy needle accurately and to track its position in real time in 3D US. In order to solve the two main problems above, we propose a method based on the RANSAC algorithm and Kalman filter. In this method, a region of interest (ROI) has been limited to robustly localize and track the position of the biopsy needle in real time.

The ROI-RK method consists of two steps: the initialization step and the tracking step. In the first step, a ROI initialization strategy using Hessian based line filter measurement is implemented. This step can efficiently reduce the speckle noise of the ultrasound volume, and enhance line-like structures as biopsy needles. In the second step, after the ROI is initialized, a tracking loop begins. The RK algorithm can robustly localize and track the biopsy needles in a dynamic situation. The RANSAC algorithm is used to estimate the position of the micro-tools and the Kalman filter helps to update the ROI and auto-correct the needle localization result. Because the ROI-RK method is involved in a dynamic situation, a motion estimation strategy is also implemented to estimate the insertion speed of the biopsy needle.

3D US volumes with inhomogeneous background have been simulated to evaluate the performance of the ROI-RK method. The method has been tested under different conditions, such as insertion orientations angles, and contrast ratio (CR). The localization accuracy is within 1 mm no matter what the insertion direction is. Only when the CR is very low, the proposed method could fail to track because of an incomplete ultrasound imaging of the needle.

Another methodology, *i.e.* RANSAC with machine learning (ML) algorithm has been presented. This method aims at classifying the voxels not only depending on their intensities, but also using some structure features of the biopsy needle. The simulation results show that the RANSAC with ML algorithm can separate the needle voxels and background tissue voxels with low CR.

Key words: 3D, ultrasound, biopsy needle, Kalman, RANSAC, speckle tracking, classification, machine learning

Résumé

Dans les examens médicaux et les actes de thérapie, les techniques minimalement invasives sont de plus en plus utilisées. Des instruments comme des aiguilles de biopsie, ou des électrodes sont utilisés pour extraire des échantillons de cellules ou pour effectuer des traitements. Afin de réduire les traumatismes et de faciliter le suivi visuelle de ces interventions, des systèmes d'assistance par imagerie médicale, comme par exemple, par l'échographie 2D, sont utilisés dans la procédure chirurgicale.

Nous proposons d'utiliser l'échographie 3D pour faciliter la visualisation de l'aiguille, mais en raison de l'aspect bruité de l'image ultrasonore (US) et la grande quantité de données d'un volume 3D, il est difficile de trouver l'aiguille de biopsie avec précision et de suivre sa position en temps réel. Afin de résoudre les deux principaux problèmes ci-dessus, nous avons proposé une méthode basée sur un algorithme RANSAC et un filtre de Kalman. De même l'étude est limitée à une région d'intérêt (ROI) pour obtenir une localisation robuste et le suivi de la position de l'aiguille de biopsie en temps réel.

La méthode ROI-RK se compose de deux étapes: l'étape d'initialisation et l'étape de suivi. Dans la première étape, une stratégie d'initialisation d'une ROI en utilisant le filtrage de ligne à base de matrice de Hesse est mise en œuvre. Cette étape permet de réduire efficacement le bruit de granularité du volume US, et de renforcer les structures linéaires telles que des aiguilles de biopsie. Dans la deuxième étape, après l'initialisation de la ROI, un cycle de suivi commence. L'algorithme RK localise et suit l'aiguille de biopsie dans une situation dynamique. L'algorithme RANSAC est utilisé pour estimer la position des micro-outils et le filtrage de Kalman permet de mettre à jour la région d'intérêt et de corriger la localisation de l'aiguille. Une stratégie d'estimation de mouvement est également appliquée pour estimer la vitesse d'insertion de l'aiguille de biopsie.

Des volumes 3D US avec un fond inhomogène ont été simulés pour vérifier les performances de la méthode ROI-RK. La méthode a été testée dans des conditions variables, telles que l'orientation d'insertion de l'aiguille par rapport à l'axe de la sonde et le niveau de contraste (CR). La précision de la localisation est de moins de 1 mm, quelle que soit la direction d'insertion de l'aiguille. Ce n'est que lorsque le CR est très faible que la méthode proposée peut échouer dans le suivi d'une structure incomplète de l'aiguille.

Une autre méthode, utilisant l'algorithme RANSAC avec apprentissage automatique a été proposée. Cette méthode vise à classer les voxels en se basant non seulement sur l'intensité, mais aussi sur les caractéristiques de la structure de

l’aiguille de biopsie. Les résultats des simulations montrent que l’algorithme RANSAC avec apprentissage automatique peut séparer les voxels de l’aiguille et les voxels de tissu de fond avec un CR faible.

Mots-clés: 3D, ultrasons, aiguille de biopsie, Kalman, RANSAC, estimation de mouvement, classification, apprentissage automatique

Acknowledgment

First, I would like to sincerely gratitude to my supervisors: professor Christian Cachard and associate professor, HDR Hervé Liebgott, for the continuous support of my Ph.D study and research in Lab CREATIS, for their patience, motivation, and immense knowledge, and for their inspiring guidance during my thesis. It is really a great experience working with them. With their abundant research experience, they show me how to become an independent researcher.

I appreciate professor Pascal Haigron and associate professor, HDR Jean-Marc Girault for reviewing my thesis. I would like to thank professor Didier Vray and professor Laurent Sarry for accepting as the jury of my thesis.

I appreciate the previous Ph.D Marián Uherčík, his experience in programming helped me a lot during my research work.

I would like to thank professor Jan Kybic, who works in Czech Technical University, for his great experience in the domain of machine learning.

I would like to thank all my colleagues in the laboratory for their help during my stay in France. Especially, I appreciate my close and deep friends who courage me for pursuing the Ph.D when time is dark and hard.

I express special thanks to my parents. Even though the distance between us is more than ten thousand kilometers, I can feel their endless love and support. Their encouragement supports me to finish my thesis.

Last but not least, I would like to thank my boyfriend Jianxing for being accompanying the whole time by the plenty love and patience. The stay in France is a precious experience for both of us.

Notations

Abbreviation

1D, 2D, 3D	One-, two-, three-dimensions
ARFI	Acoustic radiation force impulse
CA	Constant accelerating
CMUT	capacitive micro-machined ultrasonic transducer
CR	Contrast ratio
CT	Computer Tomography
CV	Constant velocity
HT	Hough transform
ML	Machine learning
MRI	Magnetic Resonance Imaging
NCC	Normalized cross correlation
PCA	Principal component analysis
PIP	Parallel integral transform
PVA	Polyvinyl alcohol
RANSAC	Random sample consensus
RF	Radio frequency
ROI	Region of interest
ROI-RK	ROI based RANSAC and Kalman
STD	Standard deviation
SVM	Support vector machine
TRUS	Trans Rectal Ultrasound
US	Ultrasound

Mathematical symbols

$\Re^n$	n dimensions Euclidean space
$\Re$	The set of real numbers
$\mathbf{A}$, $\mathbf{B}$, $\mathbf{F}$, $\mathbf{H}$	Matrices
$\mathbf{p}$, $\mathbf{s}$, $\mathbf{u}$, $\mathbf{v}$	Vectors
$\alpha, \beta, \theta, \varphi$	Angles in degree
x, y, z	The Cartesian coordinate
i, j, k	Indicators
J, ζ, η, t	Parameters
$f(\cdot)$, $l(\cdot)$, $q(\cdot)$, $d(\cdot)$, $C(\cdot)$	Functions
$V(\cdot)$	A set of voxels
$\lvert V(\cdot)\rvert$	The number of voxels in a set

Contents

Contents of Figures

Part I

Medical and method background

Chapter 1

Introduction

Contents

1.1 Motivation

In medical examinations and surgeries, minimally invasive technology is widely used. Some specially designed surgical instruments, like biopsy needles, or electrodes are operated by radiologists or robotic systems and inserted in the human's body for extracting cell samples or to perform radiation therapy.

With the advancement of science and technology, several medical imaging modalities are now used routinely in the hospital. To reduce the inside injury and improve the localization accuracy for minimally invasive surgeries, different medical imaging systems, like Computer Tomography (CT), Magnetic Resonance Imaging (MRI) and Ultrasound (US) imaging have been employed for guiding the micro tools inserted in human tissue. Y. Ohno *et al.* use CT to guided percutaneous needles for lung cancer biopsy [Ohno *et al.* (2003)]; X. Chen *et al.* use MRI to guide 14-Gauge (1.6 mm in diameter) needles for breast biopsy [X Chen *et al.* (2004)]. MRI is also used in neurosurgery to ensure that the objects, like biopsy needles or micro-pipettes to deliver drugs, are placed at precise locations in the brain [Hall *et al.* (1999)]. Fig. 1-1 illustrates the demonstrations for guidance of surgical instruments using CT and MRI. The advantages for CT and MRI images are: (i) the resolution of the images are high, so they can provide more detailed information; (ii) they are suitable for every kind of human organs, e.g., from brain to leg. Nevertheless, the disadvantages cannot be ignored. The CT scanner delivers a relatively high dose of radiation to the patient; the MRI scanner produces a loud noise, and lying in the enclosed space of the scanner for a long time makes the patients suffer; the movement affects the MRI image qualities, so the patient should hold still for a long time. What is more, the CT and MRI scanners are extremely expensive, which leads to a high cost for the examinations; both kinds of scanner are huge medical instruments, so that they are neither portable nor flexible.

To avoid some disadvantages, US scanners can also be selected for the miniature biopsy tools guidance. Indeed, there are several advantages for US scanners: (i) the US systems benefit of a short acquisition time, imaging is performed in real-time; (ii) there is no radiation involved during the US scan, it is totally safe; (iii) the quality of the images delivered by modern US scanners have been improved a lot; (iv) the cost of an US scanner is low compared to CT or MRI systems, as well as the examination fee; (v) portable and flexible US scanner are now available on the marked. Due to the reasons above, the US machine is more practical and suitable for the guidance of miniature biopsy and surgery tools inserted in human body compared to CT or MRI.

Usually, in order to observe the tracked tool, like biopsy needle, the radiologists use the one dimensional (1D) US transducers to scan the target region, and get the 2D US image displayed on the monitor. However, this option is difficult because visualization of the needle requires alignment of the US scan plane with the axis of the needle [K Chin *et al.* (2008)]. Fig. 1-2 gives an illustration of 2D US image for guidance of biopsy needle inserted in human's breast tissue.

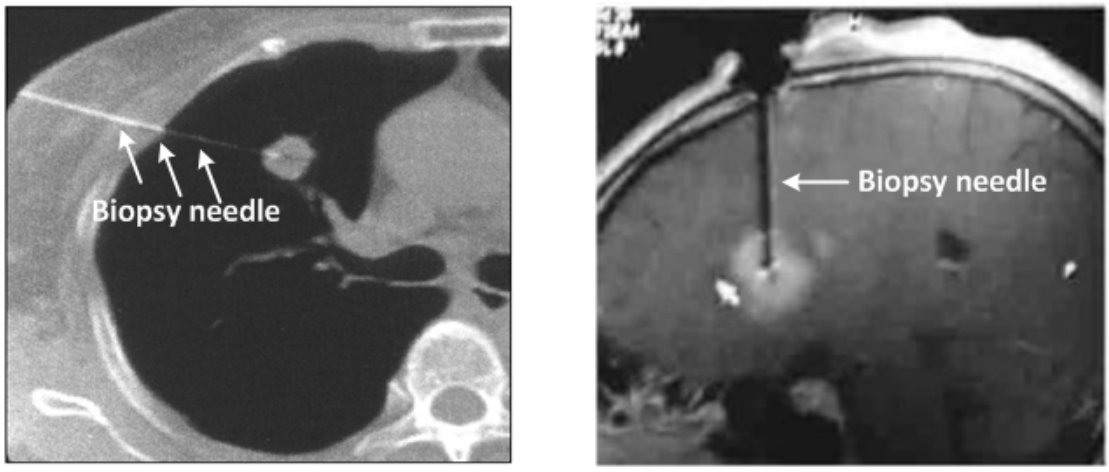

Fig. 1-1 Medical imaging technologies for surgical instruments guidance: (a) CT image for guidance of biopsy needle inserted in human's lung; (b) MRI image for guidance of biopsy needle inserted in human's brain. These two applications are not suitable organs for US imaging.

There are mainly two approaches to 2D US guidance of interventional biopsy needle insertion: guided or freehand [Allen *et al.* (2006)]. In the guided needle approach, a system with a channel attached to the probe is used to guide the needle in the US scan plane of the probe. Fig. 1-3 gives two kinds of US needle guides. By contrast, the freehand approach is technically more challenging and takes longer to learn but it provides greater flexibility. In this approach, one operates the transducer with one hand while the other hand holds the needle unattached to the transducer. To

date, the guided approach has been carried out using mainly 1D array US probes, which can generate 2D images. During the procedure, it is necessary to slide, tilt and rotate the probe so as to align the US beam and the needle axis [KJ Chin (2012)]. Some useful assistant devices have been developed to help in the alignment, for example, the LOGIQ E9 system from GE Healthcare (General Electric Company, USA). It provides a needle assembly that consists of a sheath and stylet, which houses a removable and reusable electromagnetic sensor. There is also a navigation system that can predict the path of the needle tip on the ultrasound scanner, as the iU22 xMATRIX ultrasound system with PercuNav (Philips Healthcare, Koninklijke Philips N.V.), which uses an electromagnetic navigation technology to locate the tip of the needle or other instruments in real time, and also guides the instruments to the target region. However, this type of devices increase the cost of the procedure. Moreover, metal needles and tissues are three-dimensional (3D) structures, and most of the time the needle does not correspond well to the 2D US acquisition plane. Only a part of the needle is visible as shown in Fig. 1-2. Other times, the radiologist can see the tissues and organs clearly, but the needle cannot be found. This increases the risk of injuring normal tissues. As a result, interest in 3D US guidance and computer-aided localization technologies has been increasing.

Our main goal is to use a 3D US system to locate and track the biopsy needle. 3D US volume can be obtained with the classic 1D probe moved mechanically through only one single sweep of a mechanical transducer, by free hand with the help of a calibrator, or with a 2D array. Inside a 3D volume, a better spatial information and relative position between the biopsy needle and the background tissue can be obtained than with conventional 2D US Imaging. What's more, thanks to the 3D acquisition, a plane which contains the needle can always be reconstructed and extracted from the volume. However, it is still difficult for radiologists to locate the needle within a 3D US volume without the assistance of automatic localization tools and the help of computer assisted systems. With the aim of accurate locating and tracking the biopsy needle using 3D US volumes, we propose to develop an algorithm which automatically locates the position of the needle in the 3D US volume, and return the specific frame which contains the tool or the one perpendicular to the tool. Moreover, as the insertion process in the human tissues is a dynamic process, the algorithm must be able to track automatically the needle in dynamic situations, and should always return the tool frame.

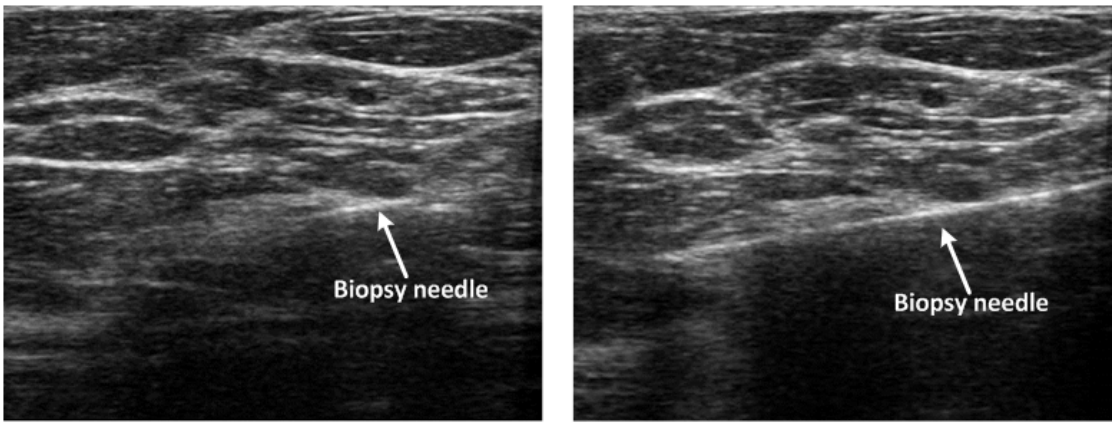

(a) (b)

Fig. 1-2 2D US image for guidance of biopsy needle in the breast tissue: (a) the US acquisition plane is not well aligned with the axis of the biopsy needle, only a part of the needle can be observed; (b) the US acquisition plane is well aligned with the needle axis including its tip, and the image of the needle is relatively clear, (the data sets are kindly provided by D. Buckton and C. Perrey from GE Medical System).

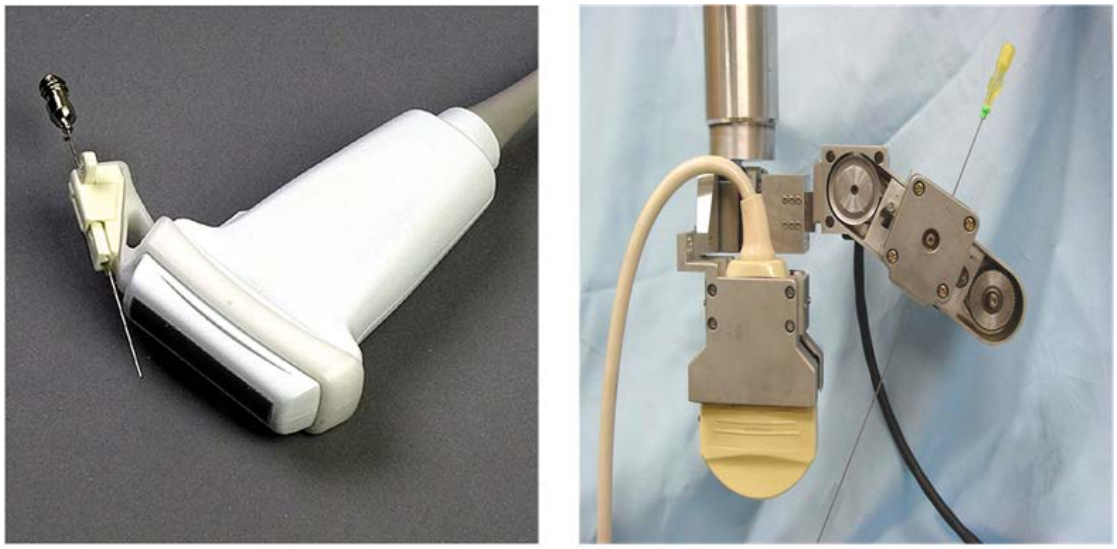

(a) (b)

Fig. 1-3 Two different kinds of needle guides attached to the 2D US probe: (a) the simplest guide attached to a probe; (b) an US-guided motion adaptive needle-insertion instrument [Hong *et al.* (2004)].

1.2 Objectives

Our goal is to develop a robust algorithm which locates and tracks a biopsy needle inserted in human tissue using 3D US in real time. There are several tasks to achieve:

- **Noise reduction.** US image suffers a granular noise pattern called speckle noise. This kind of noise reduces the contrast ratio (CR) of the US image. It can also influence the imaging of the tiny objects, like biopsy needle tip, thus lead to an inaccurate tip localization result. The algorithm involves a strategy for speckle noise reduction.
- **Accuracy.** Precise navigation of surgical tools is crucial. Since the algorithm developed will be further used in clinical applications, the accuracy of the method cannot be neglected. For clinical biopsies, an error of a few millimeters can be acceptable [Mari *et al.* (2011)]. In our work, the desired localization accuracy of the biopsy needle is 2-3 mm with inhomogeneous background.
- **Robustness.** Our algorithm is expected to locate and track the biopsy needle in a dynamic situation. Sometimes, the poor quality of US images lead to the miss-localization of the medical tools. So, a robust position prediction system should be implemented.
- **Real time application.** One of the main interests of US systems is that the images are displayed in real time. The traditional US systems have a frame rate that can easily reach 20-50 2D US frames / second. 3D imaging methods should try to reach the same characteristics. Even if using mechanically sweeping 3D probes, it takes a couple of seconds to acquire one 3D US volume. 2D array probes should be able to attain volume rates higher than 10 volumes / second. Thus to satisfy the real-time constraint, our algorithm should be able to treat one 3D volume within tenth of a second.

The objective of this research is to develop a robust real-time needle localization and tracking method using 3D US. The text of the thesis is organized as follows: Chapter 2 introduces the technical background, including the basic knowledge of ultrasound imaging and the state of the art of the detection and tracking method of micro-tools using ultrasound. Chapter 3 presents the main contribution of the thesis: the ROI based RANSAC and Kalman (ROI-RK) method. In the Chapter 4, the simulation results are given to evaluate the performance of the ROI-RK method under different conditions. Chapter 5 presented a second contribution: the evaluation of the RANSAC with machine learning (ML) algorithm and its performance on biopsy needle localization. At last, the conclusion and perspective of this thesis are given in Chapter 6.

Chapter 2

Technical background

Contents

2.1 Ultrasound imaging

Medical ultrasonography is a diagnostic modality which enables the radiologists to view, in real time, anatomical structures such as muscles, vessels and internal organs. It exploits the backscattering of acoustic energy from biological tissues. A set of pressure pulses are transmitted into the body along pre-determined trajectories, and a narrow ultrasound beam is formed. The ultrasound images are generated from the backscattered signals received from each beam.

Typically, the frequency range of medical ultrasound used in the clinical diagnosis lies between 1 and 20 MHz. The acquisition of ultrasound images is relatively fast and it is considered as a real-time modality with a frame rate from $5-80$ frames per second. Medical ultrasound involves no ionizing radiations, thus there limited side effect. Comparing to other medical imaging modalities like CT and MRI, the device and operation cost of ultrasound are relatively modest, and certain ultrasound scanners are portable and easy to use. However, there are some drawbacks of ultrasound imaging. For example, some organs or anatomical structures, like the bones and lungs,

cannot be properly imaged using medical ultrasound. Moreover, the image quality is affected by a strong speckle noise [Burckhardt (1978)].

The major applications of medical ultrasound include obstetrics (the assessment on the development of the fetus), abdominal ultrasonography (the investigation of liver, kidney, etc …) and cardiology (the diagnosis of the function of heart).

2.1.1 Sound propagation in medium

The propagation of sound is caused by a continuous interchange between the kinetic energy and the potential energy of medium particles, which is related to the density and the elastic properties of the medium [Angelsen (2000)]. In water or biological tissues, in the range of the frequencies involved in medical imaging, the sound propagates as a longitudinal wave (Fig. 2-1).

The sound wave equation which governs the propagation pressure $p(x,t)$ is a function of the position x and time t. Suppose a longitudinal wave with a planar wave front propagates in a homogeneous medium without attenuation, the relation between the pressure $p(x,t)$ and the sound velocity c can be described with the 1D second-order differential equation [Angelsen (2000)]:

$$\frac{\partial^2 p(x,t)}{\partial x^2} - \frac{1}{c^2}\frac{\partial^2 p(x,t)}{\partial t^2} = 0 \tag{2.1}$$

Using the medium compressibility κ [Pa^{-1}], the sound velocity c can be expressed in terms of the density of medium ρ:

$$c = \frac{1}{\sqrt{\kappa\rho}} \tag{2.2}$$

Table 2-1 summarizes the sound velocity for some materials and biological tissues. In case of a harmonic sound wave with frequency f, the sound propagation velocity is given as:

$$c = \lambda \cdot f \tag{2.3}$$

where λ is the sound wavelength in the medium.

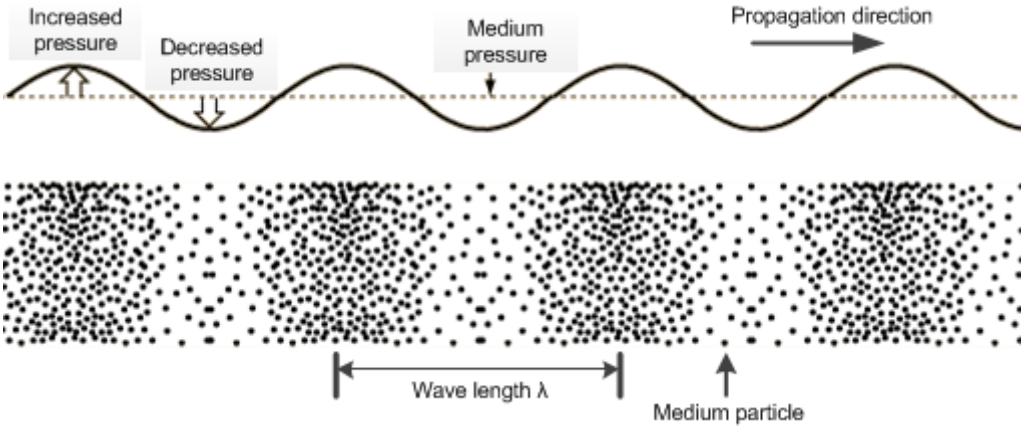

Fig. 2-1 Illustration of the propagation of a 1D longitudinal wave in homogeneous, loss-less medium [1].

Table 2-1 Acoustic parameters for selected materials and biological tissues [Angelsen (2000)].

Medium	Acoustic parameters		
	Density ρ [kg / m^3]	Sound velocity c [m / s]	Impedance × 10^{-6} z [kg /m^{2}s]
Air	1.20	344	0.0004
Water	1000	1484	1.48
Aluminium	2375	6420	17.00
Fat	920	1467	4.33
Lung	400	650	0.26
Liver	1566	1566	1.66
Skull bone	1380 - 1810	2717 - 4077	3.75 – 7.38

One important property of the medium for ultrasound imaging is the acoustic impedance. The specific acoustic impedance z is expressed as the ratio of sound pressure p to particle velocity v at a single frequency:

$$z = \frac{p}{v} = \rho \cdot c \tag{2.4}$$

The unit for z is rayl defined as $1[\text{rayl}] = 1\left[\text{kg} \cdot \text{m}^{-2} \cdot \text{s}^{-1}\right]$. From equation (2.2), equation (2.4) can be written as:

$$z = \sqrt{\frac{\rho}{\kappa}} \tag{2.5}$$

[1] Fig. 2-1 sources from: http://hyperphysics.phy-astr.gsu.edu/hbase/sound/tralon.html

It shows that the specific acoustic impedance z is an inherent property of a medium. Table 2-1 gives the specific acoustic impedance of some selected materials and biological tissues.

When the ultrasound waves encounter the interface between tissues of different acoustic impedances, some parts of them are reflected while others are transmitted. The reflection parts are proportional to the difference in acoustic impedance between the two media. The acoustic impedance explains that a biopsy needle appears brighter than the dark uniform background provided by water or agar phantom [K Chin *et al.* (2008)]. Thus the metal needles which have high impedance are clearly visible against the background from water or agar phantoms which have low impedance (Table 2-1). However, the visibility of biopsy needle inserted in soft tissue is more complex. The soft tissue is a mixture of fluid, muscle, fat, etc… each having a different acoustic impedance. The reflections of the ultrasound waves occur at each of the tissue interface. This makes the background provided by soft tissue inhomogeneous and reduces the visual contrast between the needle and tissue. So it is more difficult to distinguish the biopsy needle inserted in soft tissue than in experiment phantoms.

Scattering

The magnitude of scattered energy depends on several factors like the shape, the size and the acoustic properties of the scatterers. There are three categories of scattering based on length scales: a) specular for reflections from objects whose shapes are much bigger than a wavelength; b) diffractive for objects slightly less than a wavelength to hundreds of wavelength; c) diffusive for scatterers much smaller than a wavelength [Szabo (2004)].

The major part of the scatterers of tissue is in the group of diffusive scatterers. When the incident wave encounters the tissue particles as diffusive scatterers, its energy is reflected into many directions in the form of a spherical wave. During the scanning process, the spherical waves generated by a very large number of diffusive scatterers interact through positive and destructive interferences, which results in a typical “speckle” noise pattern of US images. A biopsy needle has a smooth metallic surface. As a result, the needle acts as specular reflectors [K Chin *et al.* (2008)]. A large part of echoes return to the transducer as the needle-beam angle approaches 90°. If the needle is inserted in a steeper trajectory, the needle-beam angle becomes smaller, less part of echoes can return to the transducer, and this leads to an unclear visibility of the needle (Fig. 2-2).

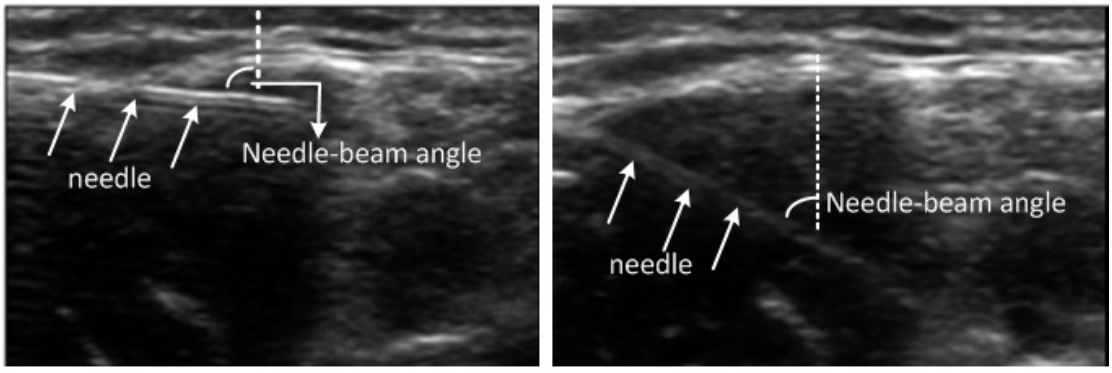

(a) (b)

Fig. 2-2 In-plane view of a 22-gauge (0.711 mm in diameter) biopsy needle with different needle-beam angle: (a) the needle-beam angle is nearly 90°; (b) the same needle inserted in a steeper trajectory [K Chin *et al.* (2008)].

Even though the scattering has a negative effect on the signal-to-ratio (SNR) of the US images, it has the potential to characterize the different tissue and medical instruments like biopsy needles.

2.1.2 US transducer for 3D imaging

The transducer is a key component for the US system. It converts the electrical signal to the mechanical energy and vice versa. The transducer acts in a pulse-echo mode which contains two steps: transmission and reception. In the transmission mode, the transducer is excited by a short electric pulse and generates mechanical vibrations, which transmit into the body as a sound wave. In the reception mode, the transducer receives the sound waves and converts them into electrical signals, which are processed using the US system to finally generate an US image.

The most common US transducers are composed of an array of small piezoelectric crystals. The ultrasound wave is generated thanks to the piezoelectric phenomenon. Through the application of a harmonic voltage, the dimensions of the array of crystals change periodically and a mechanical wave is produced. A new generation technology, the so-called capacitive micro-machined ultrasonic transducers (CMUTs) are known to offer an attractive alternative to the traditional piezoelectric transducers for US imaging [Caliano *et al.* (2005); Novell *et al.* (2009)]. The CMUTs transducers have higher bandwidth and axial resolution than piezoelectric ones, however, their sensitivity is low, which is a limitation particularly for images in the depth of the human body. What's more, the CMUTs transducers are still in development, thus most of the commercial US systems are not compatible with them. Therefore, our introduction still concentrates on the traditional piezoelectric transducers.

Over the past two decades, three different 3D ultrasound imaging approaches have been developed: free-hand techniques with or without position sensors, mechanical scanning, 2D matrix probes [Fenster *et al.* (2001)]. With the existing computer technology, the acquired 3D US volume can either be stored in the original digital format of the US system, for medical utilizations, or exported to an external computer and converted to other digital formats for further medical or scientific analysis. These three 3D US imaging approaches are here discussed.

Free-hand techniques: the free-hand approach is the most wildly used method because of its flexibility. Unlike mechanical probes, which are bulky, heavy and with a limited field of view, the free-hand scanning uses a conventional transducer and can scan large anatomical structures.

Using a conventional probe to scan the interest target to get a series of 2D images and reconstruct the 3D volume, different alignment methods are used: a) an optical or electromagnetic sensor is attached to the transducer to measure its position and orientation (Fig. 2-3). While the transducer is being manipulated, the acquired 2D images are recorded by a computer and a 3D volume is reconstructed using the 2D images and pre-noted information; b) free-hand scan use transducer without sensor. This method needs the operator to move the transducer with a constant linear or angular velocity while acquiring a series of 2D images, then a 3D volume is reconstructed by assuming a predefined geometry. Some computer assisted methods like voxel-based methods, pixel-based methods and function based methods are used to help reconstruct the volume [Lindseth *et al.* (2013)].

Motorized mechanical probes: in the 3D mechanical approach, the target region is scanned by a motorized mechanical probe to translate (Fig. 2-4), tilt (Fig. 2-5, Fig. 2-6) or rotate (Fig. 2-7) a conventional 1D array as it rapidly acquires a series of 2D US images spanning the volume of interest. Because the scanning protocol is predefined and precisely controlled, the relative position and orientation of every 2D image can be obtained accurately [Fenster *et al.* (2001)].

Various kinds of motorized scanning apparatus have been developed to fit the different medical applications. Some probes are with the motor mounted inside the probe housing, which is easy to use but larger and heavier, and also need a specially-designed 3D US machine; other probes can be mounted a motor externally, which is more flexible and can be adapted to hold the transducer of any conventional US machine [Fenster *et al.* (2001); Lindseth *et al.* (2013)].

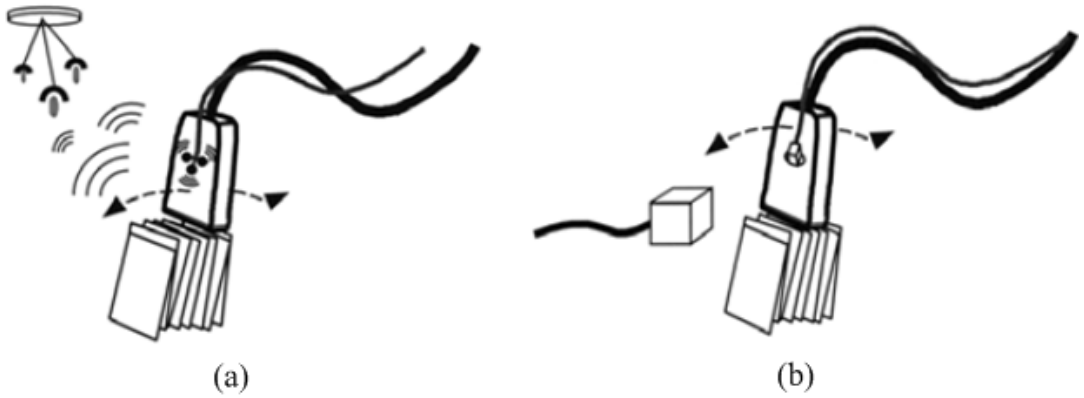

Fig. 2-3 Schematic diagram shows (a) optic or acoustic sensing, and (b) magnetic sensing to record the position and orientation of the transducers [Fenster *et al.* (2001)].

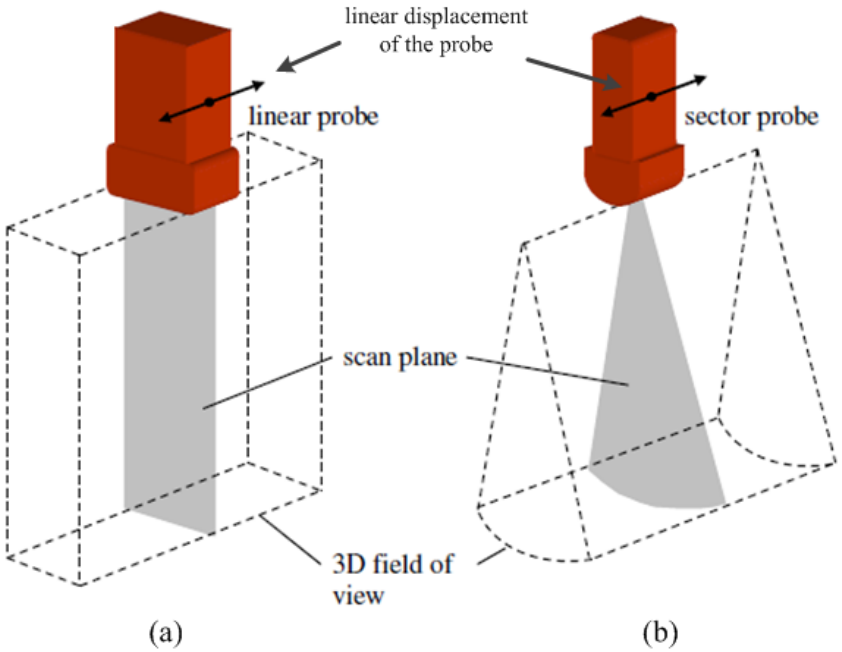

Fig. 2-4 Linear (a) and sector (b) transducer is translated by a motor to acquire a series of parallel 2D images, which are used to reconstruct a 3D volume ([Barva (2007)]).

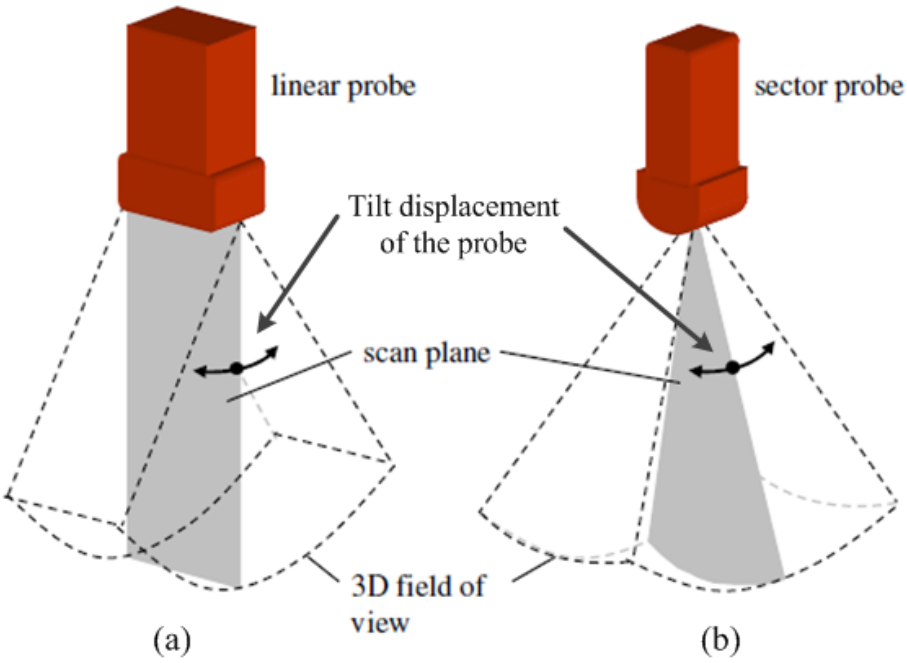

Fig. 2-5 Linear (a) and sector (b) transducer is tilted by a motor to acquire a series of 2D images with a predetermined angular step, which are used to reconstruct a 3D volume ([Barva (2007)]).

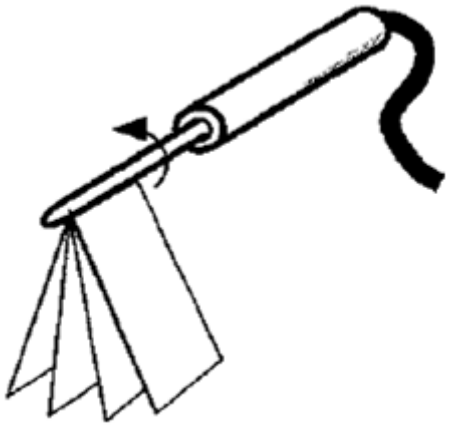

Fig. 2-6 Tilt scanning approach used with a side-firing transrectal (TRUS) transducer to produce 3D images of the prostate ([Fenster *et al.* (2001)]).

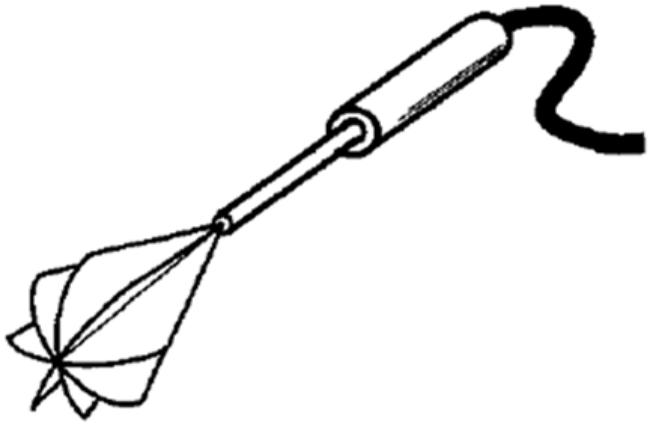

Fig. 2-7 Rotational scanning approach with a end-firing endocavity transducer in gynaecological and urological imaging ([Fenster *et al.* (2001)]).

2D matrix probe: instead of using a conventional 1D array transducer which is mechanically or manually controlled to sweep out the anatomy of interest, transducers with 2D phased arrays (Fig. 2-8) are developed in order to enable the 3D US visualization of dynamic structures in real time, for example, echocardiography images [Smith *et al.* (1991)]. Electronics is used to control the US beam and scan out a volume like a truncated pyramid. With a 2D array of transducer elements, it is challenging to fabricate a cable large enough to connect all the elements in the array. To solve this problem, the sparse array technology is under development and has lead recently to very interesting results [Diarra *et al.* (2013)].

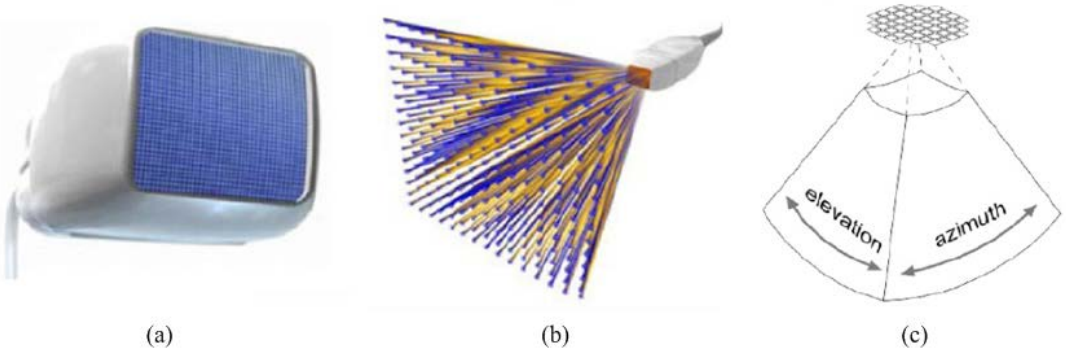

Fig. 2-8 2D matrix probe. (a) 2D array of elements; (b) the beam can be steered in two directions; (c) a truncated pyramid liked data volume can be acquired [Lindseth *et al.* (2013)].

2.1.3 3D US image reconstruction

The acquisition of US data consists of transmission of pulses and reception of echoes from the target region. For each transmission-reception pair, the active elements of the transducer generate a narrow US beam that emits into the tissue, and

then the active elements turn to the receiving mode and record the echoes which contain the tissue information and store them in the memory of the US system for image reconstruction. In case of 3D data acquisition, the beams are organized in an array of $P \times B$, P is the number of planes, and B is the number of beams in each plane. A sampling rate f_s is applied on the radio-frequency (RF) signal of each beam, and the continuous beam is discretized as S samples. Then the RF signal is processed in a sequence of operations to generate a US image (Fig. 2-9).

Band-pass filtering: we denote the sampled RF signal along the *i*-th beam on the *j*-th plane as $\mathrm{r}_{i,j}[\mathrm{n}]$. Received RF signals can have some frequency components outside the frequency band of the transducer. These components correspond to noise. To suppress them, the RF signals $\mathrm{r}_{i,j}[\mathrm{n}]$ are filtered with a band-pass filter which has the same frequency band of the transducer. The filtered RF signals is noted as $\mathrm{f}_{i,j}[\mathrm{n}]$.

Envelope detection: Image intensities shown on the monitor are derived from the amplitude envelope of the filtered RF signals $\mathrm{f}_{i,j}[\mathrm{n}]$. The most common way for computing the envelope of the RF signal is the Hilbert transform:

$$\hat{x}(t) = \mathcal{H}\{x(t)\} = \frac{1}{\pi}\int_{-\infty}^{\infty} \frac{x(\tau)}{t-\tau} d\tau \tag{2.6}$$

where $\mathcal{H}\{\cdot\}$ denotes the Hilbert transform; $x(t)$ denotes the real-valued signal; $\hat{x}(t)$ is the Hilbert transform of $x(t)$.

Introduce an analytic signal $z(t)$:

$$z(t) = x(t) + j \cdot \hat{x}(t) \tag{2.7}$$

The amplitude envelope $e(t)$ is calculated as the complex module of $z(t)$.

$$e(t) = |z(t)| = |x(t) + j \cdot \hat{x}(t)| \tag{2.8}$$

In reality, the Hilbert transform performs on the filtered RF data $\mathrm{f}_{i,j}[\mathrm{n}]$ is a discrete process:

$$\mathrm{e}_{i,j}[\mathrm{n}] = \left|\mathrm{f}_{i,j}[\mathrm{n}] + j \cdot \mathcal{H}\{\mathrm{f}_{i,j}[\mathrm{n}]\}\right| \tag{2.9}$$

where $\mathrm{e}_{i,j}[\mathrm{n}]$ is the discrete envelope signal.

Amplitude compression: the intensity differences of the highly and weakly reflecting tissue structures are very large. This leads to envelope signals $\mathrm{e}_{i,j}[\mathrm{n}]$ with dynamic ranges up to 70 dB [Dutt (1995)]. Such a difference could avoid the clinician to see all the details contained in this huge dynamic range. So an amplitude compression strategy is implemented in the US system. Usually, logarithmic compression is used before displaying the images:

$$c_{i,j}[n] = n_1 \log(e_{i,j}[n] + n_2) \qquad (2.10)$$

where n_1, n_2 are parameters which control the degree of amplitude compression. For the purpose of visualization, $n_1 = n_2 = 1$ is proposed [Jensen (2001)].

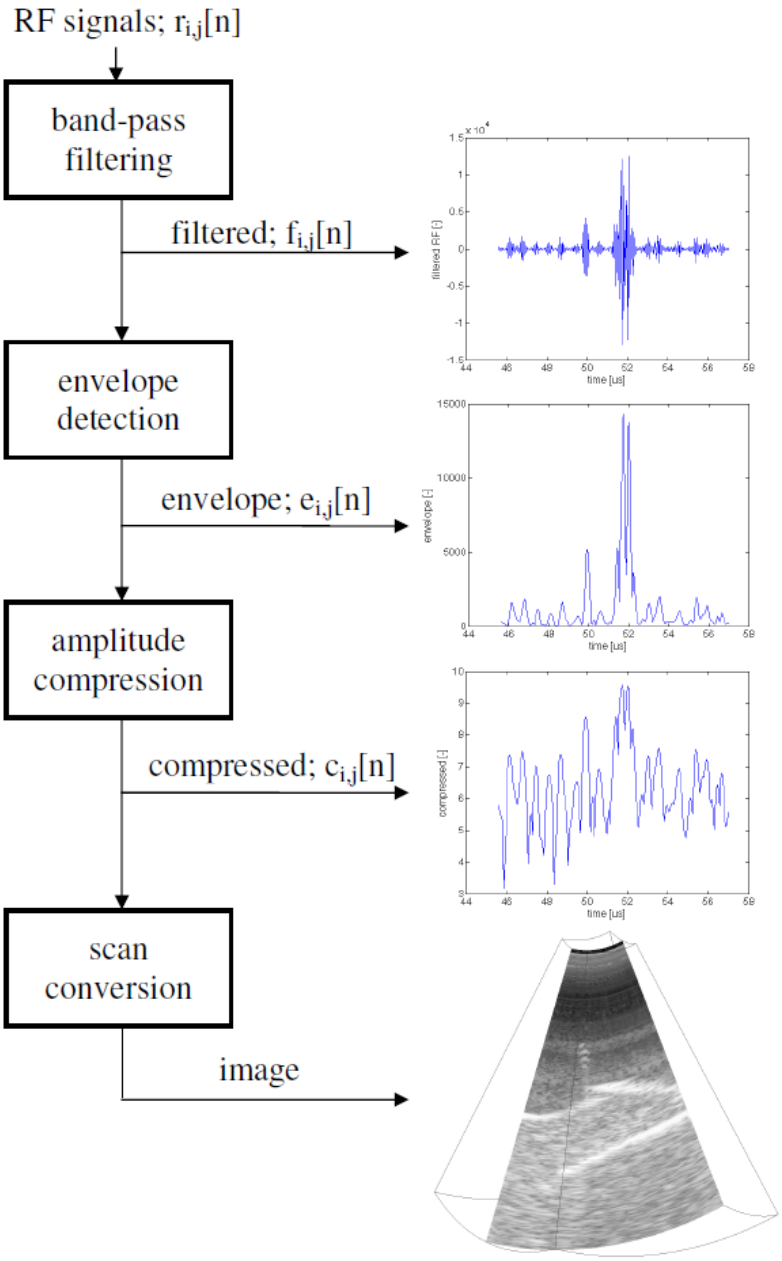

Fig. 2-9 Block scheme illustrating the reconstruction of an US image from the acquired RF signals. The intermediate data are shown on the right side [Barva (2007)].

Scan conversion: the values in $c_{i,j}[n]$ specify the intensities of voxels along the *i*-th beam on the *j*-th plane of the 3D US volume. To correctly display the acquired volume, the position of the voxels corresponding to the intensities $c_{i,j}[n]$ should be determined in a defined Cartesian coordinate system. The convention formula depends on the scan type used for data acquisition. The formulae for a sectorial and a cylindrical geometry are presented in equation (2.11) and (2.12), respectively.

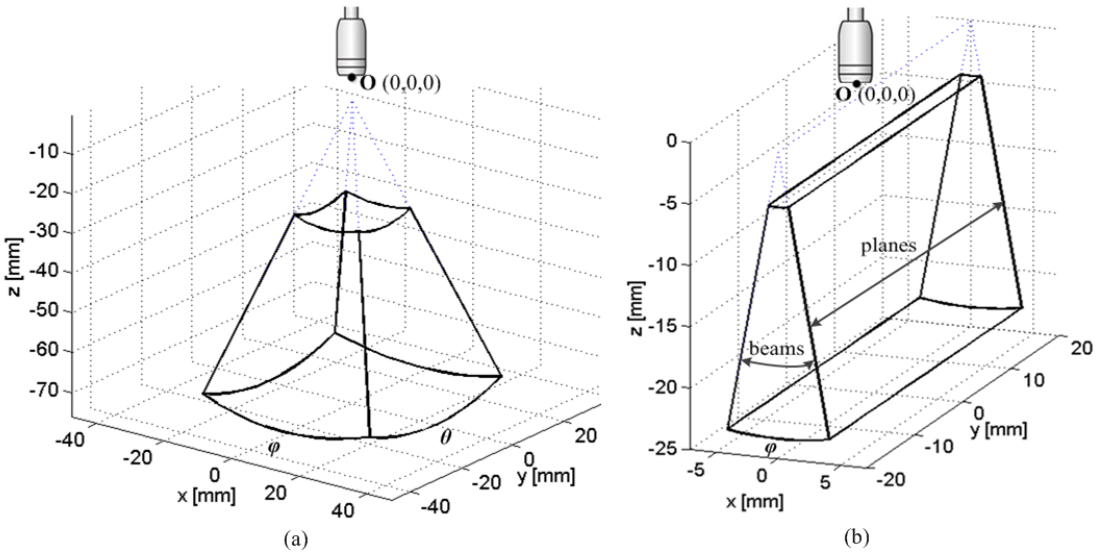

Fig. 2-10 The coordinate system and the geometries of 3D US volume drawn as wireframe model: (a) the sectorial geometry; (b) the cylindrical geometry.

In case of 3D US data with sectorial geometry (Fig. 2-10 (a)), the conversional equation from the indices $[i, j, n]$ to the Cartesian coordinates $[x, y, z]$ is:

$$\begin{bmatrix} x(i,j,n) \\ y(i,j,n) \\ z(i,j,n) \end{bmatrix} = \frac{n \cdot c}{2 f_s} \begin{bmatrix} \sin(\varphi_i) \\ \cos(\varphi_i)\sin(\theta_j) \\ \cos(\varphi_i)\cos(\theta_j) \end{bmatrix} \qquad (2.11)$$

$$\forall i \in \{1,...,B\},\ \forall j \in \{1,...,P\},\ \forall n \in \{1,...,S\}$$

where $\theta_j = \frac{\theta}{P-1}(j-1) - \frac{\theta}{2}$ is the angle of the *j*-th plane, θ is the scan angle of the US plane; $\varphi_i = \frac{\varphi}{B-1}(i-1) - \frac{\varphi}{2}$ is the angle of the *i*-th beam on the *j*-th plane, φ is the scan angle of the US beam; c is the sound wave velocity in the medium as mentioned in Section 2.1.1.

In case of 3D US data with cylindrical geometry (Fig. 2-10 (b)), the conversional equation from the indices $[i, j, n]$ to the Cartesian coordinates $[x, y, z]$ is:

$$\begin{bmatrix} x(i,j,n) \\ y(i,j,n) \\ z(i,j,n) \end{bmatrix} = \begin{bmatrix} \frac{n \cdot c}{2 f_s} \cdot \sin(\varphi_i) \\ s_y \cdot \left(j - \frac{P}{2} \right) \\ \frac{n \cdot c}{2 f_s} \cdot \cos(\varphi_i) \end{bmatrix} \quad (2.12)$$

$$\forall i \in \{1,...,B\}, \forall j \in \{1,...,P\}, \forall n \in \{1,...,S\}$$

where $\varphi_i = \frac{\varphi}{B-1}(i-1) - \frac{\varphi}{2}$ is the tilt angle of the *i*-th beam on each plane, φ is the scan angle of the US beam; s_y is a scale parameter with respect to *y*-axis.

To obtain the final US volume after the scan conversion, an interpolation strategy is performed. The positions of the points in the Cartesian coordinate is calculated using equation (2.11) or (2.12), the corresponding intensities are computed using backward interpolation into the original volume data $c_{i,j}[n]$.

2.2 State of the art of the detection and tracking of biopsy needle using ultrasound

Since needle identification using 2D or 3D US remains one of the hottest research topics in the domain of medical US, several emerging technologies have been recently developed. Most of them use the assumption that the metal biopsy needle appears brighter than the background tissue and the needle axis is always straight. In this section, the principles and the results of the existing needle detection algorithms are summarized.

2.2.1 Principal component analysis (PCA) method

The main idea of PCA is to reduce the dimensionality of a data set consisting of a large number of interrelated variables while retaining as much possible of the variation present in the data set. This is achieved using a mathematical procedure which uses orthogonal transformation to convert a set of observations of possibly correlated variables into a set of values of linearly uncorrelated variables called principal components [Jolliffe (2002)]. In the application of biopsy needle localization, the PCA is used to find the main distribution direction of a cluster of connected pixels, and regards the direction with the largest eigenvalue, or the largest ratio of the first and second eigenvalue as the direction of the needle.

Draper *et al.* developed an automatic needle localization method based on PCA using 2D US image [Draper *et al.* (2000)]. Their method can be developed into 5 steps:

Step 1: The variance of the region surrounding each pixel in the original US image f_o is calculated using the equation:

$$f_v(i,j) = \frac{\sum_{i=1}^{N}\sum_{j=1}^{N}\left[f_o^2(i,j) - \overline{f}_o^2 \right]}{N^2} \tag{2.13}$$

Where, $\overline{f}_o = \frac{\sum_{i=1}^{N}\sum_{j=1}^{N} f_o(i,j)}{N^2}$, the variance kernel is $N \times N$. The aim to calculate the variance image is to enhance the needle pixels and suppress the background noise.

Step 2: a binary image f_b is created by thresholding the variance image f_v. The intensity of all the pixels in f_v can be modeled as a normal distribution with mean μ and standard deviation σ. The threshold T has a linear relation with μ and σ:

$$T = \mu + k\sigma \tag{2.14}$$

Five sample 2D US images are used to estimate the threshold T. The variance kernel size is fixed at 11×11 (by pixel). T is estimated by varying the number of standard deviation above the mean ($k \in [1,5]$ stepped by 0.5), and the optimal value of T is $k = 3.5$.

Step 3: a binary closing operation is implemented to smooth the needle contour. In order to avoid biasing the needle orientation, a symmetrical 3×3 structuring element is chosen.

Step 4: after step 3, the joint bright pixels are identified as potential groups of pixels from the needle. Suppose there are M groups denoted $C_i\,(i = 1,...,M)$ which might stand for the pixels of the needle. To determine whether or not one cluster is a part of the needle, PCA is used to find the principle axis of each cluster by calculating the largest eigenvalue of the covariance matrix $\mathbf{R}_i$:

$$\mathbf{R}_i = \begin{bmatrix} \sigma_{xx}^2 & \sigma_{xy}^2 \\ \sigma_{yx}^2 & \sigma_{yy}^2 \end{bmatrix} \tag{2.15}$$

Where, $\sigma_{xy}^2 = \frac{1}{|C_i|}\sum_{j=1}^{|C_i|}\left(x_j - \overline{x}\right)\left(y_j - \overline{y}\right)$; (x_j, y_j) is the *j*-th Cartesian coordinate of the pixel in the cluster; $\overline{x}$, $\overline{y}$ are the mean x, y coordinate of pixels in C_i; $|\cdot|$ denotes the pixel number in C_i. Suppose $\lambda_{i,1} \geq \lambda_{i,2} \geq 0$ are determined by PCA, then the vector $\mathbf{v}_{i,1}$ corresponding to $\lambda_{i,1}$ is the principle direction of the cluster C_i. Then the

direction of the needle can be identified among the candidates as the cluster with the largest eigenvalue.

Step 5: the needle tip is found by masking the estimated needle direction within the binary image from step 3. Clusters along the line separated by a gap smaller than the diameter of the needle are considered as part of the same cluster. The tip is found as the end of the largest cluster.

The algorithm has been tested on a tissue mimicking phantom with a 14-gauge (2.1 mm in diameter) breast biopsy needle. The phantom was scanned using a 1D US probe at 5.5 MHz. An accuracy of 1 mm for a depth of insertion greater than 15 mm has been reported for the algorithm.

Novotny *et al*. has extended the above algorithm for 3D US imaging [Novotny *et al.* (2003)]. First, the data volume is segmented by a pre-set threshold value. Then with the connection of the neighboring, the binary volume is divided into discrete candidate volumes. PCA is performed on every candidate to find the direction of maximum variance. The candidate with the maximum ratio of the first and second principle components is consider to be the tool volume and the axis direction is determined by the eigenvector corresponding to its maximum eigenvalue. The position of the tool axis is found by projecting the selected candidate's voxel points to a perpendicular plane to its axis. The center is calculated using a linear least square fit. At last the tip of the needle is simply found along the principle axis at the end of the segment cluster.

Their method was tested using a 6.2 mm diameter acetal cylindrical rod which is submerged in water and close to the tissue sample. The method succeeded in locating the position of the rod, and the determination of tip had an small error (mean 0.7 mm, standard deviation 0.6 mm).

The PCA-based needle localization method can perform well only when the needle appears continuous in the image or the distance between clusters remains small enough. Otherwise, error occurs when the wrong cluster has been selected and treated as the tool cluster. As it is known that in real situations, the appearances of biopsy needles are not continuous, which is the challenge for PCA-based algorithms.

2.2.2 Hough transform

The classical Hough transform (HT) tackles the problem with the identification of the lines in the images. It transforms the images to a parameter space of lines, and then uses a voting scheme to find the corresponding parameters for the desired line. However, the computing complexity and large demand of memory are the main drawbacks of these techniques. Based on these features, HT-based algorithms and their modifications have also been implemented in needle localization approaches.

M. Ding *et al.* have proposed a real-time HT (RTHT) for needle segmentation in 2D US image [Ding *et al.* (2003)]. First, the original image is thresholded and transformed to a binary image $f(x,y)$. Second, to reduce the quantity of calculation, a two-step coarse-fine search strategy is carried out in the image space only. At the coarse stage, a lower resolution image $g(x,y)$ is created as:

$$g(x,y) = f(M_x x, M_y y) \tag{2.16}$$

Here, $M_x, M_y \in \aleph$ is the down-sampling factor. The standard HT (SHT) is performed on $g(x,y)$ and the approximate orientation θ^* and position ρ^* of the needle is found. Then, at the fine search stage, the SHT is performed on $f(x,y)$, and in the parameter space, the parameter searching region is set as $\theta \in [\theta^* - \Delta\theta, \theta^* + \Delta\theta]$, $\rho \in [\rho^* - \Delta\rho, \rho^* + \Delta\rho]$, $\Delta\theta$ and $\Delta\rho$ are the expected deviations. At last the accurate orientation θ_n and position ρ_n are determined. The above two stages together are named RTHT. Third, the endpoint of needle is located along the axis direction determined by $[\theta_n, \rho_n]$ using the binary image $f(x,y)$. The running time for RTHT is claimed at an average of 17 ms in 2D US images.

H. Zhou *et al.* have implemented a modification of classical HT -- the 3DHT algorithm for needle segmentation in 3D US volumes [Zhou *et al.* (2007)]. In the first step, a threshold is applied to limit the calculation time and generate a binary volume. The second step is to find the most appropriate parametric equation for the 3D line that crosses the maximum number of voxels. The basic idea for HT is to specify the parameters of a line in the parameter space. As a 3D line can be represented using minimum four parameters [Roberts (1988)], the goal is to determine them using the thresholded data set.

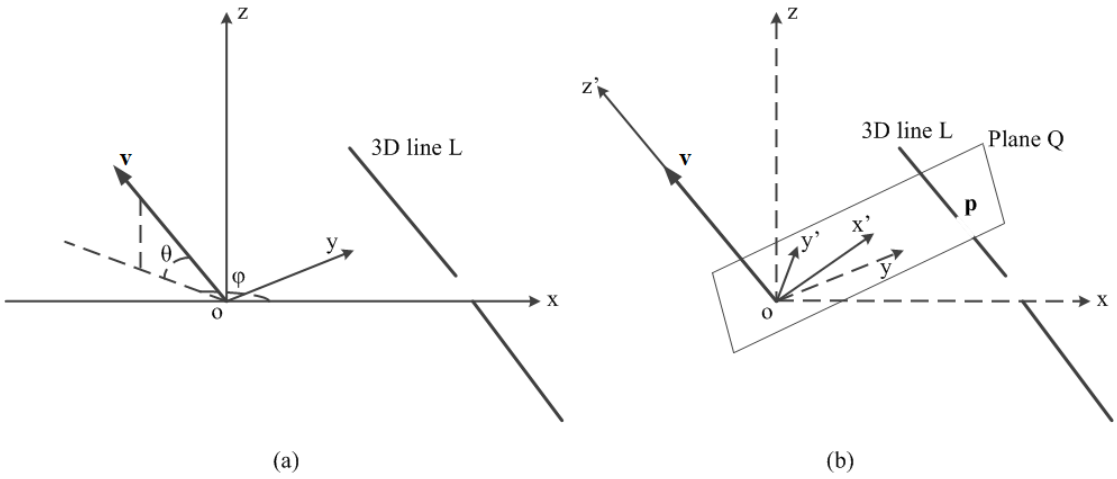

Fig. 2-11 Illustrations for a 3D straight line in the Cartesian coordinate: (a) the direction vector of the line **v** is determined by the two directional angles θ and φ; (b) a plane Q with the normal vector **v** is selected. The Cartesian coordinate (x', y', z') is a rotation of the original coordinate (x, y, z). The direction of z' axis is the same as vector **v**. The point p is determined using the (x', y').

Fig. 2-11 gives an illustration of the parameters used for representing the 3D lines. The directional vector **v** can be determined using the azimuth angle φ and the elevation angle θ. A point **p** on the line L can be determined using two parameters ρ and α in the rotated Cartesian coordinate (x', y'), where ρ is the distance from **p** to the origin o, α is the angle between the line $o\mathbf{p}$ and the x' axis. Thus the 3D line L can be represented using the four parameters $(\theta, \varphi, \rho, \alpha)$. For each point in the 3D image, the (ρ, α) of the needle can be solved with a specified (θ, φ). A Hough parameter accumulator $H(\theta, \varphi, \rho, \alpha)$ is defined and initialized to zero. For each point with the value "1" in the binary image, all possible parameters $(\theta, \varphi, \rho, \alpha)$ are calculated and $H(\theta, \varphi, \rho, \alpha)$ is accumulated. The best fitted parameters are found as:

$$(\theta_{\max}, \varphi_{\max}, \rho_{\max}, \alpha_{\max}) = \arg\max H(\theta, \varphi, \rho, \alpha) \qquad (2.17)$$

A water phantom with a nylon line to simulate a needle was used to test the algorithm. The 3D HT was implemented using Visual C++ 6.0. The orientation deviation was reported at 1.5° and the position deviation about 1.8 mm. The running time was 3-4 seconds on segmentation of a chosen region of the original 3D US volume.

P. Hartmann *et al.* also used the 3DHT method to segment the needle on prostate biopsy images [Hartmann *et al.* (2009)]. The method is implemented using C++ and a variation of computation time from 45-200 seconds has been reported.

To reduce the running time, H. Zhou *et al.* proposed an improved 3DHT (3DIHT) by adding a coarse-fine search strategy to automatically segment the needle in 3D US volumes [Zhou *et al.* (2008)]. First a volume cropping is done on the original volume to limit the size, and the threshold strategy is used to create the binary volume. Then a down-sampled volume is created for coarse search using 3D HT and fixed the parameters $\left(\theta^*, \varphi^*, \rho^*, \alpha^*\right)$ for an approximate position of the needle. To obtain a more accurate segmentation, the original 3D binary volume is used in the fine search step. However, the searching range for 3D HT is set as $\left(\theta^* - \Delta\theta, \varphi^* - \Delta\varphi, \rho^* - \Delta\rho, \alpha^* - \Delta\alpha\right)$ to $\left(\theta^* + \Delta\theta, \varphi^* + \Delta\varphi, \rho^* + \Delta\rho, \alpha^* + \Delta\alpha\right)$. The step $\Delta\cdot$ has the relation with the down-sampling factor. The 3D HT together with the coarse-fine search strategy is named as 3DIHT in [Zhou *et al.* (2008)]. The localization accuracy is a little decreased using 3DIHT, but the running time is less than 2 seconds under C++ environment.

To further reduce the computational complexity and the large storage requirements, W. Qiu *et al.* use 3D quick randomized HT (3DQRHT) to segment the needle in a water phantom [Qiu *et al.* (2008)]. Their method is based on the idea of randomized HT (RHT) [Kultanen *et al.* (1990)]. In 3D RHT, a pair of 3D points $\left(\mathbf{p}_{i,1}, \mathbf{p}_{i,2}\right)$ is randomly chosen using a probability distribution, and a 3D line can be defined using this pair and the parameter $\left(\theta_i, \varphi_i, \rho_i, \alpha_i\right)$ of the line can be calculated. The Hough accumulator $H\left(\theta, \varphi, \rho, \alpha\right)$ is used to count the different parameter pairs, the value of $H\left(\cdot\right)$ is the times when the different pairs of points are found on the same line. The solution of the target line is found at the maximum value of $H\left(\theta, \varphi, \rho, \alpha\right)$.The main improvement of 3DQRHT is the implementation of the coarse-fine search in the 3D RHT. Using 3DQRHT, the localization time for the needle using 3D US is around 1 s under C++ environment.

To summarize, HT-based linear tool localization methods needs much calculation time and big computer memories. Because HT is used as a line detector, if there are other line-like structures in the 3D data volume, the HT-based algorithms fail to locate the correct position of the needles.

2.2.3 Parallel integral projection (PIP) transform

The PIP transform is a special form of the Radon transform. The traditional Radon transform is reduced to a plane detector and cannot detect line structures in 3D

situation. Novotny *et al.* have first proposed a modified Radon transform to detect the lines in 3D US volumes [Novotny *et al.* (2007)], which is the same transform as PIP. The PIP transform is defined as a mapping which transforms a 3D volume $f(x, y, z)$ to a function P_V. Usually, P_V is defined as an integral along a line passing a point $Q(u,v)$ on a plane with the normal direction determined by two angles α, β:

$$P_V(u,v,\alpha,\beta) = \int_{-\infty}^{\infty} f\left(\mathbf{R}(\alpha,\beta)\cdot(u,v,\tau)^T\, d\tau\right) \tag{2.18}$$

$$\mathbf{R}(\alpha,\beta) = \begin{pmatrix} \cos\beta & \sin\alpha & \cos\alpha\sin\beta \\ 0 & \cos\alpha & \sin\alpha \\ \sin\beta & -\sin\alpha\cos\beta & \cos\alpha\cos\beta \end{pmatrix} \tag{2.19}$$

here, α and β are anticlockwise rotation angles around x-axis and y-axis respectively, thus $\mathbf{R}(\alpha,\beta)$ is the rotation matrix.

Barva *et al.* have implemented the PIP transform into a straight electrode localization algorithm in 3D US [Barva *et al.* (2008)]. Assuming the appearance of the electrode is straight and the intensity of the electrode voxels are much higher than the background voxels, as the electrode's diameter is close to zero, the axis of the electrode can be found by maximizing P_V of the original US volume:

$$(u_{\max}, v_{\max}, \alpha_{\max}, \beta_{\max}) = \arg\max P_V(u,v,\alpha,\beta) \tag{2.20}$$

Then the parametric equation for the electrode's axis is:

$$a(t) = \mathbf{R}(\alpha_{\max}, \beta_{\max})\cdot(u_{\max}, v_{\max}, t)^T \tag{2.21}$$

Here, $t \in \Re$ is the parameter.

To search the maximum PIP transformation, a discrete operation is implemented. In order not to miss the electrode, the discretization steps are set as:

$$\Delta\alpha, \Delta\beta \le 2\arctan\frac{d}{2\|\mathbf{x}_{\max}\|} \tag{2.22}$$

$$\Delta u, \Delta v \le d \tag{2.23}$$

Here, d is the diameter of electrode; $\mathbf{x}_{\max}$ is the most distant voxel's position in Cartesian coordinate.

The $u_{\max}$, $v_{\max}$, $\alpha_{\max}$ $\beta_{\max}$ cannot be determined in one step. So the pair $(u_i^{\max}, v_i^{\max})$ are first found given a fixed angular pair (α_i, β_i). The corresponding PIP projection value is noted as $P_i^V(u_i^{\max}, v_i^{\max}, \alpha_i, \beta_i)$. Then the $(\alpha_{\max}, \beta_{\max})$ can be determined using:

$$(\alpha_{\max}, \beta_{\max}) = \arg\max P_i^V(u_i^{\max}, v_i^{\max}, \alpha_i, \beta_i) \tag{2.24}$$

$i \in \aleph$ is the index.

Two searching approaches have been tested for the maximization: i) exhaustive search and ii) hierarchical mesh-grid search [Stoer *et al.* (1993)]. In the exhaustive search, the angles α and β are arranged in the uniform square grid of $[0,180]\times[0,180]$, with the fixed steps $\Delta\alpha$, $\Delta\beta$ calculated in equation (2.25). The computational complexity is unbearable. The hierarchical mesh-grid search is a coarse-to-fine procedure. In the first level, a relatively large step of $\Delta\alpha_1$ and $\Delta\beta_1$ is chosen to determine the region of possible maximum value of P_V. In the second level, within this region, the same operation is done with the steps calculated as:

$$\Delta\alpha_2 = \frac{\Delta\alpha_1}{2}, \Delta\beta_2 = \frac{\Delta\beta_1}{2} \tag{2.25}$$

The searching algorithm continues until the steps $\Delta\alpha_i$, $\Delta\beta_i$ are equal or inferior to the pre-set threshold values $\Delta\alpha_t$, $\Delta\beta_t$ which control the accuracy of the axis localization. The hierarchical mesh-grid search allows accelerating the calculation time of PIP-based axis localization method.

The PIP-based electrode localization algorithm has been tested on both simulated data using Field II [Jensen *et al.* (1992); Jensen (1996)] and real data. The accuracy for electrode's axis localization is reported between 0.2 and 0.3 mm. however, even though the hierarchical mesh-grid search is implemented to accelerate the computing time, the average time used to locate the axis is 18 minutes, which is not bearable for real-time applications.

A fast multi-resolution-PIP (MR-PIP) algorithm for localizing straight electrodes in 3D US volumes has been proposed to limit the calculation time [Uherčík *et al.* (2008)]. Instead of using the whole volume for the calculation of PIP projection function P_V, a series of down sampled volumes are created using a special decimation filter: (a) $f_{\max}$ -- the maximum intensity of the neighboring voxels ; (b) f_{avg} -- the standard average of the neighboring voxels. The $f_{\max}$ is suggested in [Uherčík *et al.* (2008)] because it preserves relatively well the contrast between the electrode and background.

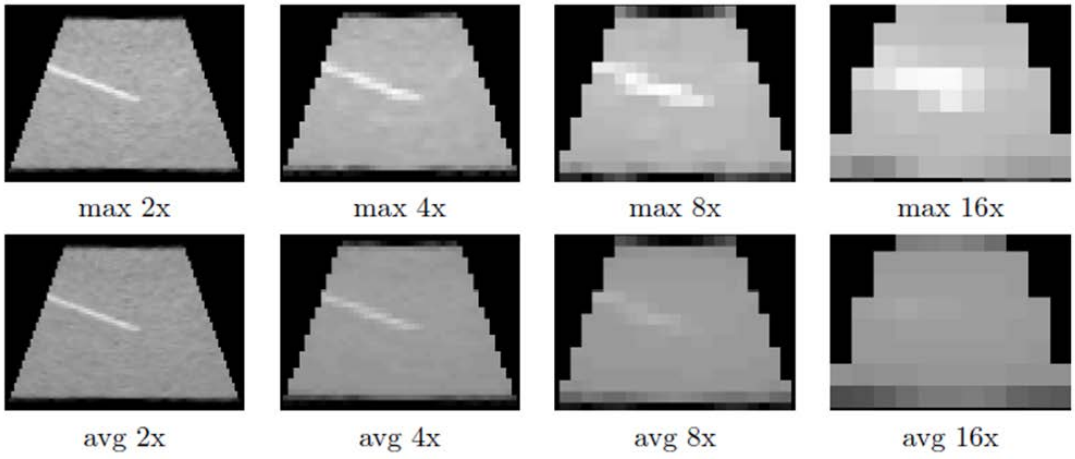

Fig. 2-12 The multiple down-sampled images of a 2D frame with needle selected from a simulated 3D US volume using the $f_{\max}$ (denoted max) and f_{avg} (demoted avg) [Uherčík *et al.* (2008)].

To reduce the iterations of PIP based localization algorithm, the discretization steps for u, v, α, β decrease as the resolution of the series of down sampling volumes is refined. Moreover, the iteration steps at a coarser resolution than the original volume, this also helps decrease the iteration time.

The fast MR-PIP algorithm has been tested on simulated and real US volumes. The average calculation time reduced to 10 seconds, however, the axis accuracy is reported at 2-3 mm. This shows that the decrement of running time is always at the expense of growth of localization error. What's more, 10 s for localizing the electrode in one 3D volume cannot satisfy the demand of real-time application.

2.2.4 RANSAC

The Random Sample Consensus (RANSAC) algorithm was introduced by M. Fischler and R. Bolles in [Fischler *et al.* (1981)]. It is an iterative method used to estimate the parameters of a pre-set mathematical model from a dataset that contains inlier points, which can be approximately fitted to a model, and outlier points, which cannot be fitted to this model. In image processing, it is used to detect line-like or circle-like features. Unlike conventional sampling techniques that use as much of the data as possible to obtain an initial solution, RANSAC uses the smallest set possible to form the model and then proceeds to enlarge this set with consistent data. For a line structure, the RANSAC procedure chooses only two points from the whole dataset to form one linear model in one iteration, and then calculates the model cost involving all the points. After all the iterations, the cost of different models is compared, and the minimum cost model is considered as the best-fitting model for the dataset. M.

Uherčík *et al.* have proposed an efficient model-fitting RANSAC (MF-RANSAC) algorithm for straight needle localization in 3D US volume [Uherčík *et al.* (2010)]. Since the contributions of this thesis are partly based on RANSAC, the details about this algorithm and our implementation are presented in Chapter 3.

2.2.5 Instrument based straight tool localization methods

The above sections present the computer assisted tool localization methods without other instruments. It exists also localization methods using the assistance of robot or some US technologies. Z. Wei *et al.* proposed a threshold based method for oblique needle segmentation and tracking with a 3D Trans Rectal Ultrasound (TRUS) guided and robot assistant prostate brachytherapy system [Wei *et al.* (2004)] [Wei *et al.* (2005)]. The differences between voxels are obtained by subtracting a live-scan 3D US volume and a pre-scan US volume performed before insertion of the needle. Then, by thresholding, the background noise is removed and the voxels of the needle are detected. Finally, the 3D US volume is reconstructed. With robotic assistance, their method can achieve high accuracy, but the registration of the pre-scan and post-scan volume remains a problem if the free-hand scan is used. What's more, the use of a robot strongly limits the field of application and increases the system's cost dramatically. K. Nichols *et al.* tested the visibility of needles with different echo enhancement modifications in the change in angles of insonification [Nichols *et al.* (2003)]. From their conclusion, the prototype dimpled and echotip needles best maintains their visibility at the clinical important angles, which can be a reference in 2D or 3D US guided minimally invasive surgeries. M. Fronheisr *et al.* used a US system with 3D color Doppler combined with the ColorMark technology to track a vibrating needle at kilohertz frequencies for cardiac applications [Fronheiser *et al.* (2008)]. Thanks to the analytical model for the vibrating device and the improvement of the Doppler setting, which helps to detect vibrating devices, their method is able to distinguish the needle tip from the vessel or heart wall. V. Rotemberg *et al.* developed a three-step segmentation algorithm which can identify a needle in an acoustic radiation force impulse (ARFI) image and overlay the needle prediction on a 2D co-registered B-mode image [Rotemberg *et al.* (2011)]. The contrast of ARFI image is derived from the differences in mechanical properties rather than acoustic properties of tissues, so the needle appears in ARFI images as some part of the medium with lower displacement than the surrounding tissues. Due to this property, using contrast enhancement, noise suppression and smoothing methods, accurate position of the needle can be obtained on the ARFI images. Thanks to a registration between the B-mode and the ARFI image, the needle's position can be determined accurately. A robotic vision system that can automatically retrieve and position surgical instruments in the robotized laparoscopic surgical environment has been proposed in [Krupa *et al.*

(2002)]. Their system includes a special designed device to hold the surgical instrument with tiny laser pointers. It can be used to automatically guide the instrument in the field of view. What's more, images of optical markers mounted on the tip of the instrument and images of the laser spots projected by the same instrument are used to estimate the distance between the instrument and organ in real time. Their system has been successfully validated by performing a experiment on living pigs.

To summarize, the instruments based needle navigation systems are accurate, however, these methods depend on specially designed systems, which will increase the cost. As a result, because of these specific and limiting conditions, (for example, the robotic arm for robotic navigated system), these methods are not extensively applied in clinical utilizations.

2.3 Conclusion

This chapter can be divided into two parts. In the first part, we first introduced the properties of sound wave. Then the different types of US transducers are introduced to give concrete concept of a 3D US volume generation. At last, the 3D US volume reconstruction steps are presented.

In the second part, we introduced the state of the art of micro tool localization methods. To limit the calculation time, a threshold step is performance in all the algorithms. The PCA-based methods aim at locating the most important eigenvector of the point clusters which stands for the needle. The HT-based algorithms search for the most appropriate parameters which define the straight line in the parametric space. The PIP transform locates the line position by searching the maximum value of the integral projections along all the possible directions. Finally a brief summary of the instrument based micro-tools localization methods is also presented in this part.

PART II

Contributions

Chapter 3

Contribution: ROI-RK method

Contents

In this chapter, the ROI-RK method is presented. This method can be divided into two parts: the initialization and the tracking procedures. Section 3.1 introduces a global view of the ROI-RK method. Section 3.2 presents the initialization step: first the principle theory used for noise reduction is presented in sub-section 3.2.1, and then follows the method of ROI initialization. Section 3.3 mainly presents the tracking procedure of the ROI-RK method. In sub-section 3.3.1, the basic theories of the used methodology, such as Kalman filter and speckle tracking method are introduced. Then follows our applications stated in sub-section 3.3.2. At last, a conclusion is given in section 3.4.

3.1 Global view of ROI-RK method

It is very difficult for radiologists to manually detect the correct US plane that contains the needle in the 3D US volume. Therefore, automatic needle detection methods for 3D US volumes have become very important. There are several

challenges for the existing needle localization algorithms. First, the 3D US volume has speckle noise, and certain parts of tissue may have the same level of intensity as the needle; in this situation the localization algorithms fail to detect the correct position of the needles. Second, there are tens of thousands of voxels in a series of 3D US volumes, which leads to a large quantity of calculations. Third, most of the localization methods can detect the needle in only one single 3D US volume. No method is tested in a dynamic situation. For a tracking task, the localization method should be robust enough to follow the position of the needle in a series of acquisitions of 3D US volumes. What's more, the running time should be short enough to satisfy the demand of real-time application, i.e. the processing time should be faster than the acquisition time. With the aim of responding to the three constraints mentioned above, we propose to improve the model of RANSAC algorithm using a region of interest (ROI) based RANSAC and Kalman (RK) method for localizing and tracking the needle in a series of 3D US volumes in real time.

The ROI-RK algorithm is mainly based on three assumptions:

(a) The intensity of the needle voxels is higher than the background voxels.

(b) The needle is a thin, long and straight cylinder.

The needle might be deformed during the insertion because of the lateral forces [Dimaio *et al.* (2003)]. Typically, the bending situations mostly happen within the thin electrodes (diameter around 0.3 mm). The main application background for this thesis is the liver biopsy, and the needle size varies from 15 to 20 Gauges [Plecha *et al.* (1997)] (diameter around $0.8 - 1.5$ mm), so the needle remains straight during insertion.

(c) The trajectory of insertion stays always the same direction. Even though a slightly relative motion could happen, it does not influence the main direction of insertion.

The details of ROI-RK method is introduced in the following sub-sections of this chapter. In a global view, it consists of two main steps (Fig. 3-1):

Step 1: Initializing step – To enhance the contrast between the needle and background, a 3D line filter [Frangi *et al.* (1998)] is used in the complete 3D US volume to obtain a tubularness volume. The RANSAC algorithm runs in this volume to get an initial position of the needle. Using this position, the ROI is initialized automatically.

Step 2: Tracking step – The following operations are only run inside the ROI. The biopsy needle is detected and tracked in three steps: (a) the RANSAC algorithm is used to detect the position of the needle in the ROI; (b) speckle tracking is used to estimate the velocity of the needle tip; (c) the Kalman filter is used to update the ROI and refine the position of the needle.

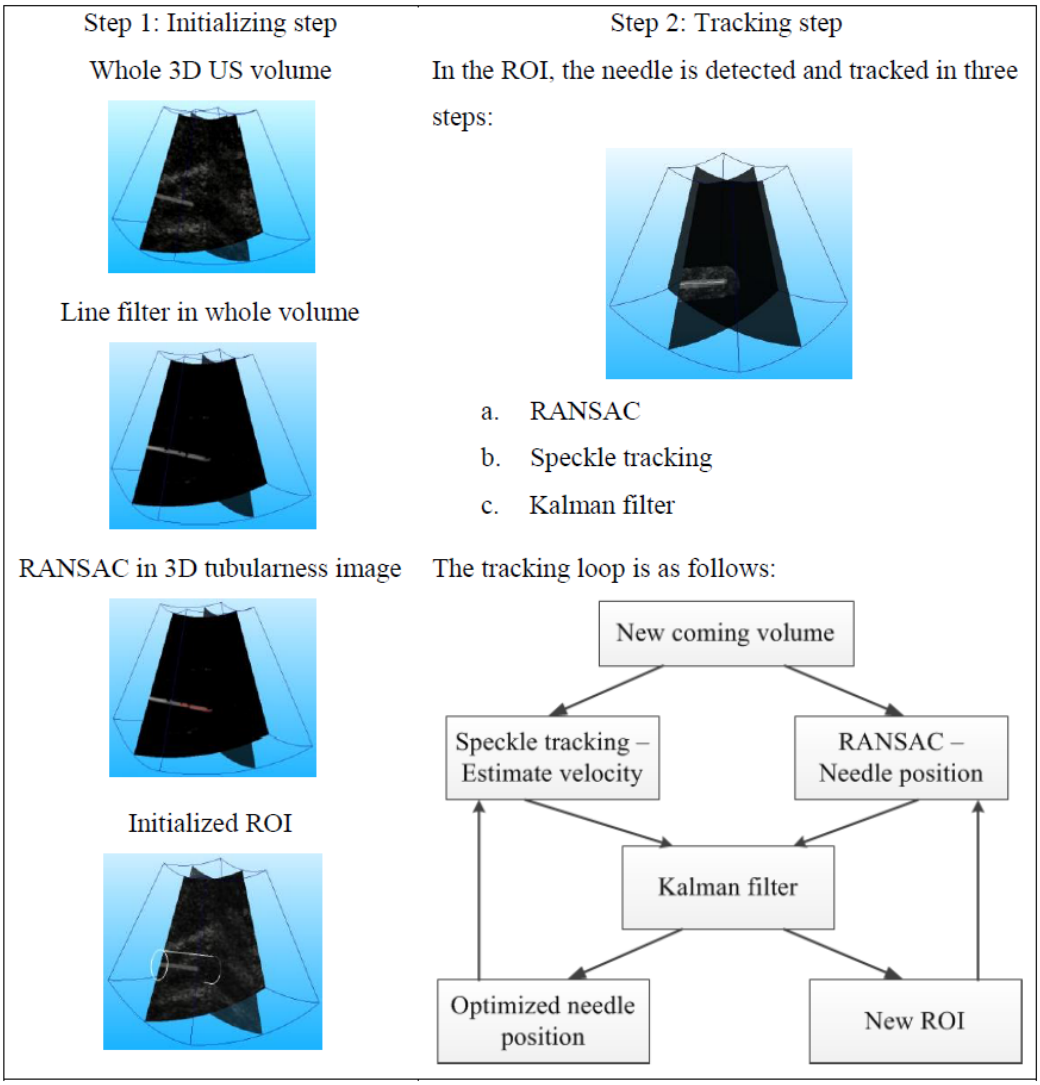

Fig. 3-1 A global view of the ROI-RK method

3.2 Step 1: Initialization

The original 3D US volume includes needle voxels and inhomogeneous background voxels. The high-intensity voxels from the inhomogeneous background are outliers and influence the result of localization algorithms. Without restricting the processed data to a limited ROI that contains the needle, the localization algorithms running in the whole US volume could confuse the high-intensity line-like tissue structures and needle, and thus yield a false needle position. Unfortunately, for the initial volume even a rough position of the needle is not known. As a result, the complete volume must be processed so as to initialize the ROI used in the remaining part of the algorithm. To reduce the risk of false detection, a 3D line filter initially proposed by

Frangi *et al.* [Frangi *et al.* (1998)] and previously used by our group [Uherčík *et al.* (2009)] is applied to enhance the contrast between the needle and the background. Section 3.2.1 briefly introduces the principle theory of line filter enhancement and compares the performance of three different line filter enhancement methods.

3.2.1 Introduction of line filter

The original application of line filter is the enhancement of vessel structures, so that it is easier to segment the structures from background tissue [Frangi *et al.* (1998)]. The line enhancement measurement for the tubular structure is a Hessian matrix based method.

Let $V(M(x,y,z),I(M))$ be a set of voxels of a 3D US volume having two characteristics for each voxel: $M(x,y,z)$ and $I(M)$ represent the position in the image and intensity of the voxels, respectively. Note that when the term "voxel" is used, the indices coordinates are used; when the term "point" is mentioned, the Cartesian coordinate is used. The intensity variation of an image function is evaluated using the second-order derivatives. The Taylor expansion of the image function $f_V(V)$ at the voxel M_0 is:

$$f_V(M_0+\Delta M_0) = f_V(M_0) + \Delta M_0^T \nabla f_V(M_0) + \frac{1}{2}\Delta M_0^T \mathbf{H}(M_0)\Delta M_0 \qquad (3.1)$$

where $\mathbf{H}(M_0)$ is the Hessian matrix:

$$\mathbf{H}(M_0) = \begin{bmatrix} f_{Vxx}(M_0) & f_{Vxy}(M_0) & f_{Vxz}(M_0) \\ f_{Vyx}(M_0) & f_{Vyy}(M_0) & f_{Vyz}(M_0) \\ f_{Vzx}(M_0) & f_{Vzy}(M_0) & f_{Vzz}(M_0) \end{bmatrix} \qquad (3.2)$$

According to the concepts of the linear scale space theory, the derivatives of the image $f_V(M)$ are defined as a convolution with the derivatives of a Gaussian function [Florack *et al.* (1992)]:

$$f_{Vx}(M) = f_V(M) * \frac{\partial}{\partial x} G(M,s) \qquad (3.3)$$

$$f_{Vxy}(M) = f_V(M) * \frac{\partial}{\partial x \partial y} G(M,s) \qquad (3.4)$$

$G(M,s)$ is the three-dimensional Gaussian kernel defined as

$$G(M,s) = \frac{1}{\sqrt{2\pi s^2}^3} \exp\left(-\frac{\|M\|^2}{2s^2}\right) \qquad (3.5)$$

Here, s is the scale. In our case, it is set as the expected radius of the needle.

The Hessian matrix contains the second-order information of the local structure. Suppose that λ_1, λ_2 and λ_3 are the eigenvalues of the Hessian matrix, and

$|\lambda_1| \le |\lambda_2| \le |\lambda_3|$. For an ideal bright tubular structure with a dark background, the three eigenvalues satisfy:

$$|\lambda_1| << |\lambda_2| \approx |\lambda_3| \text{ and } \lambda_1 \approx 0 \text{ and } \lambda_2 < 0, \lambda_3 < 0 \tag{3.6}$$

A simple line filter enhancement is proposed by Q. Li *et al* [Li *et al.* (2003)]:

$$J_L = \frac{|\lambda_2|}{|\lambda_3|}\left(|\lambda_2| - |\lambda_1|\right) \tag{3.7}$$

J_L is maximized when $|\lambda_2| \approx |\lambda_3|$ and the difference between $|\lambda_2|$ and $|\lambda_1|$ is large.

Y. Sato *et al.* have proposed a multi-scale line filter enhancement using the eigenvalues of the Hessian matrix [Sato *et al.* (1998)] summarized as:

$$J_S = \begin{cases} |\lambda_3|\left(\frac{\lambda_2}{\lambda_3}\right)^{\gamma_{23}}\left(1+\frac{\lambda_1}{|\lambda_2|}\right)^{\gamma_{12}}, & \lambda_3 < \lambda_2 < \lambda_1 \le 0 \\ |\lambda_3|\left(\frac{\lambda_2}{\lambda_3}\right)^{\gamma_{23}}\left(1-a_S\frac{\lambda_1}{|\lambda_2|}\right)^{\gamma_{12}}, & \lambda_3 < \lambda_2 < 0 < \lambda_1 < \frac{|\lambda_2|}{a_S} \\ 0, & \textit{otherwise} \end{cases} \tag{3.8}$$

Here, $\gamma_{23} \ge 0$ controls the sharpness of the selectivity for the cross-section isotropy. $\gamma_{12} \ge 0$ and $0 < a_S \le 1.0$. α is introduced to give an asymmetrical characteristic in the negative and positive regions of λ_1. The $\gamma_{12} = \gamma_{23} = 1.0$, $a_S = 0.25$ are proposed by Sato *et al* [Sato *et al.* (1998)].

Frangi *et al*. have proposed an advanced tubularness measurement by introducing three natural quantities: R_B distinguishes the structure from a blob-like pattern:

$$R_B = \frac{|\lambda_1|}{\sqrt{|\lambda_2\lambda_3|}} \tag{3.9}$$

R_A distinguishes between plate-like and line-like structures:

$$R_A = \frac{|\lambda_2|}{|\lambda_3|} \tag{3.10}$$

and S quantifies the needle voxels and background voxels:

$$S = \|H\|_F = \sqrt{\sum_{i=1}^{3}\lambda_i^2} \tag{3.11}$$

the tubularness measurement function is defined as:

$$J_F = (1-\exp(-\frac{R_A^2}{2a_F^2}))\exp(-\frac{R_B^2}{2b^2})(1-\exp(-\frac{S^2}{2c^2})) \tag{3.12}$$

here, a_F, b and c are parameters that control the sensitivity of $T(M)$ to measure R_B, R_A and S. The recommended value of a_F, b are 0.5 and $c = \frac{1}{2}\arg\max(\lambda_i^2), i = 1,2,3$.

To compare the different performance of the three line filter enhancement methods, different data sets, including *in vivo, in vitro* and simulated data have been chosen to calculate the contrast ratio improvement. The contrast ratio (CR) of the whole volume CR_W is defined as:

$$CR_W = \frac{\overline{I}(V_{nd})}{\overline{I}(V_{bg})} \tag{3.13}$$

here, V_{nd} includes the needle voxels and V_{bg} includes the background voxels. $\overline{I}(\cdot)$ calculates the mean intensity of the voxels. The contrast ratio improvement Ψ is defined as:

$$\Psi = \frac{CR_W^{lf}}{CR_W^{ori}} \tag{3.14}$$

Here, CR_W^{lf} is the contrast ratio of the line filtered volume, CR_W^{ori} is that of the original volume.

The best improvement in CR_W is obtained with Frangi's method (Table 3-1) The computation time which is dominated by filtering and calculating the eigenvalues, depends linearly on the size of the US volume, and is almost identical for all methods (about 3s for the simulated data using MATLAB).

Table 3-1 Mean contrast ratio improvement for the three line-enhancement methods and three groups of experiments. The best result in each row is set in bold.

Data type	Type of line filter		
	Frangi	Sato	Li
Simulation	**12.8**	3.4	6.5
PVA	**16.8**	4.0	3.1
Breast biopsy	**4.5**	2.3	1.9

According to Table 3-1, Frangi's line filter enhancement is chosen as an efficiently contrast enhancement method. Using equations (3.9) - (3.12), a tubular volume can be generated using the original 3D US volume, and in the tubular volume, the structure of the needle is well enhanced and the background noise is reduced, too. Thus, for the initialization of ROI, the tubularness of the US volume is processed instead of the voxels' intensity.

3.2.2 Initialization of ROI

In 3D US volumes, the needle appears as a tubular structure, so the line filter method can be implemented for the enhancement of the contrast of the needle and background tissue. Considering the shape of the biopsy needle and effective limitation of the size of the region, the ROI can be defined as a cylinder of radius R_{ROI} and length L.

Suppose that $l(t;\mathbf{A})$ represents the axis of the needle. It is a spatial parametric polynomial curve $\Re \to \Re^3$ given as:

$$l(t;\mathbf{A}) = \begin{bmatrix} a_{11} & \cdots & a_{1n} \\ a_{21} & \cdots & a_{2n} \\ a_{31} & \cdots & a_{3n} \end{bmatrix} \begin{bmatrix} 1 \\ \vdots \\ t^{n-1} \end{bmatrix}, t \in \Re \tag{3.15}$$

where, $\mathbf{A}$ is the curve coefficient matrix, and t is a curve parameter. A straight spatial line is modeled using $n=2$; a C-like bending situations is modeled by $n=3$; some higher ordered curves can also be presented by larger n (e.x. $n=4$ can represent S-like shapes). The parametric curve can be determined by n control points N_1 to N_n. To define the cylinder like ROI, a straight axis is needed, thus, the solving process of straight parametric line is presented. Two control points N_1, N_2 are needed for the solution. The RANSAC algorithm (Section 3.3.2) is used for selecting these two points. With N_1 and N_2, the two parameters t_1 and t_2 can be set as:

$$\begin{aligned} t_1 &= 0 \\ t_2 &= \left\| N_1 - N_2 \right\| \end{aligned} \tag{3.16}$$

Then, the matrix $\mathbf{A}$ can be solved as follows:

$$\mathbf{A} = \begin{bmatrix} N_1 & N_2 \end{bmatrix} \begin{bmatrix} 1 & 1 \\ t_1 & t_2 \end{bmatrix}^{-1} \tag{3.17}$$

Finally, the line $l(t;\mathbf{A})$ can be determined. To effectively limit the ROI, the length L of the ROI is determined according to the steps: i) knowing the pre-set geometry of the US volume, the two boundary points B_1 and B_2 can be located as the intersection of the line $l(t;\mathbf{A})$ and the volume boundary; ii) using the tubular volume, the intensities of the voxels along the line segment $\overline{B_1B_2}$ can be calculated; iii) registering the coordinates of the voxels along $\overline{B_1B_2}$ and the intensity values. In the tubular volume, only the needle part appears bright, therefore, the boundary point with the higher intensity value is considered as the insertion point. With the tip point N_{tip} found by RANSAC (Section 3.3.1.2), and an empirical bias δ, L is calculated as:

$$L = \left\| N_{tip} - B_i \right\| + \delta, i = 1 \, or \, 2 \tag{3.18}$$

Here, the insertion point B_i is determined automatically by comparing the intensities of the boundary points B_1, B_2.

Note V_{roi} as the subset of the voxels within the ROI. Then the V_{roi} satisfies the following condition:

$$V_{roi} = \{M \in V \mid d\left(M, \overline{B_i N_{tip}}\right) \leq R_{ROI}\}, i = 1 \, or \, 2 \tag{3.19}$$

Here, $d\left(M, \overline{B_i N_{tip}}\right)$ is the Euclidian distance from the point M to the line segment $\overline{B_i N_{tip}}$. Once the V_{roi} is obtained, the initialization of ROI is finished. The properties of ROI (*e.g.*: the radius, the length and the sub-set of voxels) is stored for further utilization of the ROI-RK algorithm.

3.3 Step 2: Tracking procedure

3.3.1 General aspects of methodology

3.3.1.1 Introduction of Kalman filter

The Kalman filter was published by R. E. Kalman in 1960 [Kalman (1960)]. It is an optimal recursive data-processing algorithm. Optimal means minimizing the mean of the squared error; Recursive means that the Kalman Filter does not require all previous data to be kept in storage and reprocessed every time when a new measurement is taken [Maybeck (1979)]. The Kalman filter is a set of mathematical equations that provide an efficient computational means of estimating the state of a process, in a way that minimizes the mean of the squared error [G Welch *et al.* (2006)]. This filter is powerful to estimate the past, present and even the future state of a system and it is very useful for the prediction of a needle's positions.

Equations of Kalman filter

The Kalman filter addresses the general problem of trying to estimate the state $\mathbf{s} \in \Re^n$ of a discrete-time controlled process, and the linear stochastic difference equation is:

$$\mathbf{s}_k = \mathbf{F}\mathbf{s}_{k-1} + \mathbf{B}\mathbf{u}_{k-1} + \mathbf{w}_{k-1} \tag{3.20}$$

In the equation (3.20), $\mathbf{F}\left(n \times n\right)$ is the state transition matrix which relates the state at the previous time step $k-1$ to the current step *k*. $\mathbf{F}$ might change with each time step. However, if the system is stable, $\mathbf{F}$ is a constant matrix. $\mathbf{B}\left(n \times l\right)$ is the control matrix and vector $\mathbf{u}_{k-1}$ is the control vector. Sometimes these two variables are ignored. The random vector $\mathbf{w}_{k-1}$ represents the process noise.

There is also a measurement vector $\mathbf{z} \in \Re^m$

$$\mathbf{z}_k = \mathbf{H}\mathbf{s}_k + \mathbf{v}_k \tag{3.21}$$

Here, $\mathbf{H}(m \times n)$ is the measurement matrix which relates the state $\mathbf{s}_k$ to the measurement $\mathbf{z}_k$. For a stable system, matrix $\mathbf{H}$ is also a constant. The random vector $\mathbf{v}_k$ represents the measurement noise. Normally, $\mathbf{w}_k$ and $\mathbf{v}_k$ are assumed to be independent of each other, white and with Gaussian distribution.

$$p(\mathbf{w}) \sim N(\mathbf{0}, \mathbf{Q}) \tag{3.22}$$

$$p(\mathbf{v}) \sim N(\mathbf{0}, \mathbf{R}) \tag{3.23}$$

$\mathbf{Q}$ and $\mathbf{R}$ are the processing error covariance and measurement error covariance respectively. $N(\cdot)$ represents the Gaussian distribution.

Since the Kalman filter is about the prediction and correction, two definitions of errors are introduced: the *a priori* estimate error $\mathbf{e}_k^-$ and *a posteriori* estimate error $\mathbf{e}_k$:

$$\mathbf{e}_k^- \equiv \mathbf{s}_k - \hat{\mathbf{s}}_k^- \tag{3.24}$$

$$\mathbf{e}_k \equiv \mathbf{s}_k - \hat{\mathbf{s}}_k \tag{3.25}$$

Here, $\hat{\mathbf{s}}_k^- \in \Re^n$ is the *a priori* state estimate at the step *k* without the measurement $\mathbf{z}_k$, and $\hat{\mathbf{s}}_k \in \Re^n$ is the *a posteriori* estimate at step *k* with the measurement $\mathbf{z}_k$. The definition of the *a priori* estimate error covariance $\mathbf{P}_k^-$ and the *a posteriori* estimate error covariance $\mathbf{P}_k$ is:

$$\mathbf{P}_k^- = E\left[\mathbf{e}_k^- \mathbf{e}_k^{-T}\right] \tag{3.26}$$

$$\mathbf{P}_k = E\left[\mathbf{e}_k \mathbf{e}_k^T\right] \tag{3.27}$$

All the above is the preparation. To derivate the five main equations of Kalman filter, there are mainly two methods: the innovation method [Haykin (2003)] and the Bayesian method [Z Chen (2003)]. Both derivation methods lead to the same results for Kalman filter. The Kalman filter estimates a process by using a form of feedback control [G Welch *et al.* (2006)]. The equations of the Kalman filter can be divided into two groups: the time update equations (predictor equations) and the measurement update equations (corrector equations). The time update equations are given as below:

$$\hat{\mathbf{s}}_k^- = \mathbf{F}\hat{\mathbf{s}}_{k-1} + \mathbf{B}\mathbf{u}_{k-1} \tag{3.28}$$

$$\mathbf{P}_k^- = \mathbf{F}\mathbf{P}_{k-1}\mathbf{F}^T + \mathbf{Q} \tag{3.29}$$

The measurement update equations are given as below:

$$\mathbf{K}_k = \mathbf{P}_k^- \mathbf{H}^T \left(\mathbf{H}\mathbf{P}_k^- \mathbf{H}^T + \mathbf{R}\right)^{-1} \tag{3.30}$$

$$\hat{\mathbf{s}}_k = \hat{\mathbf{s}}_k^- + \mathbf{K}_k\left(\mathbf{z}_k - \mathbf{H}\hat{\mathbf{s}}_k^-\right) \tag{3.31}$$

$$\mathbf{P}_k = \left(\mathbf{I} - \mathbf{K}_k\mathbf{H}\right)\mathbf{P}_k^- \tag{3.32}$$

Here $\mathbf{K}_k$ is the Kalman gain, $\mathbf{z}_k - \mathbf{H}\hat{\mathbf{s}}_k^-$ is the innovation.

The Kalman filter is a recursive minimum mean square error (MMSE) predictor – corrector. Fig. 3-2 shows the two basic steps: a) prediction step: the time update is taken where the one-step forward prediction of observation is calculated; b) correction step: the measurement update is taken where the correction to the estimate of the current state is calculated.

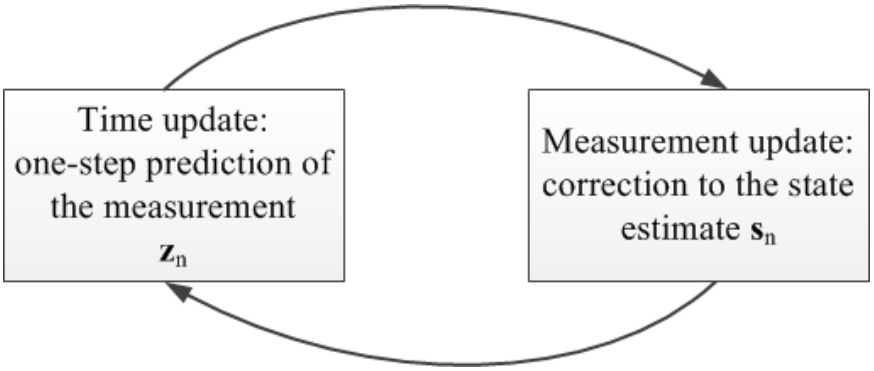

Fig. 3-2 Schematic illustration of the discrete Kalman filter cycle

Inter-relationship of Kalman filter

In the macro view, the Kalman filter is a set of five equations, as shown in (3.28) - (3.32). However, because the estimated state could be influenced by the processing noise and the measurement noise, the inter-relationship of the Kalman filter cannot be ignored.

In equation (3.29), *a priori* estimate error covariance $\mathbf{P}_k^-$ has relationship with *a posteriori* estimate error covariance $\mathbf{P}_{k-1}$ and the process noise covariance $\mathbf{Q}$. Here two possibilities for $\mathbf{Q}$ are considered: 1) it is small enough that its influence can be ignored; 2) it is too large to ignore its influence. In the situation 1), accompanied with the decrease of process noise covariance $\mathbf{Q}$, the prediction result of measurement update step gets closer to the *a priori* estimate result $\hat{\mathbf{s}}_k^-$; In the situation 2), with the increasing of the process noise covariance $\mathbf{Q}$, the prediction result of measurement update step is closer to the measurement $\mathbf{z}_k$. The value of matrix $\mathbf{Q}$ illustrates that the model chosen is well fitting or not to some extent. If $\mathbf{Q}$ is too large, it indicates that the model chosen does not go well with the real situation. It is then better to change the model for a better fitting one. In the subsequent chapters, we suppose that

the model chosen fits well to the real situation. The matrix $\mathbf{Q}$ is set small enough and its influence to $\mathbf{P}_k^-$ and $\mathbf{K}_k$ can be ignored.

Now, consider the relationship among Kalman gain $\mathbf{K}_k$, $\mathbf{P}_k^-$ and measurement error covariance matrix $\mathbf{R}$. The equation (3.30) can be written as:

$$\mathbf{K}_k = \frac{\mathbf{P}_k^- \mathbf{H}^T}{\left(\mathbf{H}\mathbf{P}_k^- \mathbf{H}^T + \mathbf{R}\right)} \tag{3.33}$$

from (3.33), it can be seen that if the influence of measurement error covariance $\mathbf{R}$ can be ignored, the Kalman gain $\mathbf{K}_k$ is equal to $\mathbf{H}^-$, thus from the equation (3.31), it is easy to get that:

$$\hat{\mathbf{s}}_k = \mathbf{H}^- \mathbf{z}_k \tag{3.34}$$

It shows that the prediction state $\hat{\mathbf{s}}_k$ totally depends on the measurement $\mathbf{z}_k$, and this means that the measurement $\mathbf{z}_k$ is trusted. Another situation is that $\mathbf{P}_k^-$ gets closed to $\mathbf{0}$, and $\mathbf{K}_k$ is equal to $\mathbf{0}$. Thus $\hat{\mathbf{s}}_k = \hat{\mathbf{s}}_k^-$, and the correction of innovation $\mathbf{z}_k - \mathbf{H}\hat{\mathbf{s}}_k^-$, which contains the new information from the measurement, is ignored. In this situation, the result of Kalman filter is gradually turned to constant. The third situation is that the measurement error covariance $\mathbf{R}$ is large. From equation (3.33), it is obvious that the larger the $\mathbf{R}$ is, the smaller the $\mathbf{K}_k$ is. From equation (3.31), it can be seen that the *a priori* estimation $\hat{\mathbf{s}}_k^-$ is then more trusted than the measurement $\mathbf{z}_k$. This means that when the measurement noise is large, the Kalman filter inclines to the *a priori* estimation but not the measurement $\mathbf{z}_k$. With the experience of the inter relationships, the best fitting parameters of Kalman filter can be set.

3.3.1.2 Introduction of RANSAC algorithm

The RANSAC algorithm was first presented by M. Fischler and R. Bolles in 1981. Using a sample set containing a large portion of noise, the RANSAC uses the smallest possible set to form the model. During the context of parameters estimation, two terms are defined: inliers and outliers. The term “inliers” denotes the points which consist of the best model. The rest of the points are denoted as “outliers”, which can be considered as the noise for the model. The model is qualified using a cost function defined by the user.

RANSAC is an iterative algorithm. During each iteration, n distinct points $N_i, i = 1, \cdots, n$ are randomly selected from the input data set V to form the model, for example, if the model is a C-like curved line, $n = 3$. The set is defined as $N = \{N_i, i = 1, ..., n\}$. After the set is chosen, a classification function $q(\cdot)$ is used to choose the inliers set V_{inl} from V using the parameter A calculated from the set N:

$$V_{inl}(A) = \{N \in V \mid q(A) = 1\} \tag{3.35}$$

The initial number of iterations J is set to $J_{\max}$ (typically a few hundreds, to arrive at the most appropriate fitting model). However, the RANSAC algorithm has the capacity to update the iteration number adaptively. When a better model is found, the number of iteration is updated using [Fischler *et al.* (1981); Torr *et al.* (1998)]:

$$J = \frac{\ln(1-\eta)}{\ln(1-\zeta^n)}, \text{ with } \zeta = \frac{|V_{inl}|}{|V|} \tag{3.36}$$

Here, ζ is the inliers ratio and η is a parameter pre-defined by the user, which indicates a desired probability that RANSAC succeeds; $P = \zeta^n$ is the probability that n randomly selected points are all from the V_{inl}.

Input:

V – a set of points

$q(\cdot)$ – the classification function for choosing V_{inl}

n – minimum number of points required to calculate the model

C – the cost function for qualifying the model

Output:

V_{inl}^* – the best set of inliers for the expected model

$L(\cdot)$ – the best fitting model

Algorithm:

Initialize: $j = 1, J_{\max}, C_0$

While $j \le J_{\max}$

Randomly selected N_j from V

Calculate A_j using N_j, choose V_{inl}^j using $q(A_j)$

Calculate cost function C_j using V_{inl}^j

If $C_j \le C_{j-1}$

Calculate J using (3.36) and set $J \to J_{\max}$

Save $L^*(\cdot) = L^j(\cdot)$ as the best fitting model, $V_{inl}^* = V_{inl}^j$ as the best set of inliers

$j = j + 1$

End while

Table 3-2 Summary of RANSAC algorithm.

Table 3-2 gives a summary of RANSAC algorithm. The details of our tool model and inliers classification function are presented in section 3.3.2.2.

3.3.2 Implementation of methodology

3.3.2.1 Mathematical model for Kalman filter

Since the Kalman filter is a linear quadratic estimation. It is based on linear dynamic systems discrete in the time domain. For dynamic targets, the constant velocity (CV) model and the constant accelerating (CA) model are the most common used [Chang *et al.* (1984)].

In the CV model, the state vector normally contains six variables:

$$\mathbf{s} = \left[x, v_x, y, v_y, z, v_z \right] \tag{3.37}$$

Here, (x, y, z) is the Cartesian coordinate of the target, v_x , v_y and v_z are the velocities in the directions x, y and z respectively.

When the target being tracked is accelerating, the CA model is sometimes used. The state vector

$$\mathbf{s} = \left[x, v_x, a_x, y, v_y, a_y, z, v_z, a_z \right] \tag{3.38}$$

Here, a_x, a_y and a_z are the accelerations in the direction x, y and z respectively. Note that in the above two models, the different variables along the x, y and z direction are independent.

The objective of the ROI-RK method is to stably track the position of a biopsy needle controlled manually. Normally, when the surgeon inserts the needle for biopsy or minimally invasive surgery, he performs a stable procedure. The needle is controlled to steadily forward to the affected part. Therefore, the CV model for Kalman filter is selected in this situation. Although, in [Roberts (1988)], the author claimed that a 3D line can be fixed using only four parameters, according to the localization algorithm chosen, five parameters are used to fix a line in the 3D space. These parameters are chosen as direction angles α (the angle between the needle and the plane xoz, Fig. 3-3 b), β (the needle-beam angle Fig. 3-3 b), and the position of the needle tip $\mathbf{p}_t(x_t, y_t, z_t)$ (needle end point, Fig. 3-4). Since the insertion of the needle and the mechanical transducer are controlled manually, it is hard to know the inserting speed at one moment. Moreover, the needle in the US volume is not only moving along the axis direction, but a rotation and even motion along the z-axis can also occur. As a result, the speed of variation v_α, v_β of the two angles α, β and speed of the needle tip $\mathbf{v}_t$ should be included in the state vector.

Using the CV model, the state vector $\mathbf{s}$ in our system is set as $\mathbf{s} = [\beta, \alpha, v_\beta, v_\alpha, \mathbf{p}_t, \mathbf{v}_t]^T$, and the time update equations are as:

$$\hat{\mathbf{s}}_k^- = \mathbf{F}\hat{\mathbf{s}}_{k-1} \tag{3.39}$$

$$\mathbf{P}_k^- = \mathbf{F}\mathbf{P}_{k-1}\mathbf{F}^T + \mathbf{Q} \tag{3.40}$$

Here $\mathbf{F}=\begin{bmatrix}\mathbf{I}_{2\times2} & dt\times\mathbf{I}_{2\times2} & \mathbf{0}_{2\times6}\\ \mathbf{0}_{2\times2} & \mathbf{I}_{2\times2} & \mathbf{0}_{2\times6}\\ \mathbf{0}_{3\times4} & \mathbf{I}_{3\times3} & dt\times\mathbf{I}_{3\times3}\\ \mathbf{0}_{3\times4} & \mathbf{0}_{3\times3} & \mathbf{I}_{3\times3}\end{bmatrix}$, $\mathbf{p}_t=(x_t,y_t,z_t)$ is the position vector of the needle tip, and $\mathbf{v}_t=[v_{tx},v_{ty},v_{tz}]$ is the velocity vector of the needle tip, dt represents the time interval. The processing noise is assumed as Gaussian, which is the classic processing noise used in Kalman filter [Kalman (1960)].

The measurement vector $\mathbf{z}$ is set as $\mathbf{z}=[\beta,\alpha,\mathbf{p}_t,\mathbf{v}_t]^T$. The angular velocities v_α, v_β are not included in $\mathbf{z}$ because: (a) the inserting path of the needle is always along the axis direction, the expected angular velocities are considered as $v_\alpha=v_\beta=0$; (b) there is not suitable method to measure the angular velocities. The minor deviations of the angles are treated as the measurement noise. The two angles α, β and the tip position $\mathbf{p}_t$ can be measured by the RANSAC algorithm (Section 3.3.2). The inserting velocity (tip velocity) $\mathbf{v}_t$ can be estimated by a motion estimation method (Section 3.3.2.3). According to equation (3.21), the measurement matrix is $\mathbf{H}=\begin{bmatrix}\mathbf{I}_{2\times2} & \mathbf{0}_{2\times8}\\ \mathbf{0}_{6\times4} & \mathbf{I}_{6\times6}\end{bmatrix}$. The measurement noise is also a Gaussian distribution that is estimated by a large number of repeat trials. In the case of a robotic-driven needle insertion, there is a control vector $\mathbf{u}$ and control matrix $\mathbf{B}$ as input. In our application, the needle is actuated by hand. The control input is unknown, thus the $\mathbf{B}$ and $\mathbf{u}$ in equation (3.28) are set to zero. The next two sections introduce the RANSAC algorithm and the motion estimation method which afford the measurements to the Kalman filter.

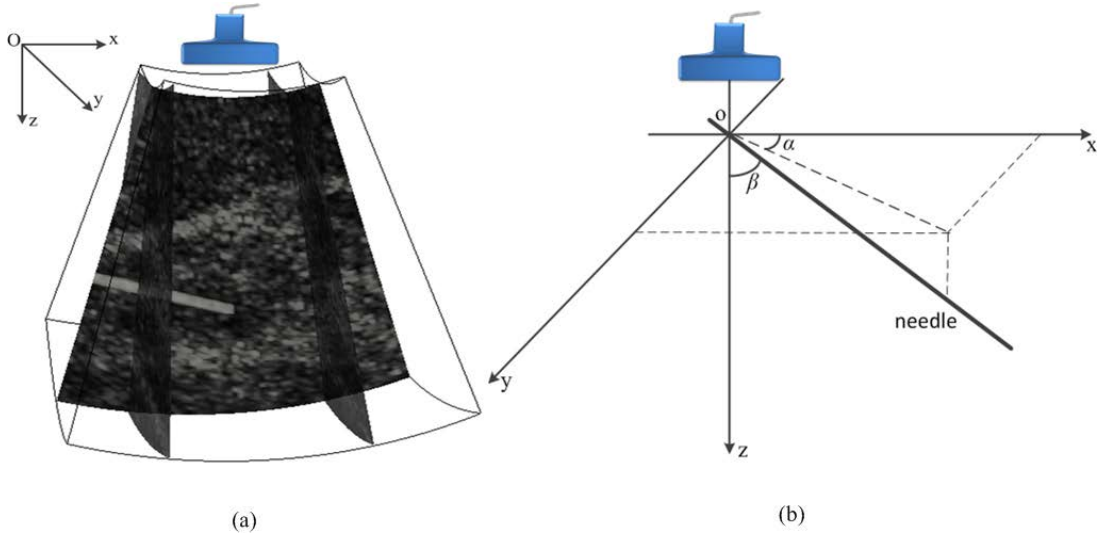

Fig. 3-3 The definition of the Cartesian coordinate relevant to the probe and the two inserted directional angle α, β of the needle: (a) an example of 3D US volume; (b) a diagrammatic sketch of the two angles of the needle.

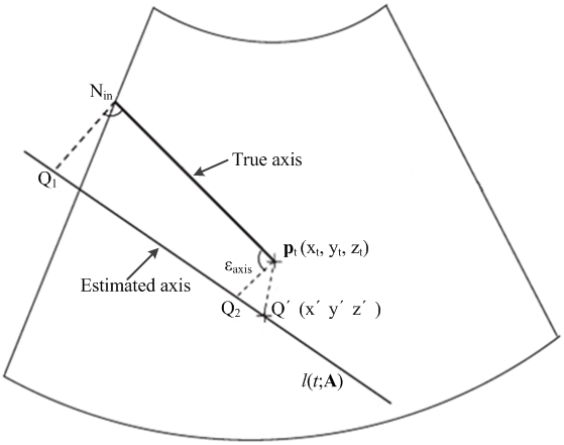

Fig. 3-4 The definition of parameters in the needle frame.

3.3.2.2 RANSAC procedure for Biopsy needle localization

The biopsy needle localization method using RANSAC algorithm in 3D US volumes was first introduced by M. Barva [Barva (2007)], then improved by M. Uherčík [Uherčík *et al.* (2010)]. It is able to localize a straight needle inserted in one 3D US volume. The RANSAC procedure consists of four steps: (i) intensity classification; (ii) axis localization; (iii) local optimization; (iv) tip localization. The output of the algorithm consists of $l(t;\mathbf{A})$, the axis equation of the needle after the local optimization and $\mathbf{p}_t$, the tip position which is directly calculated from the

RANSAC procedure. The following four parts introduce the details of the steps of the needle localization procedure.

Intensity classification

The classification procedure aims at reducing the number of voxels being processed. The voxels are separated into two disjoint sets by classifying their intensities by a threshold. V_{th} is the set of voxels whose intensities are larger than the threshold value I_{th} and V_b is considered as the set of voxels from the background:

$$\begin{aligned} V_{th} &= \{M \in V \mid I(M) \geq I_{th}\} \\ V_b &= V - V_{th} \end{aligned} \tag{3.41}$$

M. Barva has proposed to choose the threshold value as 95 % quantity of the input data by fitting a Gamma distribution [Barva (2007)]. However, manually segmenting the 3D US volume, we found that the needle voxels represent less than 1 % of the whole volume [Zhao *et al.* (2013)]. So, the choice of the threshold value is proposed in order to correspond to the assumption that 99% of the voxels are from the background surrounding tissue. Even under this assumption, V_{th} also contains some non-needle voxels whose intensity is larger than I_{th}.

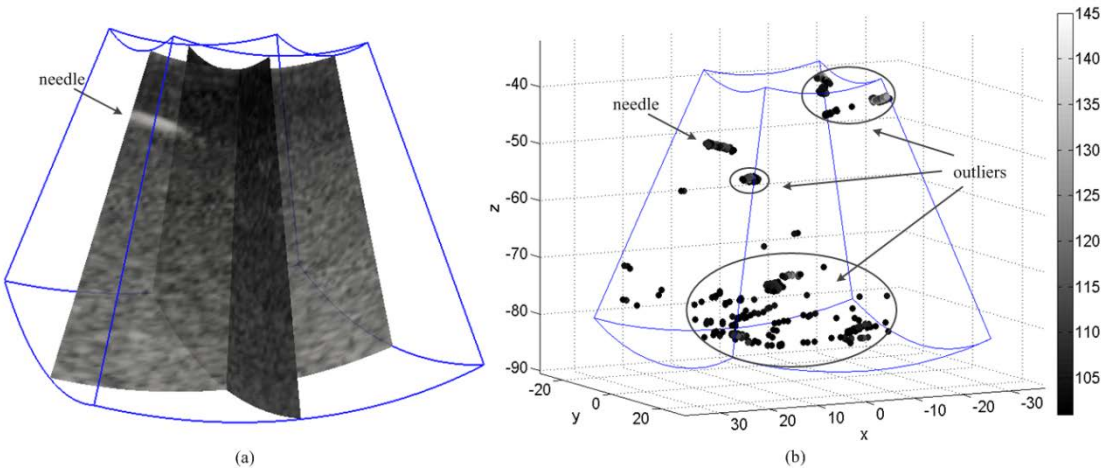

Fig. 3-5 A 3D US volume and the remaining voxels after the thresholding: (a) the US volume is obtained by scanning an agar phantom with a metal biopsy needle. A part of the needle can be seen in the volume. (b) The remaining voxels after the intensity classification. In the image, not only the voxels of the needle, but a great number of outliers whose intensity is higher than the threshold value are remaining. These outliers influence the result of MF-RANSAC algorithm.

Axis localization

The RANSAC algorithm is used in this step to estimate the axis as the position of the needle by fitting a given model. In this case, the input data set is the thresholded voxels V_{th} and a model classifier function $q(M;\mathbf{A})$. The output of RANSAC is the estimated axis and the data set of inlier voxels $\hat{V}_{inl}$ corresponding to this axis.

According to the assumption (b), the shape of biopsy needle is a 3D straight line. In our application, the minimum number of data for fitting the model is set as $n=2$, thus the point set $N=\{N_i, i=1,2\}$. To further limit the possibilities of different combinations of the two points, the shortest expected length of needle $d_{\min}$ is set. Samples with $\kappa(N)<d_{\min}$ are rejected, where $\kappa(\cdot)=\|N_i-N_j\|, i\neq j$. After the set is chosen, the coefficient matrix $\mathbf{A}$ can be calculated using (3.17), and the set of inliers can be obtained using the classification function $q(M;\mathbf{A})$:

$$V_{inl}(\mathbf{A})=\{M\in V_{th} \mid q(M;\mathbf{A})=1\} \tag{3.42}$$

In the previous work, M. Uherčík has proposed two tool models for needle localization in 3D US [Uherčík (2011)]: the model axis shape (AxShp) and model intensity distribution (IntDstr). Since the needle appearance in the US volume is more like a line segment, a model segment shape (SegShp) is proposed here. Instead of calculating the point-to-line distance, the point-to-segment distance is calculated. Because the line segment has a fixed length, through the SegShp model, a more precise inliers data set can be obtained.

Model SegShp. This model only evaluates the distances of the point $M(x,y,z)\in V_{th}$ to the estimated line segment $\overline{N_{in}N_{end}}$. This model does not need any *a priori* information on the intensity values, so no pre-trained models are needed, which ensures that this model is appropriate on all kind of data sets. A classifier function $q_{Seg}(M;\mathbf{A})\in\{0,1\}$ is defined as:

$$q_{Seg}(M;\mathbf{A})=\begin{cases}1, & \text{if } d(M;\mathbf{A})<r\\ 0, & \text{otherwise}\end{cases} \tag{3.43}$$

Here, the matrix $\mathbf{A}=\begin{bmatrix}x_{in} & x_{end}\\ y_{in} & y_{end}\\ z_{in} & z_{end}\end{bmatrix}$, where $N_{in}(x_{in},y_{in},z_{in})$, $N_{end}(x_{end},y_{end},z_{end})$ are the two distinct end points; r is the expected radius of the needle in the image, it has a relationship with the PSF function of the US system. The point to curve distance d is defined as the Euclidean distance from one point N to the line segment $\overline{N_{in}N_{end}}$. To

calculate this distance, it should judge first that if the projection of N is on the segment or not. The flag g is calculated as:

$$g = \frac{(M - N_{in})(N_{end} - N_{in})}{\|N_{in}N_{end}\|^2}, \forall M \in V_{th} \tag{3.44}$$

Here, $M(x, y, z)$ is an arbitrary point from the voxel set V_{th}. $\|\cdot\|$ represents the length of the segment $\overline{N_{in}N_{end}}$. There are three possible positions for the projection of the point M: if $g \in [0,1]$, it means that the projection is on $\overline{N_{in}N_{end}}$; if $g < 0$, the projection is on the left extension line of $\overline{N_{end}N_{in}}$; if $g > 0$, the projection is on the right extension line of $\overline{N_{in}N_{end}}$. So $d(M;\mathbf{A})$ has also three possibilities:

$$d(M;\mathbf{A}) = \begin{cases} \|MM'\|, & g \in [0,1] \\ \|MN_{in}\|, & g < 0 \\ \|MN_{end}\|, & g > 0 \end{cases} \tag{3.45}$$

Here, M' is the projection of the point M. When the projection is on the extension of the segment, instead of calculating the distance of the point and its projection, the distance from the point to the nearer end point of the segment is calculated. All the points satisfy the condition $q_{seg}(M;\mathbf{A}) = 1$ are considered as the inliers V_{inl}, the other records are outliers. To evaluate the fitness of the inliers V_{inl} with respect to line segment $\overline{N_{in}N_{end}}$, a cost function is defined:

$$C(V_{inl};\mathbf{A}) = \sum_{M \in V_{inl}} d(M;\mathbf{A}) \tag{3.46}$$

Once $\overline{N_{in}N_{end}}$ is chosen, $C(V_{inl};\mathbf{A})$ is calculated. According to the value of cost function, the best-fitting model can be chosen. This best value is used in the step of optimization.

Local optimization

Since the RANSAC algorithm can give only approximate axis position, local optimization is used to get a more accurate result. The local optimization procedure is only done with the estimated set of inliers $\hat{V}_{inl}$ [Uherčík *et al.* (2010)]. Instead of optimizing the coefficient matrix $\mathbf{A}$, the optimization is affected on the position of control points N_1, N_2 because it is more stable and easy to implement.

The optimization step depends on a local coordinate system $\mathbf{P}$, which is calculated using $\hat{V}_{inl}$ by principal component analysis (PCA). The principle direction is $\mathbf{p}_1$

corresponding to the largest eigenvalue λ_1. The other two directions $\mathbf{p}_2$ and $\mathbf{p}_3$ are arranged as $|\lambda_2| \geq |\lambda_3|$. The directions $\mathbf{p}_2$ and $\mathbf{p}_3$ have more influence than the principle direction $\mathbf{p}_1$. So the control points $\hat{N}_1$, $\hat{N}_2$ are re-parameterized using a 2×2 matrix $\mathbf{M}$ as

$$\left[N_1\ N_2\right] = \left[\hat{N}_1\ \hat{N}_2\right] + \left[\mathbf{p}_2\ \mathbf{p}_3\right]\mathbf{M} \tag{3.47}$$

The initial value of $\mathbf{M}$ is $\mathbf{M} = \mathbf{0}$. The new coefficient matrix $\mathbf{A}(\mathbf{M})$ is calculated by control points $\left[N_1\ N_2\right]$ according to the equation (3.17). Once $\mathbf{A}(\mathbf{M})$ is fixed, a new line $l\left(t;\mathbf{A}(\mathbf{M})\right)$ in the local coordinate system $\mathbf{P}$ is obtained. A local cost function is defined as:

$$C_{\mathbf{P}}\left(\hat{V}_{inl};\mathbf{A}(\mathbf{M})\right) = \sum_{N\in V_{inl}} d\left(M;\mathbf{A}(\mathbf{M})\right) \tag{3.48}$$

A more accurate axis position is found by optimizing the cost function:

$$\mathbf{A}^* = \arg\min_{\mathbf{M}} C_{\mathbf{P}}\left(\hat{V}_{inl};\mathbf{A}(\mathbf{M})\right) \tag{3.49}$$

The optimization uses a derivative-free Nelder-Mead downhill simplex method [Nelder *et al.* (1965)].

Tip localization

Once the optimal axis has been found, the tip estimation process begins. The tip position is estimated by analyzing the intensity along the estimated axis. According to Assumption (a) (section 0), on the needle axis the voxel intensities drop sharply at the end of the needle. The needle is inserted from the outside, thus there is only one tip needed to be located in the image. All the intensities of the voxels along the optimal axis are calculated, and a significant drop below the threshold value is considered as the tip position, shown in Fig. 3-6.

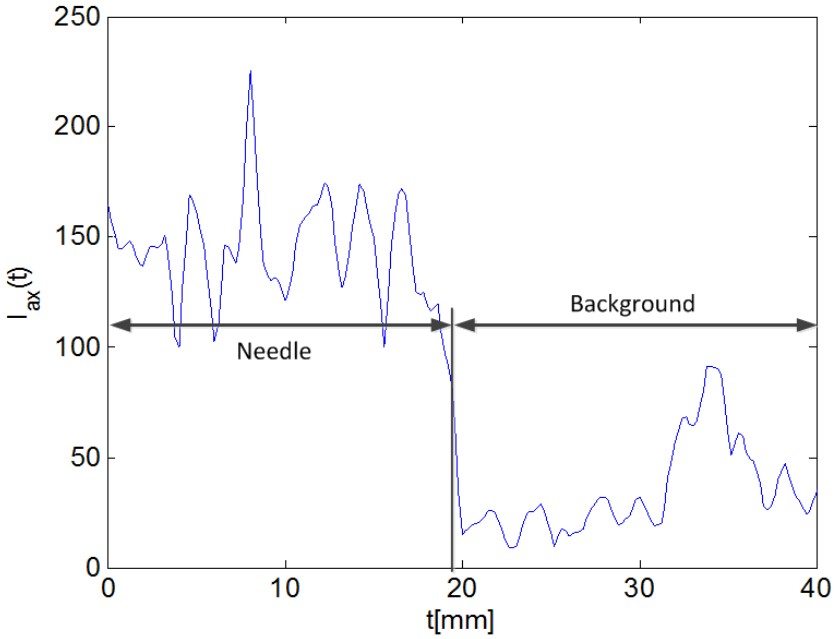

Fig. 3-6 Illustration of the intensity curve along the needle axis

3.3.2.3 Motion estimation

In medical ultrasound, there are different state-of-the art algorithms for motion estimation, for example, block-matching and optical flow. The speckle tracking method, which belongs to the branch of block-matching algorithms, is selected here because it can directly track the backscattered echoes generated by ultrasonic scatterers in tissue [Building (2000)]. This method was first described by Robinson *et al.* [Robinson *et al.* (1982)], and then applied by Trahey *et al.* [Trahey *et al.* (1987)]. It was first used to detect the blood velocity with ultrasound data. It estimates velocities based on the displacement of a speckle pattern in the axial, lateral, and elevation directions.

In our applications, the expected motion of the speckle pattern of the background tissue is stationary, except that when the needle is inserted, it is sheared apart. The motion of the speckle pattern of the needle is a translation motion along the axis direction, and there is no deformation along the insertion direction because the needle is thick enough. However, considering that there could be a slight relative motion between the needle and the probe, as pressing and rotating, there can be a movement of the axis within the ROI in the 3D volume. Here, the speckle tracking method is used to measure the speed of the needle tip $\mathbf{v}_t$. Firstly, a small 3D region is chosen in the first volume as the kernel region, which is selected according to the coordinates of the estimated tip position. Then, a larger region is chosen as a searching region in the second volume. During the tracking procedure, the kernel region slides voxel by voxel

in the searching region, and the normalized cross correlation (NCC) is used to compare the similarity between the kernel region and the searching region. The 3D NCC is given as:

$$\rho(a,b,c)=\frac{\sum_{i=1}^{m}\sum_{j=1}^{n}\sum_{k=1}^{p}\left[\mathbf{X}_0(i,j,k)-\bar{\mathbf{X}}_0\right]\left[\mathbf{X}_1(i+a,j+b,k+c)-\bar{\mathbf{X}}_1\right]}{\sqrt{\sum_{i=1}^{m}\sum_{j=1}^{n}\sum_{k=1}^{p}\left[\mathbf{X}_0(i,j,k)-\bar{\mathbf{X}}_0\right]^2\sum_{i=1}^{m}\sum_{j=1}^{n}\sum_{k=1}^{p}\left[\mathbf{X}_1(i+a,j+b,k+c)-\bar{\mathbf{X}}_1\right]^2}} \tag{3.50}$$

with ρ the correlation coefficient, $\mathbf{X}_0$ the kernel region, whose size is $m\times n\times p$, and $\mathbf{X}_1$ the searching region, size $M\times N\times P$. The size of ρ is related to the sizes of $\mathbf{X}_0$ and $\mathbf{X}_1$, its size is $(M-m+1)\times(N-n+1)\times(P-p+1)$. However, the traditional NCC does not match all the requirements of real-time applications; for this point, the fast normalized cross correlation algorithm (FNCC) [Lewis (1995)] is chosen to overcome this difficulty. To calculate the numerator of (3.50), the fast Fourier transform (FFT) is used to transfer the numerator part to the 3D frequency domain. After the multiplication, the inverse FFT (IFFT) is applied to turn back the result to the spatial domain. The denominator part is calculated using the summed-area tables algorithm [Crow (1984)], which effectively reduces the processing time. With the FNCC algorithm, the computational efficiency is improved compared with the normal NCC algorithm. The best matching region is $\rho=\rho_{\max}$. The difference of coordinate between the kernel region and the best matching region indicates the displacement of the needle, thus the speed of the needle is obtained by dividing the displacement by time. It is used as an input measurement of the Kalman filter mentioned in the section 3.3.2.1.

3.3.2.4 Tracking loop

Once the ROI is initialized, the tracking procedure begins. The RANSAC algorithm (described in section 3.3.2) runs in this ROI to obtain the needle axis $l(t;\mathbf{A})$ and tip position $\mathbf{p}_t$. Since the needle axis is estimated using the RANSAC algorithm, the unit vector of the axis $\mathbf{u}=\left[u_x,u_y,u_z\right]$ is easy to get, and the two angles α, β are calculated (Fig. 3-3 (b)):

$$\alpha=\arctan\left(\frac{u_y}{u_x}\right),\ \beta=\arccos\left(\frac{u_z}{\|\mathbf{u}\|}\right) \tag{3.51}$$

When the second volume comes, the inserting velocity $\mathbf{v}_t$ is obtained using the speckle tracking method (section 3.3.2.3). The initial velocities v_α, v_β are set to zero. The α, β, v_α, v_β, $\mathbf{p}_t$ and $\mathbf{v}_t$ are all used to initialize the Kalman filter. Since the

needle and the probe could have a relative motion, and the ROI is quite limited, the previous ROI may not be suitable for the next volume. Therefore, the *a priori* information is used for updating the new ROI, so that it can be adapted in the new coming US volume. The time updates equation of the Kalman filter is used to predict the new position of the ROI in the new coming volume by updating the needle position. Equation (3.39) is used to calculate the state vector $\hat{\mathbf{s}}_k^-$ based on the state vector $\hat{\mathbf{s}}_{k-1}$ of the $k-1$ step. From $\hat{\mathbf{s}}_k^-$, the predicted needle tip $\hat{\mathbf{p}}_{tk}^-$, the angles $\hat{\alpha}_k^-$, and $\hat{\beta}_k^-$ can be obtained. Using these three parameters, a 3D line segment can be fixed. It can be considered as the axis of the cylinder like ROI and the length of the segment is also the length of the cylinder. With a pre-defined radius, the predicted ROI can be defined. Then the RANSAC algorithm is applied in the updated ROI to get the components for measurement vector of the Kalman filter. After that, the measurement update equations (equations (3.30) - (3.32)) of the Kalman filter are used to optimally estimate the position of the needle, the *a posteriori* state vector $\hat{\mathbf{s}}_k$ can be calculated, and more precise position information of the needle is obtained. The frame that contains the needle and its perpendicular frame can be obtained using a strategy of interpolation with the original US volume and shown on the screen. All of this is a single loop in our method, and this loop continues until the end of the tracking procedure.

3.4 Summary and conclusion

In this chapter, the details of ROI-RK method have been presented. It mainly contains two steps: (a) ROI initialization step; (b) needle localization and tracking step. In step (a), to suppress the noise and automatically initialize the ROI, the Hessian matrix based line filter is implemented. The Frangi's line structure measurement is selected because the improvement of the contrast ratio is the best. In step (b), the RANSAC runs only in the ROI so that it is less influenced by outliers. A Kalman filter is implemented to update the ROI and auto-correct the needle localization result. Because the ROI-RK method is involved in a dynamic situation, a motion estimation strategy is also implemented to estimate the insertion speed of the biopsy needle. The next chapter focuses on quantifying the performance of the proposed technique using simulations.

Chapter 4

Simulation and Result

Contents

4.1 Simulation

To evaluate the performances of our proposed ROI-RK method, different series of 3D US volumes are simulated. In each series, the length of the needle is changed to simulate a dynamic situation. The $[\alpha, \beta]$ pairs and the contrast ratio (CR) are changed to simulate different situations of needle insertion. The inhomogeneous US background is simulated using Field II [Jensen *et al.* (1992); Jensen (1996)]. The density of scatterers is 10 scatterers / mm^3. The spatial arrangement of the background scatterers is chosen as a random uniform distribution. Then, all scatterers are assigned the intensities of voxels from a 3D US volume of breast tissue acquired with a GE Voluson E8 scanner using a 12MHz probe. This scattering map is chosen in order to have realistic images looking very "similar" to real images. The obtained images contain an inhomogeneous US background with complicated patterns such as line-like structures. Each 3D US volume is composed of 55 planes, 64 beams / plane, and 160 samples / beam. The sector angle φ is 34.5°, the total tilt angle θ is 38°. The sample frequency for the envelope is 2.5 MHz. The axial resolution is 0.3 mm, the lateral resolution is about 0.7 mm, and the azimuthal resolution is about 0.9 mm.

The needle voxels are added in the US volume in order to have a known ground truth position. Their intensity follows a distribution evaluated on experimental data. A $50\times50\times50$ mm^3 polyvinyl alcohol (PVA) cryogel phantom [Duboeuf *et al.* (2009)], containing 10% of PVA and 1% of silicate powder, was made and scanned with a Sonix MDP scanner equipped with a 4DC7-3/40 3D probe, after a thin metal needle

of 0.6 mm radius was inserted. The needle was manually segmented ten times by an expert. The corresponding amplitude distribution was estimated from eight scanned series of 3D US volumes. All the voxels of the needle were saved to generate the histogram of intensities and fitted with Gaussian distribution as represented in Fig. 4-1.

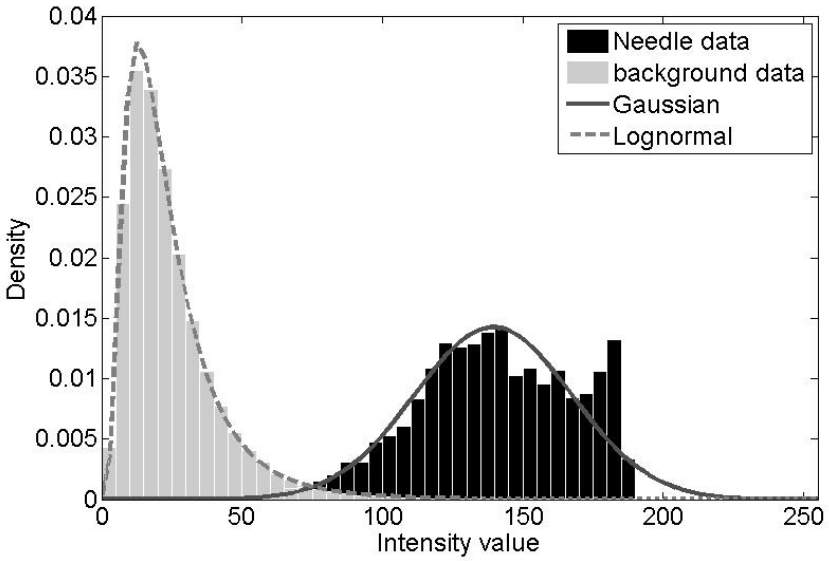

Fig. 4-1 Distribution of the background voxels and the needle voxels of the phantom used on simulation. The background voxels are fitted with a lognormal distribution, and the needle voxels are fitted with a Gaussian distribution.

In Fig. 4-1, the parameters of the Gaussian distribution of the needle voxels (equation (4.1))

$$f\left(x \mid \mu,\sigma\right)=\frac{1}{\sigma\sqrt{2\pi}}e^{\frac{-(x-\mu)^2}{2\sigma^2}} \tag{4.1}$$

are measured to be $\mu=140$ and $\sigma=28$.

Because the ROI-RK method and RANSAC algorithm both process the voxels whose intensity is larger than a threshold value, the voxels with the intensities lower than the threshold are out of consideration and have no influence on the performance of the algorithms. Thus, in order to evaluate the quality of volumes after the intensity classification, a constant contrast ratio (CR) CR_{th}, is defined as:

$$CR_{th}=\frac{\overline{I}\left(M_{nd}^{th}\right)}{\overline{I}\left(M_{bg}^{th}\right)} \tag{4.2}$$

with, M_{nd}^{th} the needle voxels and M_{bg}^{th} the background voxels after the intensity classification respectively. $\overline{I}\left(\cdot\right)$ calculates the mean intensity of the chosen voxels.

Two main groups of simulated 3D US volumes have been generated. The first group is used to test the robustness of ROI-RK method compared with RANSAC only method with different insertion angles of the needle and a constant CR_{th} . α is changed from 0° - 90°, and β is changed from 60° - 120° corresponding to practical examination conditions [Bradley (2001)]. The simulation is done with one angle fixed and another changed. The detailed simulation parameters are given in Table 4-1. The simulation of randomly chosen α and β within the proposed range is also done to evaluate the performance of the ROI-RK method.

Table 4-1 The simulation parameters for evaluating the influence of the insertion angle with the constant contrast ratio (CR).

Parameter	**Value**
Needle length [mm]	$6-25$
Needle radius [mm]	0.6
α [degree]	$0^{\circ}, 30^{\circ}, 60^{\circ}, 90^{\circ}$
β [degree]	$60^{\circ}, 75^{\circ}, 90^{\circ}, 115^{\circ}$
CR	1.26

The second group is used to test the performance of ROI-RK method with different CR_{th} values. We aimed at evaluating the failure condition of ROI-RK method. All the other parameters, for example, the distance from the probe to the needle or the orientation of the needle, are fixed. The intensity of the digital image coded with 8 bits varies from 0 to 255. So, the simulation is performed to reach a CR between 0.90 and 1.33 (μ in (4.1) is from 70 to 150 stepped by 5). First, the threshold value is set as 99 % of the voxels are background voxels in one 3D US volume, then, the percentage of threshold is changed to get the different performances of ROI-RK method. Since the CR is calculated from the intensities, and these intensities are chosen in regular steps, the CR values are not separated by a constant step. In order to visualize the distributions of the voxel intensities, both in the needle and in the background, the different counts inside the ROI are given as histograms in Fig. 4-2. The simulation parameters are given in Table 4-2.

Table 4-2 The simulation parameters for evaluating the influence of the varied contrast ratio (CR) with the same inserting angles

Parameter	**Value**
Needle length [mm]	$10-25$
Needle radius [mm]	0.6
α [degree]	0°
β [degree]	73°

CR	0.90 – 1.33

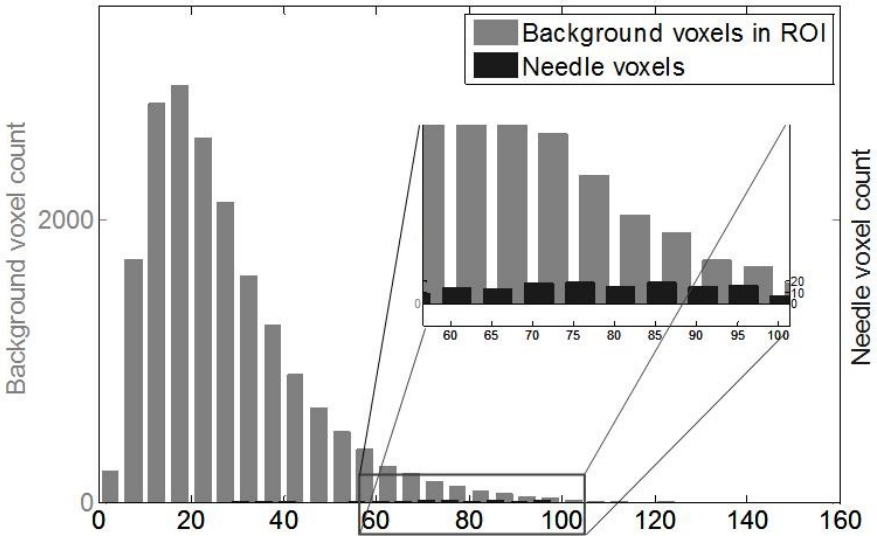

Fig. 4-2 An example of the count of the background voxels and the needle voxels on the same scale. The scale of the needle voxels can be seen in the enlarged view of the region in the square.

4.2 Results

The proposed ROI-RK method results were evaluated quantitatively and compared with the previously obtained results of the RANSAC algorithm used alone [Uherčík *et al.* (2010)]. Mean error (equation (4.3)) and standard deviation (STD) of error (equation (4.4)) were calculated. Each series was repeated 20 times.

$$\bar{\mathbf{e}}^{l} = E\left[\hat{\mathbf{x}}_i^{l} - \mathbf{x}_r^{l}\right] \tag{4.3}$$

$$STD^{l} = \left(\frac{1}{n-1}\sum_{i=1}^{n}(\hat{\mathbf{e}}_i^{l} - \bar{\mathbf{e}}^{l})^2\right)^{\frac{1}{2}} \tag{4.4}$$

here, the superscript l stands for the length of needle. $\hat{\mathbf{x}}_i^{l}$ is the estimated result of the i*th* repetition of the tracking chain, $\mathbf{x}_r^{l}$ is the ground truth value. $\hat{\mathbf{e}}_i$ is the measurement error of the i*th* repetition, and $\bar{\mathbf{e}}$ is the mean error of all the repeated tracking chains. n is the number of repetitions. The axis accuracy ε_{axis} and the tip error $\left|N_{tip}Q'\right|$ are illustrated in Fig. 3-4 (Section 3.3.2.1): N_{in} is the real insertion position, N_{tip} is the real tip, and $l(t;\mathbf{A})$ is the estimated axis. Q_1 and Q_2 are the orthogonal projections of N_{in} and N_{tip} on the estimated axis, respectively. $Q'(x',y',z')$ is the estimated tip position. The tip accuracy is defined as the error

between the x, y, z and x', y', z' separately. ε_{axis} is defined as the maximum of the Euclidean distance between the ground truth position of the insert point or tip point to their projection on the estimate axis, e.g. $\|N_{in}Q_1\|$, $\|N_{tip}Q_2\|$ in Fig. 3-4.

$$\varepsilon_{axis} = \max\left\{\|N_{in}Q_1\|, \|N_{tip}Q_2\|\right\} \tag{4.5}$$

4.2.1 Influence of insertion angle at fixed contrast ratio.

In this first series of simulations, the needle is inserted in the background at the fixed velocity of 1 mm/s along its axis. Between the beginning and the end of the sequence, the needle insertion varies from 6 mm to 25 mm. Four different values of angle α ($0^\circ, 30^\circ, 60^\circ, 90^\circ$) (Fig. 3-3 (b)) are simulated, whereas $\beta = 73^\circ$ in all the simulated volumes. The CR value is maintained constant and equal to 1.26 (μ in equation (4.1) is 140) for all the experiments presented in this section. The ROI is selected as a cylinder, whose axis is the axis of the needle, and whose radius is 5 times the radius of the needle. The length of ROI is limited using the estimated length of needle in the previous US volume. The results of the different metric errors for $\alpha = 30^\circ$ are represented in Fig. 4-3.

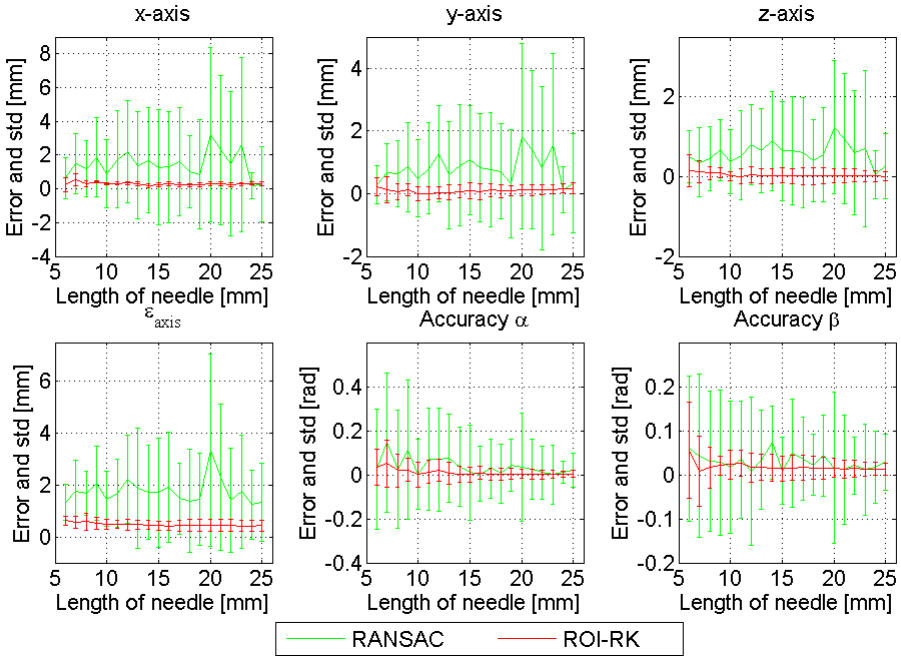

Fig. 4-3 The mean and the STD of the tip error (the first line), ε_{axis} (second line, left), α (second line, middle) and β (second line, right) for the RANSAC and ROI-RK detection methods with $\alpha = 30^\circ$, $\beta = 73^\circ$.

From Fig. 4-3, the mean error of the RANSAC only algorithm is always significant, while that of the proposed ROI-RK algorithm is very close to zero. This means that with the inhomogeneous background, the RANSAC cannot well estimate the position of the needle. The STD of the error of the ROI-RK is much smaller than that of the RANSAC algorithm, demonstrating that the ROI-RK method is more robust than the RANSAC algorithm to inhomogeneous background derived from breast scattering maps. Although sometimes the mean error of the RANSAC algorithm is equal or smaller than that of the ROI-RK method, this is only a fortuitous result, it cannot affect the average performance of the algorithm. Table 4-3 shows the STD improvement of error of the ROI-RK algorithm compared with the RANSAC algorithm with the different α. The improvement percentage is calculated as:

$$I_{per} = \left(1 - \frac{\overline{STD}_{ROI\_RK}}{\overline{STD}_{RANSAC}}\right) \times 100\% \qquad (4.6)$$

here, $\overline{STD}_{ROI\_RK}$ is the mean STD of error of the ROI-RK method; $\overline{STD}_{RANSAC}$ is the mean STD of error of the RANSAC algorithm. The high percentage improvement proves that the ROI-RK algorithm has largely increased the robustness of the needle position detection with the inhomogeneous background imitating the US response of breast tissues. What should be mentioned is that the change of insertion angle of the needle slightly influences the performance of the ROI-RK method. For the tip localization, if the coordinate is closer to the axis direction, the STD of error is smaller. From Table 4-3, when $\alpha = 90^\circ$, the improvement of the x-axis is only 54 %, and when $\alpha = 0^\circ$, the improvement of y-axis is 50 %. This is because the different spatial resolution of the lateral and azimuthal direction. In the tip localization step, the needle tip is considered as a point without size, meanwhile the size of the voxels cannot be ignored. This leads to a little shift when localizing the tip. When the coordinate is further to the axis direction, the STD of error is lager and it causes a smaller improvement rate.

Table 4-3 Improvement of the STD of the ROI-RK method compared with the RANSAC method ($\beta = 73^\circ$).

α	Improvement according to different α					
	x-axis	y-axis	z-axis	ε_{axis}	α	β
0°	95%	50%	84%	76%	80%	71%
30°	95%	87%	83%	88%	78%	72%
60°	90%	93%	91%	93%	76%	86%
90°	54%	95%	92%	90%	70%	88%

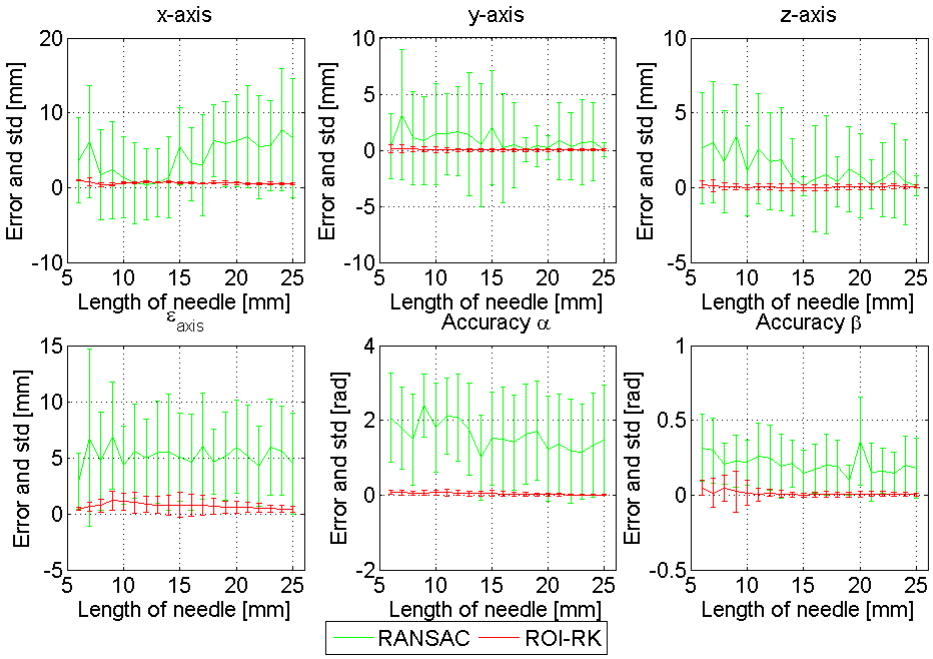

Fig. 4-4 The mean and the STD of the tip error (the first line), ε_{axis} (second line, left), α (second line, middle) and β (second line, right) for the RANSAC and ROI-RK detection methods with $\alpha = 0^\circ$, $\beta = 90^\circ$.

The second series of US volume are four different values of angle β ($60^\circ, 75^\circ, 90^\circ, 115^\circ$) are simulated, with fixed $\alpha = 0^\circ$, CR = 1.26. The needle is still in a dynamic situation with an insertion velocity 1mm / s along the inserting direction. The ROI is still a cylinder-like region with a constant radius 5 times the radius of the needle in the US image. The length of ROI is limited using the estimated length of needle in the previous US volume. The results of the different metric errors for $\beta = 90^\circ$ are represented in Fig. 4-4.

It can be seen from Fig. 4-4 that the mean and STD of error for RANSAC only method is significant, while the result of the proposed ROI-RK method is quite close to the ground truth value, even with a stable performance (extreme little STD). It is shown that the ROI-RK method is not influenced by the tilt angle of the inserting trajectory. Some of the mean errors of RANSAC algorithm are also small, even smaller than ROI-RK method (Fig. 4-4, length 12 of x-axis), however the corresponding error of y-axis and z-axis is large. It means that the tip position detected using RANSAC algorithm still has a large deviation from the ground truth value. Combined with the error chart of the angles α and β, it is obvious that the RANSAC algorithm failed to fit the best model of the needle axis. On the contrary, the ROI-RK method well located the needle axis and tip position. Table 4-6 gives the

percentage of improvement of the error's STD of the ROI-RK method compared to the RANSAC method. The average improvement of the tip position is higher than 95 %. The improvement of axis accuracy is more than 85 %. The improvement of angle α has an average at 95 %. Even with a changing β, the improvement ratio of β is at an average of 80 %. The significant improvement represents the excellence of the ROI-RK method. What's more, its stability satisfies for further on-line applications.

Table 4-4 Improvement of the STD of the ROI-RK method compared with the RANSAC method ($\alpha = 0^\circ$).

β	Improvement according to different β					
	x-axis	y-axis	z-axis	ε_{axis}	α	β
60°	97%	97%	97%	96%	94%	82%
75°	96%	97%	96%	97%	94%	80%
90°	97%	95%	93%	85%	96%	80%
115°	97%	98%	95%	95%	98%	78%

To further verify the proposed method, random pairs of α and β selected within the region given in Section 4.1 are used to generate the needle in different inserting directions. A summary of the needle tracking and locating results using ROI-RK method with four pairs of randomly chosen α and β are given in Table 4-5.

Table 4-5 A summary of mean located error and the STD of error using ROI-RK method.

α	β	The mean located error and its STD					
		x-axis [mm]	y-axis [mm]	z-axis [mm]	ε_{axis} [mm]	α [degree]	β [degree]
11°	118°	0.42 ± 0.43	0.15 ± 0.27	0.66 ± 0.31	0.99 ± 0.23	0.86 ± 2.58	0.48 ± 2.36
43°	101°	0.43 ± 0.60	0.57 ± 0.56	0.46 ± 0.57	1.30 ± 0.64	0.99 ± 4.16	1.83 ± 5.03
55°	97°	0.36 ± 0.55	0.62 ± 0.66	0.16 ± 0.80	1.05 ± 0.88	0.96 ± 3.72	0.46 ± 4.34
78°	67°	0.05 ± 0.26	0.64 ± 0.22	0.66 ± 0.18	1.05 ± 0.22	0.50 ± 2.58	0.92 ± 1.87

Table 4-5 summarizes the mean tracking error and its deviations of the six localization parameters of the different angle pairs of $[\alpha, \beta]$ equals to $[11^\circ, 118^\circ]$, $[43^\circ, 101^\circ]$, $[55^\circ, 97^\circ]$ and $[78^\circ, 67^\circ]$, respectively. With an inhomogeneous background and a randomly chosen insertion direction, there could be many outliers

which influence the tracking result. Thanks to the ROI-RK method, the mean error of the coordinates of x, y, and z coordinate of the tip position can be controlled within 1 mm. The mean error of the axis accuracy are all within 1.4 mm. Note that the axis accuracy ε_{axis} is defined as the maximum of the Euclidean distance between the ground truth position of the insert point or tip point to their projection on the estimated axis (Equation (4.5)). Since the needle appears as a thin cylinder in the 3D US volume, there could be a bias when estimating the needle position using an approximate model of line segment. An error of 3 mm for the axis accuracy is acceptable. Even though the axis accuracy reaches 1.4 mm or higher, the estimated axis is still within the range of the needle voxels of the 3D US volume. The shifts of angle α and β are less than 2°, which also illustrate that the estimated axis is within the main direction of the needle.

The ROI-RK method is also less time-consuming than RANSAC. Equation (3.36) gives the iteration number J of the RANSAC algorithm. This number is updated during processing according to the inlier ratio. The larger the inlier ratio, the smaller the iteration number, and the faster the needle position can be determined. To limit the processing time in the simulation, the maximum iteration number is set to 50. Since convergence is not attained when the RANSAC only algorithm reaches the number of 50 iterations, the position of the needle does not fit for a proper model. This leads to an inaccurate needle localization result and high STD error (Fig. 4-3, Fig. 4-4).

In order to get the same performance, RANSAC and ROI-RK were tested using the same series of 3D US volume but with different maximum iteration values. First, the iteration number J is estimated using Equation (3.36) in Section 3.3.1.2. For the RANSAC algorithm, there is not a precisely defined ROI, so the estimated maximum inlier ratio $\zeta_R = 0.05$. In the ROI-RK method, thanks to the precisely defined ROI, its estimated inlier ratio $\zeta_{ROI} \geq 0.4$. The parameter $\eta = 0.99$, thus J_R is about 1840 for RANSAC and J_P is about 26 for ROI-RK ($\zeta_{ROI} = 0.4$). This explains why convergence of RANSAC is not attained in our case, since the iteration number is set to 50 for both algorithms. In order to attain similar performances, the expected iteration number for RANSAC is set to 2000 while that of ROI-RK stays at 50.

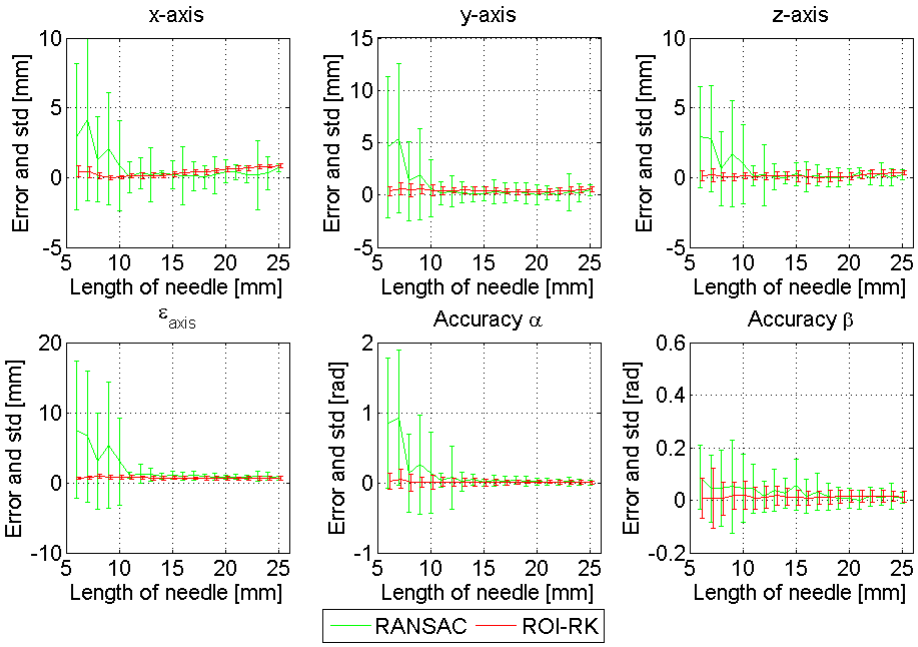

Fig. 4-5 The mean and the STD of the tip error (the first line), $\varepsilon_{\text{axis}}$ (second line, left), α (second line, middle) and β (second line, right) for the RANSAC and ROI-RK detection methods with $\alpha = 0^{\circ}$, $\beta = 75^{\circ}$.

Fig. 4-5 shows the approximate same performance using the RANSAC and ROI-RK method. When the needle length shorter than 10 mm, no matter how large the iteration number is set, the RANSAC algorithm confusing the needle position with the line-like structures from the inhomogeneous background. It cannot achieve the same performance as ROI-RK method. When the needle length is longer than 10 mm, the almost same performance is achieved using the two localization method. In this situation, the average time for needle localization in a single volume is $t_{RANSAC} = 2.6$ s for RANSAC algorithm and $t_{ROI-RK} = 0.1$ s for ROI-RK algorithm. Note that at present, the ROI-RK method is implemented using MATLAB. The calculation time is expected to further reduce by implementing it in a C++ environment. Since the ROI-RK method is less time-consuming, and since for the mechanical US scanner, it takes about 1 s to generate a 3D US volume, the proposed method satisfies the real-time condition necessary for clinical applications. Even using a 2D array probe with a volume rate at 10 volumes / s, the ROI-RK method is adapted to real time processing.

4.2.2 Influence of the contrast ratio (CR)

In this section, first, the success rate of the ROI-RK method is calculated depending on different CR values. Then, in the low CR condition, the situation of failure of ROI-RK method has been analyzed.

For evaluating the method, if a Euclidian distance larger than 3 mm exists between the estimated tip and the real tip position, or between the estimated axis and the real axis, the method is considered to fail. The useful simulation parameters are shown in Table 4-2. For the CR changing situation, the two angles are fixed at $\alpha = 0^\circ$, $\beta = 73^\circ$. What should be also mentioned is that the range of CR (0.90 – 1.33) is set according to the real 3D US volumes.

The needle is still in a dynamic situation with an inserting velocity along the axis direction of 1 mm/s. The ROI is selected as a cylinder, whose axis is the estimated axis of the needle, and whose radius is 5 times the radius of the needle. The length of ROI is limited using the estimated length of needle in the previous US volume. In order to count the success rate, the trail repeated 50 times.

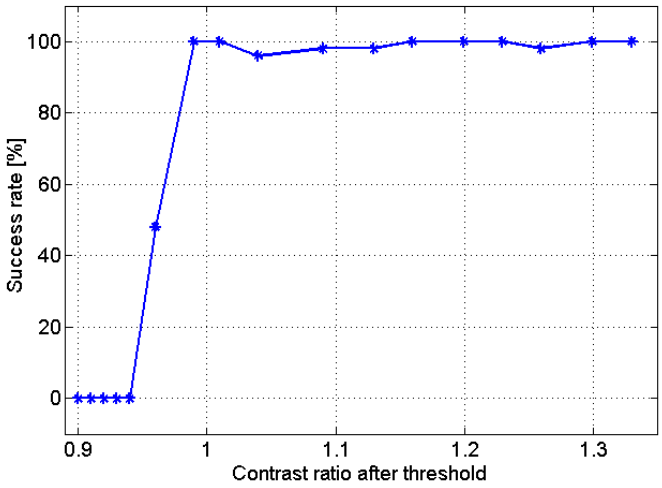

Fig. 4-6 The success rate for ROI-RK method with different CR value. Here, the threshold value is calculated as 99 % of the voxels are background.

Fig. 4-6 is the curve of the success rate of the ROI-RK method with CR_{th} from 0.90 to 1.33. The step of CR_{th} is not uniform because it is a ratio of the intensities of the needle voxels and background voxels. From Fig. 4-6, it is obvious that when the CR is equal or larger than 1, the ROI-RK method has a success rate round 100 %. However, for the CR value from 0.9 to 1.0, the success rates are not satisfying. In order to analyze the reason that leads to the failure of the ROI-RK method, it is tested by changing the percentage of the threshold value, and the results of successful rate are given in Table 4-6.

Table 4-6 The success rate of ROI-RK method depending on different CR and threshold

Success rate [%]	CR_{th}						
Threshold [%]	0.90	0.91	0.92	0.93	0.94	0.96	0.99
95	14	98	98	92	98	100	96
96	8	44	96	94	100	98	100
97	0	28	92	92	98	98	98
98	0	0	2	12	98	98	100
99	0	0	0	0	0	48	100

Table 4-6 presents the success rate of the ROI-RK method for the different CRs. The CR is calculated using the assumption that 99 % of the voxels in a 3D volume is the background voxels. In low CR situation, the percentage of background voxel is reduced to obtain a higher success rate for ROI-RK method. From each column in Table 4-6, one can observe that when the CR is fixed, the higher the percentage for calculating the threshold value, the lower the success rate is. Fig. 4-7 shows the histogram of the distributions of the background voxels in the ROI and needle voxels. The percentage of threshold changes from 95 % to 99 % while the CR is kept equal to 0.93. From Fig. 4-7, it is clear that with the growth of the threshold, although more and more background voxels are eliminated by thresholding, some needle voxels are also excluded. Table 4-7 gives the average inliers count with the same CR = 0.93; the threshold percentages change from 95 % to 99 %. The inliers count is an average value because the needle length is different. Fig. 4-8(a–e) shows the different appearances of the needle after the different thresholds in the 3D US volume when the CR = 0.93, corresponding to Fig. 4-7(a–e). A large threshold value can limit the influence of the speckle noise of the background; moreover, it also deletes the needle voxels whose intensity is less than this threshold. Obviously, the incomplete structure of the needle leads to the failure of the ROI-RK method. Thus the success rates decrease. From each line in Table 4-6 it is apparent that when the threshold percentage is fixed, the higher the CR is, the more robust the ROI-RK method is. Fig. 4-9 shows the histogram of six different CRs (from 0.90 to 0.96) of the background voxels and the needle voxels with the threshold percentage equal to 97 %. With the increase in the CR, more and more needle voxels pass the threshold and make the structure of the needle more distinct (Fig. 4-10). With the complete structure of the needle, even though the speckle noise still exists, the ROI-RK method does not fail. From Fig. 4-7 – Fig. 4-10, one can conclude that if the structure of the needle is relatively complete, regardless of whether the background is noisy or not, the ROI-RK method can detect and track the needle position well.

Table 4-7 The average inliers count with different thresholds percentages change from 95 % to 99 %, with CR_{th} = 0.93.

CR_{th}	0.93				
Threshold percentage [%]	95	96	97	98	99
Inliers count	232	220	199	168	97

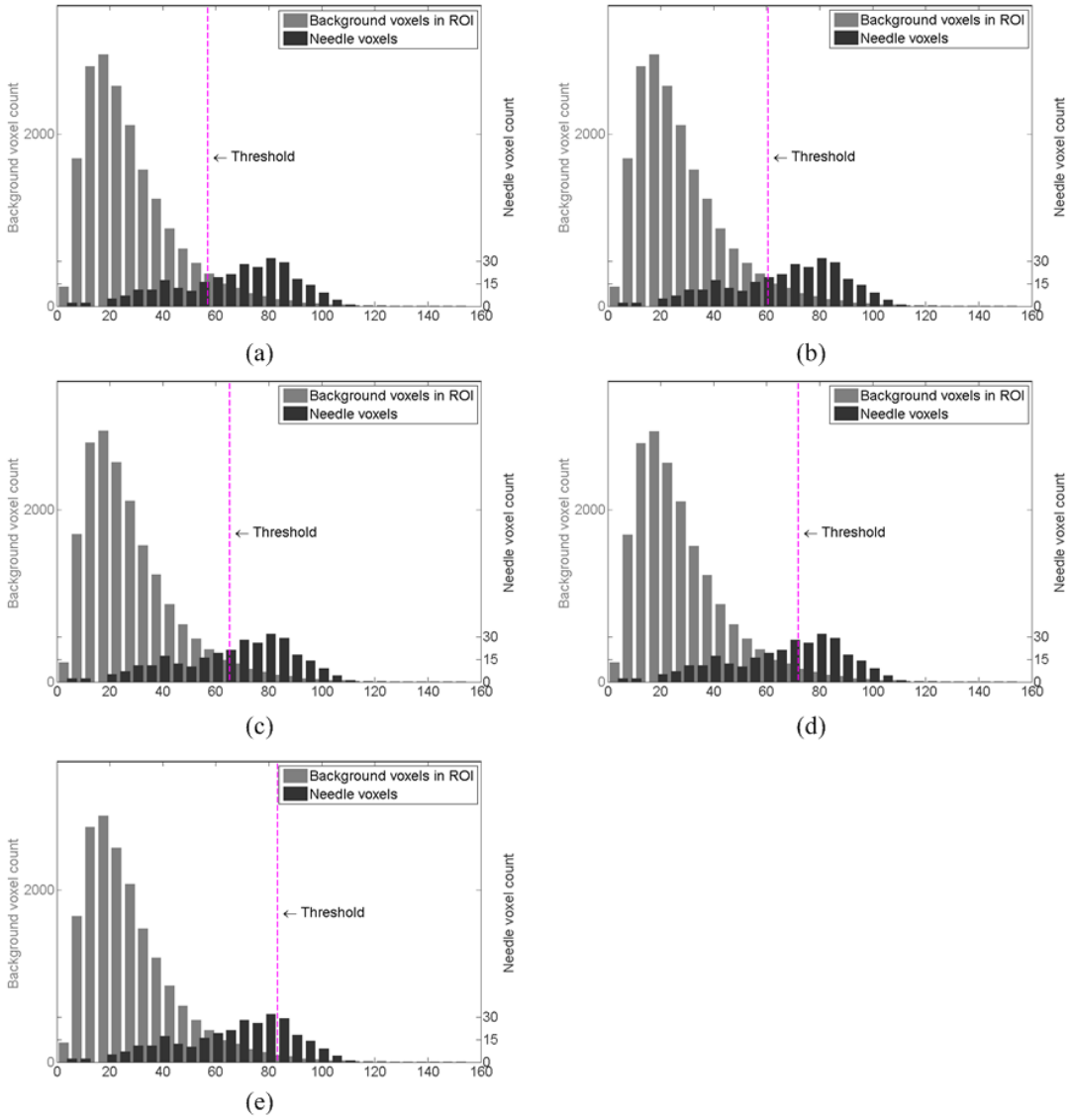

Fig. 4-7 The histogram of background voxels in the ROI and needle voxels. The vertical dashed line represents the threshold value. The threshold value changes with CR_{th} = 0.93. Note that in order to be able to observe well the different counts of the background voxels and the needle voxels, the scales of the left and right y-axis are not the same.

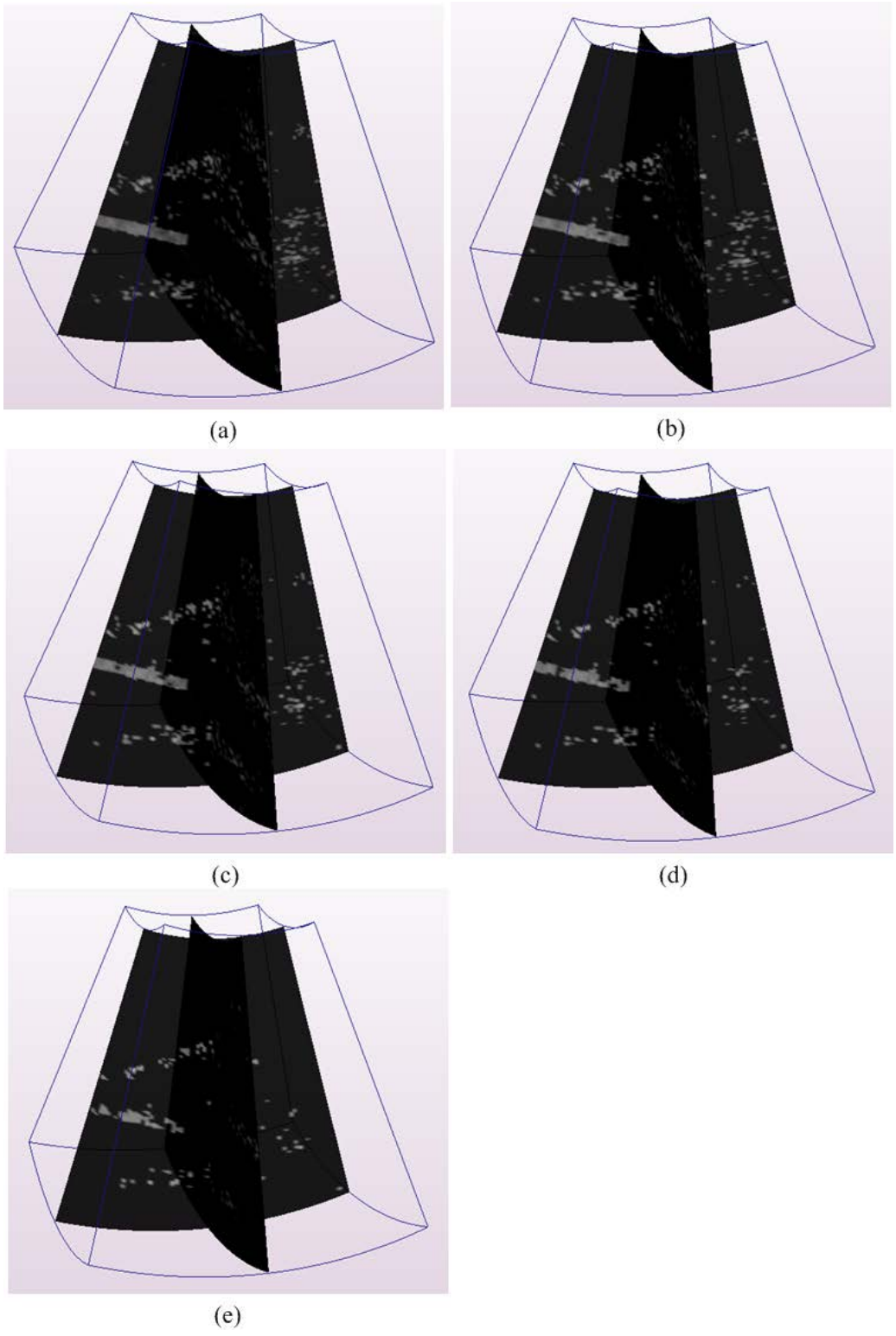

Fig. 4-8 Different appearances of a needle in the 3D US volumes after the different threshold percentage, CR_{th} = 0.93: (a) 95 %; (b) 96 %; (c) 97 %; (d) 98 %; (e) 99 %.

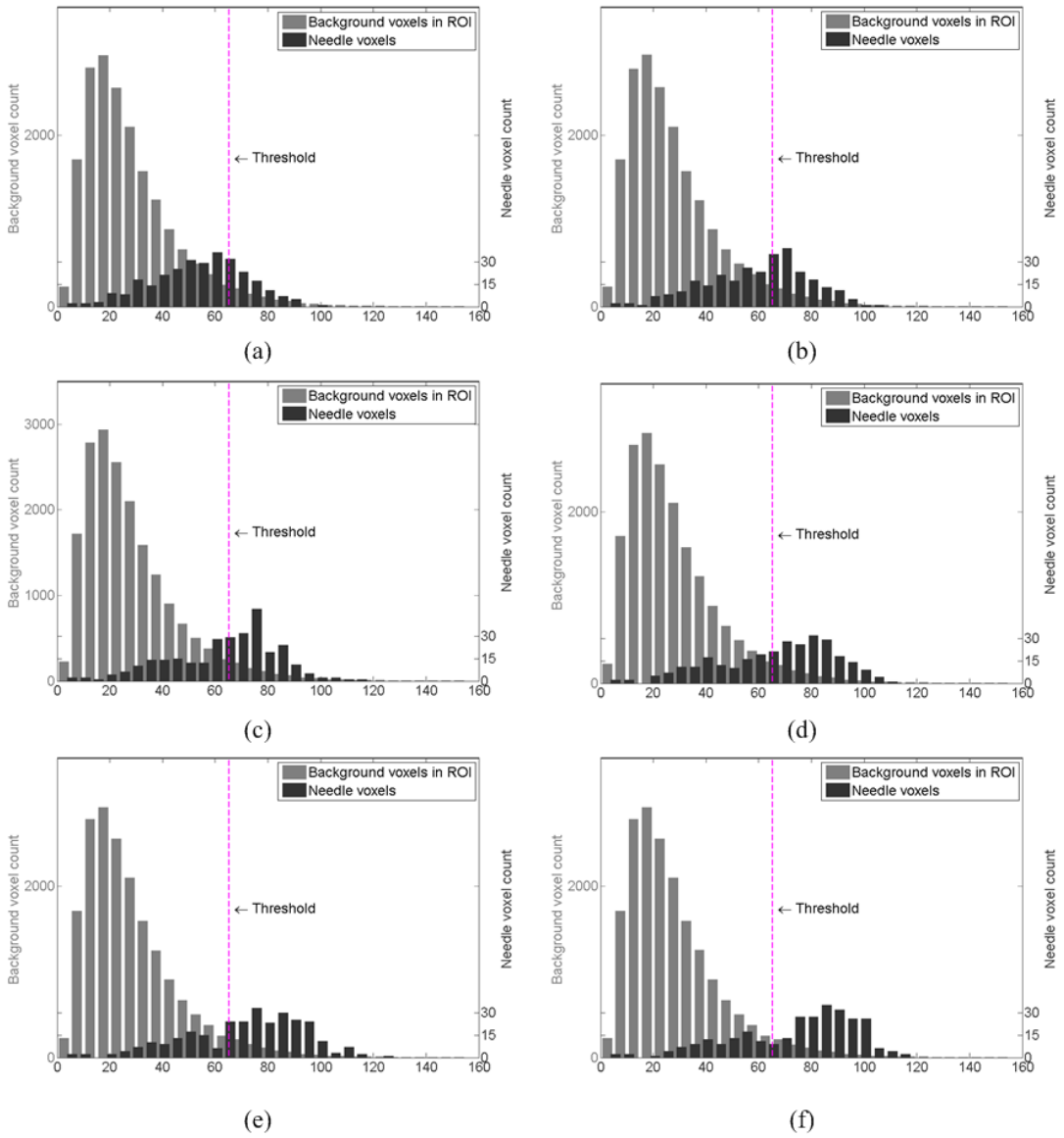

Fig. 4-9 The histogram of background voxels in the ROI and needle voxels. The vertical dashed line represents the threshold value. The CR is from 0.90 to 0.96, with the threshold percentage equal to 97 %. Note that in order to be able to observe well the different counts of the background voxels and the needle voxels, the scales of the left and right y-axis are not the same.

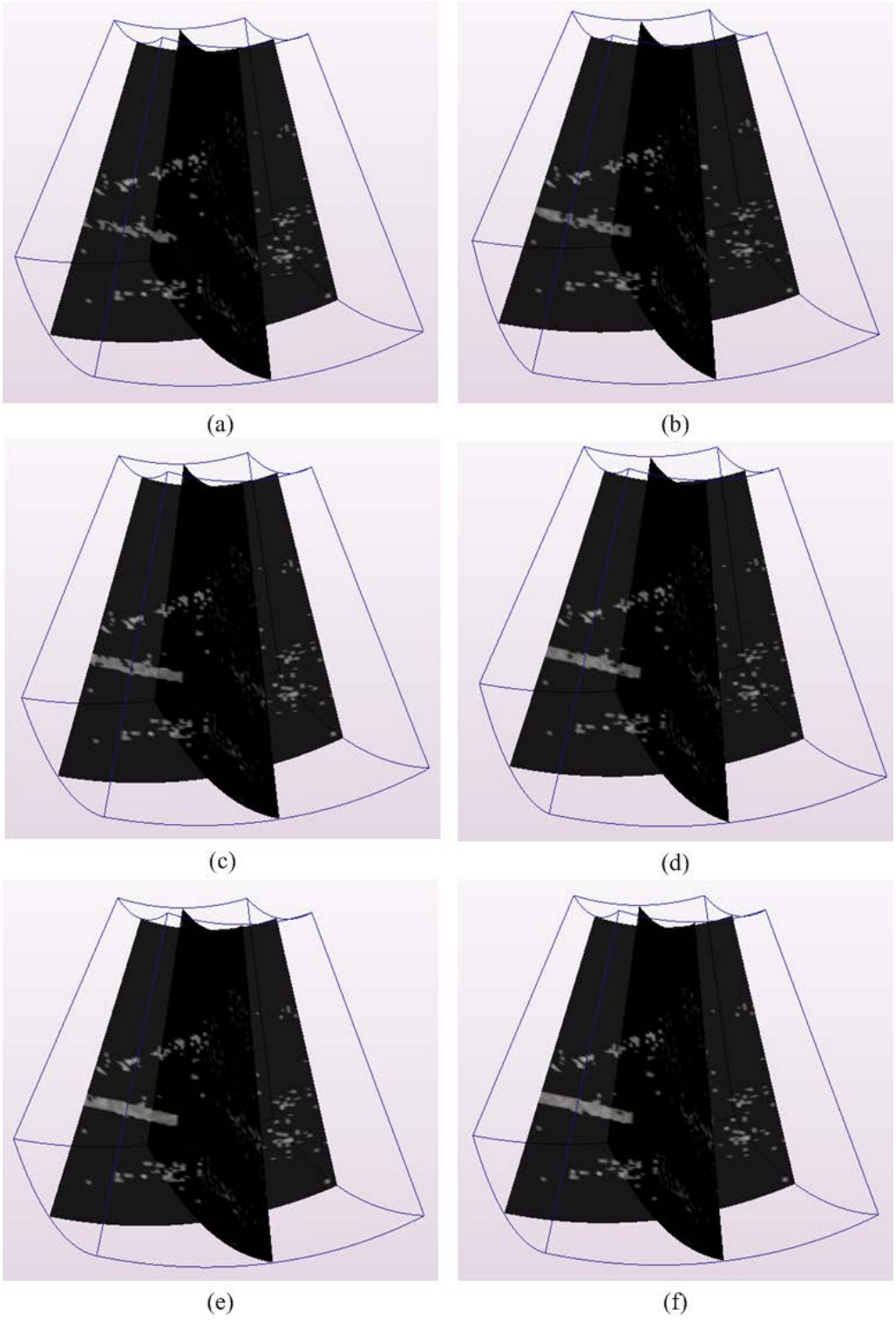

Fig. 4-10 Different appearances of a needle in the 3D US volumes after the same threshold, with different CRs : (a) 0.90; (b) 0.91; (c) 0.92 (d) 0.93; (e) 0.94; (f) 0.96.

4.3 Discussion

The objective of this thesis is to develop a robust needle localizing and tracking method for the further clinical application, especially on liver biopsy guidance using 3D US. The current work consists in a simulation validation of the robustness of the proposed technique. The study will next be extended to *ex-vivo* and *in-vivo* tests. Moreover, in real 3D US volume, some more challenges like electronic noise, the difficulty to separate the needle tip and the physiological motion can appear.

Electronic noise is usually considered as additive white Gaussian noise in ultrasonic imaging. With the increase of the depth, the influence of electronic noise grows gradually because of the attenuation of the US signal. The main effect of this kind of noise in the ROI-RK method will be in the speckle tracking step. Since the NCC is calculated, the electronic noise will lead to a miss match between the kernel region and the right target in the searching region. A step of noise compression could be added to limit the effect of the electronic noise.

The second challenge is the precise tracking of the needle tip. Because of its small size the needle tip reflects less US wave, which can cause a shadow at the tip compared with the whole image of the needle; on the other hand, because some tissue could shelter the US wave, certain parts of the needle could appear as dark as the surrounding tissue in the US image. In this situation, the tip could be considered as a hot pixel and ignored by the radiologist. What's more, if the tip of the needle is not well located, the risk of injury for the human tissue or organ increases. As a result, precise tracking of the needle tip is very important in clinical applications.

The two challenges mentioned above are less problematic in *ex-vivo* experiments. However, in the clinical applications, the physiological motion of the liver cannot be negligible. The motion of the liver tissue is mainly caused by respiration. In [Bell *et al.* (2012)], it is claimed that the mean peak-to-trough displacements of liver motion span is 5 – 40 mm in the superior – inferior direction under normal respiratory conditions. Since our work has not yet reached the *in-vivo* applicability, our model does not include the information of tissue motion. A tissue motion model could be implemented in the control vector and control matrix (Section 3.3.1.1, equation (3.28)) of the Kalman filter in order to make the ROI-RK method closer to the real applications.

4.4 Conclusion

In this chapter, different simulations have been done to verify the robustness of the ROI-RK method. The simulation results show that even with an inhomogeneous background, the ROI-RK method can locate the biopsy needle precisely and rapidly.

In the discussion part, the further development of this method and the challenges in *ex-vivo* and *in-vivo* application are presented.

Chapter 5

Other contribution: RANSAC with ML algorithm

Contents

5.1 Introduction

Machine learning (ML) plays an essential role in the field of medical imaging, including computer-aided diagnosis, image segmentation, image registration, etc. The task of ML is to determine optimal hyper planes for separating classes in the multidimensional feature space which is formed by the input features [Suzuki (2012)]. One speaks also about classification. The classification algorithms for ML algorithm include linear discriminant analysis [Duda *et al.* (2001)], support vector machine (SVM) [Burges (1998)], adaptive boost (AdaBoost) [Freund *et al.* (1997)], etc. In the medical image processing domain, using characteristics (also called features) calculated from the images instead of using directly the voxels intensities only to categorize them can improve the quality of image classification. In particular, feature based classification on medical images can help in several diagnostics, as for example, separate the cancer cells from the healthy ones. Other applications include searching

for images from a large image database, or limiting the number of query results [Tommasi *et al.* (2010)].

In the task of localization micro tools using 3D US systems, because the soft tissue has a complex structure, some parts of the tissue could have the same intensity level as the metal needle. In this situation, using only the threshold value to classify the needle and background tissue is not enough. We propose to extract some shape features of the needle to help with the needle position localization in our application. The Hessian based line filter, which is used to calculate the tubularness volume in ROI-RK method (Section 3.2), has been implemented here to calculate the tubular feature of the voxels. Several machine learning algorithms have been implemented in the RANSAC algorithm [Uherčík *et al.* (2010)] for a more accurate classification of voxels. However, in the previous work, only one group of data set has been trained and tested to evaluate the performance for ML algorithm. This is not enough to prove the advantage of the different classifiers. Thus a cross validation should be done to evaluate the average performance on different data sets. In this chapter, first the new model for RANSAC algorithm using the ML algorithm is presented. Then the selected classifiers are introduced. In the results part, we first evaluate the average performance of the RANSAC with ML algorithm using eighteen simulated data sets. Then the results for needle localization in different data sets are presented. After that follows the discussion and conclusion.

Note that this part of the work has been conducted in parallel with the development of the ROI-RK method. Unlike ROI-RK method, which uses a fixed SegShp model in RANSAC algorithm for needle localization, the RANSAC with ML algorithm concentrates more on a statistic model learnt from the features, there is not a fixed tool model. It aims at improving the success rate of the RANSAC algorithm with the models learnt from the existing 3D US volumes, and it is evaluated in a static situation. The modifications of some steps of the RANSAC algorithm are described hereunder. This piece of work has been published in CBM, 2013.

5.2 RANSAC with ML algorithm

The main improvement over the previous RANSAC algorithm is that the shape information and the classifiers trained on labeled training data have been added in the first two steps of the RANSAC algorithm, which significantly improves localization robustness. The RANSAC with ML algorithm contains four steps: (a) voxel classification; (b) axis estimation; (c) local optimization; and (d) tip localization. The main improvement concentrate on the step (a) and (b), the other two steps are the same as Section 3.3.2.2. So in this part, we only present the features extracted from the original US volume and the classification models implemented in step (a) and (b).

Voxel classification — in this step, a set of possible needle voxels V_{nd} is chosen. Not only the intensity of the voxels $I(M)$ is used, but also a tubularness measurement $J(M)$ calculated from Frangi's line filter enhancement (Section 3.2.1) is implemented. So the feature vector in this step is:

$$\mathbf{m}_1(M) = \left[I(M), J(M) \right] \tag{5.1}$$

here, M is a voxel of the original 3D volume. Using this feature vector and the different pre-trained classifiers, V_{nd} is classified from the whole US volume.

Axis estimation — in this step, an approximate position of the needle axis is located using the set of needle voxels from the first step. Two voxels are randomly selected from V_{nd} and a curve coefficient matrix $\mathbf{A}$ can be generated using equation (3.16) and (3.17), thus a line $l(t;\mathbf{A})$ is fixed. With $l(t;\mathbf{A})$, a new feature vector $\mathbf{m}_2(M)$ can be obtained:

$$\mathbf{m}_2(M) = \left[I(M), J(M), d(M;\mathbf{A}), \delta(M;\mathbf{A}) \right] \tag{5.2}$$

Here, $d(M;\mathbf{A})$ and $\delta(M;\mathbf{A})$ are the new features calculated using the curve coefficient matrix $\mathbf{A}$. $d(M;\mathbf{A})$ is the Euclidean distance from the voxel M to the line $l(t;\mathbf{A})$. $\delta(M;\mathbf{A})$ is generated as below.

Suppose the unit directional vector for line $l(t;\mathbf{A})$ is noted as $\mathbf{e}_1$. A plane perpendicular to the line $l(t;\mathbf{A})$ is easy to locate. From this plane, two mutually perpendicular unit vectors $\mathbf{e}_2$ and $\mathbf{e}_3$ are obtained. Thus the 3D oriented line filter along the direction $\mathbf{e}_1$ is defined as:

$$\delta(M, \mathbf{e}_1) = \frac{\partial^2 f_V(M)}{\partial \mathbf{e}_2^2} + \frac{\partial^2 f_V(M)}{\partial \mathbf{e}_3^2} \tag{5.3}$$

here, f_V is the image function. The filter $\delta(M, \mathbf{e}_1)$ is designed to give a high response for the linear structure with the particular orientation $\mathbf{e}_1$. Note that the second-order directional derivatives are easy to obtain from the Hessian matrix at a low computational cost [Uherčík *et al.* (2013)]:

$$\frac{\partial^2 f_V(M)}{\partial \mathbf{v}^2} = \mathbf{v}^T \mathbf{H}(M) \mathbf{v}, \ \ \mathbf{v} \in \Re^3, \|\mathbf{v}\| = 1 \tag{5.4}$$

here, $\mathbf{v}$ is a unit vector of the given direction. $\mathbf{H}(M)$ is the Hessian matrix of the voxel M. Thanks to the calculation of the tubularness measurement $J(M)$ for each

voxel M, the Hessian matrix $\mathbf{H}(M)$ is also calculated (equation (3.2)). This helps to calculate the oriented line filter $\delta(M, \mathbf{e}_1)$ more efficiently.

A classification function $q_{lf}(M;\mathbf{A})$ can be obtained using the ML algorithms and the feature vector $\mathbf{m}_2(M)$. Working as an indicator, $q_{lf}(M;\mathbf{A})$ helps to classify the inliers from V_{nd} and to selected a more precise set for needle voxels. Then this set is used in the local optimization step to get a better fitting line representing the needle. In the tip estimation step, the intensity of voxels along the best fitting line is calculated and the position with a sharp drop of the intensity value is considered as the tip position.

5.3 Introduction of the classifiers

Linear classifier: the decision function for the monolithic linear classifier is [Duda *et al.* (2001)]:

$$f_{linear}(M) = 1 \Leftrightarrow \mathbf{w}_{linear} \cdot \mathbf{m}(M) \geq \omega_{linear} \tag{5.5}$$

here, $\mathbf{w}_{linear}$ is a weight vector and ω_{linear} is a bias. The parameters $\mathbf{w}_{linear}$ and ω_{linear} are learned from the training data with ground truth value using Fisher's linear discriminant (FLD). Note that $\mathbf{m}(M)$ stands for the feature vectors, it could be $\mathbf{m}_1(M)$ and $\mathbf{m}_2(M)$. Naturally the $\mathbf{w}_{linear}$ and ω_{linear} will change according to the chosen feature vector. For the following classifiers, the same notation is used for the reason of concision. A pocket training algorithm [Gallant (1990)] is also implemented to keep the best solution found so far.

SVM: the decision function for SVM classifier is defined as:

$$f_{SVM}(M) = 1 \Leftrightarrow \mathbf{w}_{SVM} \cdot \mathbf{k}_{SVM}(M) \geq \omega_{SVM} \tag{5.6}$$

$\mathbf{w}_{SVM}$ and ω_{SVM} are the pre-learned parameters for SVM classifier. $\mathbf{k}_{SVM}(M)$ is the vector of kernel functions:

$$\mathbf{k}_{SVM}(M) = \left[k(\mathbf{m}(M), \mathbf{s}_1), k(\mathbf{m}(M), \mathbf{s}_2), ..., k(\mathbf{m}(M), \mathbf{s}_d)\right]^T \tag{5.7}$$

here, $\mathbf{s}_1, ..., \mathbf{s}_d$ are support vectors, and they are a subset of the training data. $k(\cdot)$ is the kernel function. Since the kernel function with linear mapping is selected, $k_i(\mathbf{m}(M), \mathbf{s}_i) = \mathbf{m}(M) \cdot \mathbf{s}_i$. The SVM classifier is trained using a fast-cutting plane algorithm (LIBOCAS library) [Franc *et al.* (2009)] under the Linux system. Under the

Windows system, the SVM Light library [Joachims (1999)] can be implemented but it is much slower.

AdaBoost: this classifier is actually a learning meta-algorithm [Freund *et al.* (1997)]. Given a labeled training set and a set of weak classifiers, the AdaBoost produces a strong classifier. Its decision function is:

$$f_{\text{Ada}} = \sum_{i=1}^{n} f_{weak}^{i}\left(\mathbf{m}(M)\right) \tag{5.8}$$

here, $f_{weak}^{i}(\cdot)$ stands for one of the decision function from the set of weak classifiers. In our application, the AdaBoost classifier is trained with decision stumps [Svoboda *et al.* (2007)] and ten weak classifiers.

WaldBoost: WaldBoost is proposed by J. Šochman and J. Matas [Sochman *et al.* (2005)]. It is an algorithm which integrates the AdaBoost-based measurement selection and Wald's sequential probability ratio test (SPRT). The SPRT provides the termination criterion for the evaluation in the cascade. In our application, the Waldboost classifier is trained with domain partitioning weak classifiers [Schapire *et al.* (1999)] with eight bins. The desired TP rate and FN rate (Table 5-1) were set to 99% and 1%, respectively.

Cascade classifier: the cascade classifier contains two steps. First, all the voxels of the US volume are classified by a threshold value, which is chosen as 95 % of the training data. All voxels with intensities below the threshold are considered as the background voxels. The second step is a linear classifier using the feature vector $\mathbf{m}_1(M)$ only functions on the thresholded voxels. The advantage of the cascade classifier is that the computational cost of ML algorithm is limited since ML is performed on a small fraction of voxels, so the classifier is very fast.

5.4 Evaluation of the combination of the classifiers

5.4.1 Segmentation evaluation

The ability of classifiers described from Section 5.3 to distinguish between needle and background voxels on the simulated data is evaluated in this section.

The working points of the classifiers were adjusted so that their specificity was 80% on the test data:

$$\text{Specificity} = \frac{\text{TN}}{\text{TN+FP}} \tag{5.9}$$

here, the symbols are defined in Table 5-1. The main performance criterion is precision (also called inlier ratio or positive predictive value, a voxel is considered to be an inlier if it is closer to the tool axis than the tool radius) because it directly influences RANSAC performance. The precision is defined as:

$$\text{Precision}=\frac{TP}{TP+FP} \tag{5.10}$$

The sensitivity (TP rate) is also evaluated and defined as:

$$\text{Sensitivity}=\frac{TP}{FN+TP} \tag{5.11}$$

Table 5-1 Confusion matrix illustrates naming conventions for the evaluation of classification results.

	Negative predicted	Positive predicted
Actual negative	true negative (TN)	false positive (FP)
Actual positive	false negative (FN)	true positive (TP)

Table 5-2 Parameters used in FIELD II simulations.

Parameter name	Value
Transducer center frequency [MHz]	7.5
Sampling frequency [MHz]	27
Speed of sound [m/s]	1540
Elements of the probe	128
Width of element [mm]	0.1
Height of element [mm]	10
Kerf [mm]	0.017
Focal depth [mm]	50
Range of scan lines [degree]	[-20, 20]
Range of scan planes [degree]	[-20, 20]

Table 5-3 Classifier performance in distinguishing the needle voxels and background voxels in the voxel classification step. Specificity was set at 80%.

Type of classifier	Mean precision	Mean sensitivity	Specificity
Thresholding	6.0% ± 2.0%	32.7% ± 9.1%	80%
Linear (FLD.)	87.5% ± 1.7%	78.8% ± 3.0%	80%
SVM	88.5% ± 1.7%	82.1% ± 3.2%	80%
AdaBoost	89.0% ± 2.5%	90.0% ± 3.9%	80%
WaldBoost	88.5% ± 1.3%	83.2% ± 2.6%	80%
Cascade	97.8% ± 0.9%	46.9% ± 8.1%	80%

Table 5-4 Time spent on voxel classification for different data sets using the linear classifier performance on all voxels (full) and only for voxels selected by the first step of the cascade classifier (cascade).

Data type	Size [voxel]	Calculation time [s]	
		Full	Cascade
Simulation	53×71×164	10.6	1.0
PVA	53×71×310	18.8	2.1
Breast biopsy	383×273×208	236.7	30.3

The cross validation is done to obtain an average evaluation of the performance of the classifiers. To do the cross validation, eighteen simulated data sets were generated using FIELD II [Jensen *et al.* (1992); Jensen (1996)]. Table 5-2 gives the parameters used in FIELD II. The needle orientation angle β is from 40° to 110° with respect to the probe, with 4° steps. Fifty simulation runs are done on the different pairs of training and testing data sets. For each pair of data sets, twelve out of eighteen are used for training for the parameters of the different classifiers, and the remaining six for testing. For each run, the training and testing data sets are randomly chosen from the eighteen data sets, with no repetition.

Table 5-3 shows the performances of the different classifiers in the voxel classification step. The mean precision and sensitivity and their standard deviations are given for 80% specificity. A high precision indicates that the classifier can well distinguish the needle voxels, and it barely confuses the background voxels as the needle voxels. A high sensitivity means that the classifier rarely considers the needle voxels as the background voxels. From Table 5-3, it can be found that the AdaBoost classifier gives the best results in terms of sensitivity at 90.0 % with the standard deviation 3.9 %. The Cascade classifier has much lower sensitivity, which means that it consider some needle voxels as the background, but it has excellent precision at 97.8 %, which is important for the subsequent axis estimation step, and the speed gain is substantial (Table 5-4). All classifiers using the feature vector which contains at the same time the intensity $I(\cdot)$ and tubulaness measurement $J(\cdot)$ perform significantly better than the classifier that only uses the intensity values of the voxels (denoted 'Thresholding' in Table 5-3).

5.4.2 Inlier detection

The inlier detection performances of the classifiers for the axis estimation step of RANSAC with ML algorithm (Section 5.2) were also trained and tested using cross-validation (Section 5.4.1) on synthetic data taking advantage of the availability of ground truth. The position of the needle was chosen randomly with the needle orientation angle β with respect to the probe axis between 40° and 110° (Fig. 5-2). The results for 98% specificity are reported in Table 5-5. For the SVM classifier, the mean precision and mean sensitivity are at 99 %. This result means that using the feature vector $\mathbf{m}_2(M)$ (equation (5.2), section 5.2), the SVM classifier well separates the needle voxels from the background voxels. The second best performing classifier is WaldBoost, with 97 % precision and 91 % sensitivity.

The differences between the sensitivity and precision of the linear, SVM, AdaBoost, WaldBoost and Cascade classifiers are tested using the Welch's t-test [BL Welch (1947)]. The results show that the classifiers are statistically independent.

Table 5-5 The performance of the inlier classifier on simulated data.

Type of classifier	Precision	Sensitivity	Specificity
Linear (FLD)	94.5% ± 4.4%	86.4%± 4.7%	98%
SVM	99.1% ± 1.9%	99.7%± 1.1%	98%
AdaBoost	84.5% ± 5.6%	42.8%± 4.7%	98%
WaldBoost	97.4% ± 3.1%	91.6%± 8.9%	98%

5.5 Evaluation of the tool localization method using line filter

5.5.1 Data set used to evaluate the method

The RANSAC with ML algorithms was implemented in MATLAB (the MathWorks, Natick, MA, USA) and tested on a PC with an Intel Core i7 processor at 2.83 GHz. The results of the experiments compare the various combinations of classifiers and different needle localization methods on the following data sets.

Simulation: fifty-six 3D US data sets with high or low CR were generated using an inhomogeneous background simulated with FIELD II. An image of a needle was created by adding a 0.5-mm-radius and 10-mm-length cylinder. The intensity of the needle voxel follows a distribution evaluated on experimental data (Chapter 4, Fig. 4-1). The angle β is within the range of $\left[60^{\circ},110^{\circ}\right]$, and the distance from the needle to the probe is within the range of $\left[65\text{mm},75\text{mm}\right]$ Thanks to the simulated domain, the ground-truth position of the needle is known. Fig. 5-1 shows two 3D demonstrations of the simulated volume with high and low CR. The volumes are set to mimic the real ultrasound scanner as closely as possible.

For each 3D volume, there were 55 azimuthal planes covering an angle of 34° and 64 beams covering a lateral angle of 38°; in the axial direction, each pixel corresponds to approximately 0.3mm.

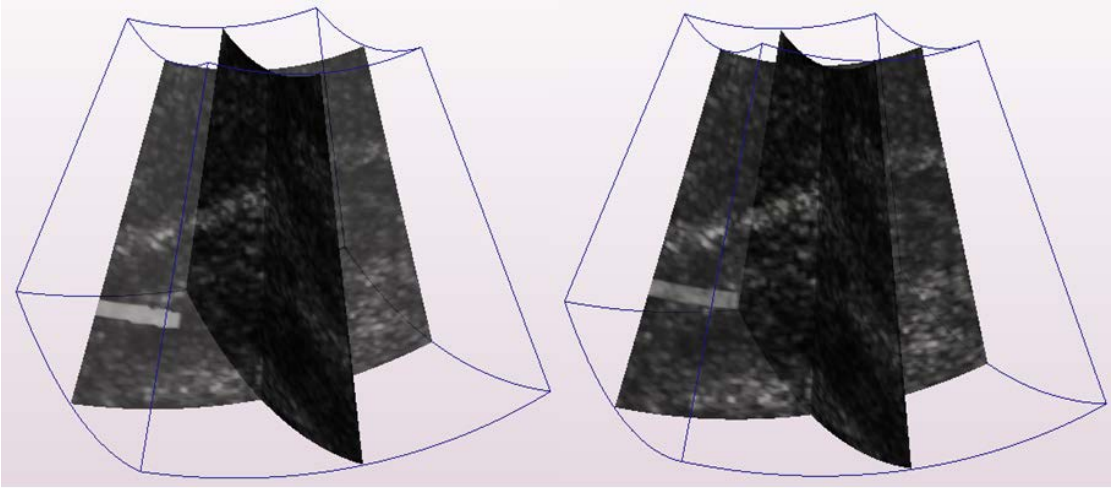

Fig. 5-1 Illustrations of simulated volumes: (a) a volume with high contrast ratio; (b) a volume with low contrast ratio.

PVA phantom: experiments were conducted on a PVA cryogel phantom that mimics biological tissue properties [Duboeuf *et al.* (2009)].

The PVA cryogel phantom contained a 0.3-mm-diameter electrode. It is important to note that although the real diameter of the electrode is 0.3mm, the apparent diameter in the US volume will be almost the same as the simulated one because ultrasound images convolve with the point spread function (PSF) [Mari *et al.* (2011)]. (Figure 2a). Eight 3D US images, 53×71×260 voxels, of the PVA cryogel phantom with different insognification angles were acquired using the Voluson 530D ultrasound scanner with 7.5-MHz probe. These volumes have different angle spans of observed volume, listed in pairs $[\alpha, \beta]$ as $[90^\circ, 20^\circ]$, $[80^\circ, 25^\circ]$, $[60^\circ, 15^\circ]$, and $[10^\circ, 25^\circ]$. The definition of α and β is shown in Fig. 5-2.

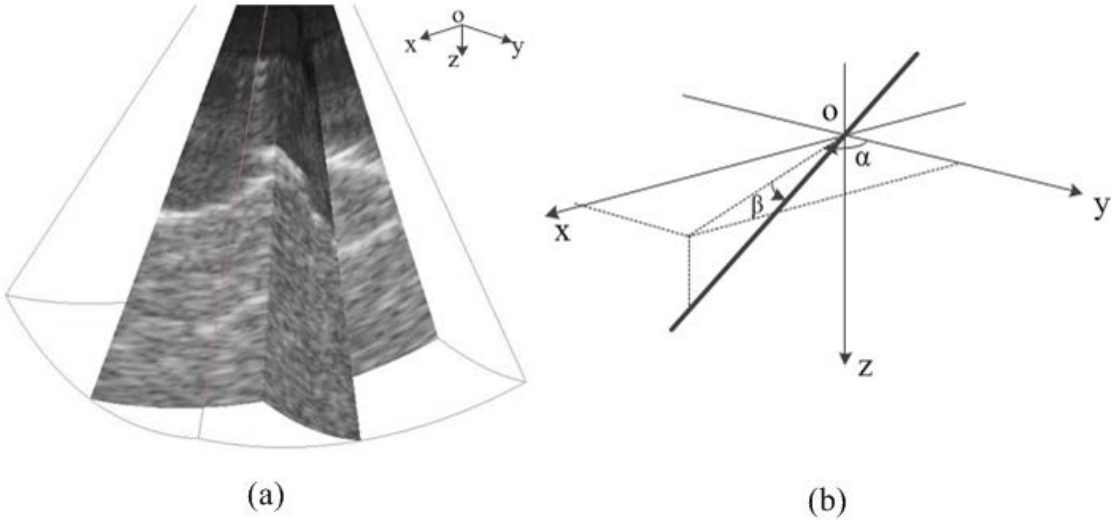

Fig. 5-2 The definition of the needle's two direction angles: (a) the original 3D US volume of PVA phantom; (b) the definition of the direction angles α and β.

Breast biopsy: the RANSAC with ML algorithm is also tested on three real data sets of live breast tissue (Fig. 5-3) with an 11-gauge straight biopsy needle (1 mm outer diameter). Three-dimensional US images were acquired using the GE Voluson E8 scanner with a 12-MHz probe. The size of all volumes was 273 × 383 × 208 voxels.

The needle position for real data sets was determined as an average location given by eight observers. The mean variability for human observers was less than 0.4mm.

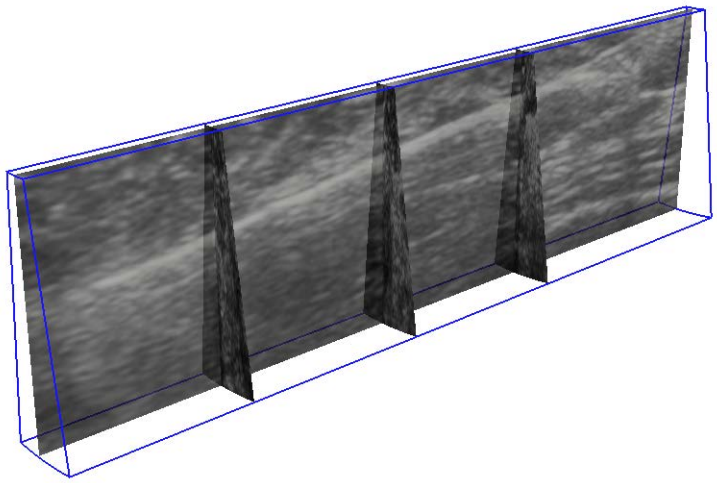

Fig. 5-3 3D US volume of breast biopsy with a needle. This is a sub-volume with 170 × 383 × 130 voxels from the original volume.

5.5.2 Tool localization — testing the complete chain

The complete proposed localization method was evaluated in terms of the success rate, axis accuracy and the calculation time. Axis accuracy ε_{axis} has the same definition as mentioned in Section 4.2, equation (4.5). Fig. 5-4 gives a intuitive definition of ε_{axis}.

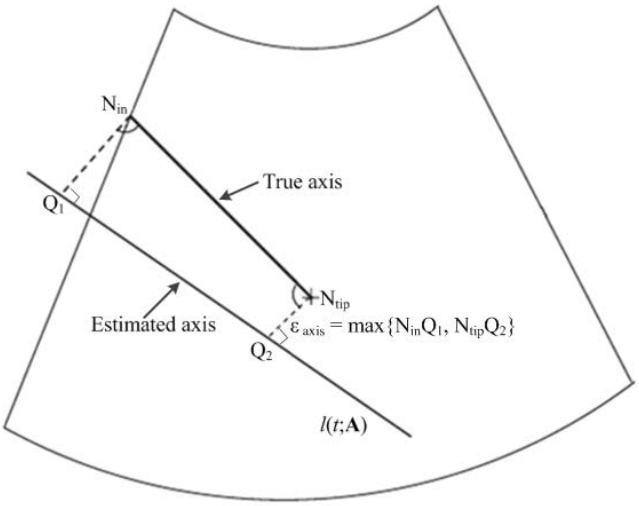

Fig. 5-4 The definition of axis accuracy ε_{axis}.

In [Mari *et al.* (2011)], it is claimed that for clinical biopsies, an error of a few millimeters can be acceptable. Consequently, the localization was considered to be a failure when the axis accuracy ε_{axis} was greater than a threshold (set at 3mm) and failures were excluded from accuracy calculations.

We considered two classifiers for the voxel classification step: (i) a cascaded classifier denoted Casc and (ii) a linear SVM classifier denoted SVM; and three inlier classifiers for the axis estimation step: (i) a linear SVM classifier denoted SVM, (ii) AdaBoost denoted ADA, and (iii) WaldBoost denoted WALD. These constitute six variants of the proposed method.

The RANSAC with ML method (Section 5.2) was compared to two variants (AxShp and IntDstr) of the previously described RANSAC localization method (Appendix B) [Uherčík *et al.* (2010)], and the ROI-RK method. The calculation time reported includes line filtering and pre-processing.

5.5.3 Tool localization on the simulated data

For the simulated data, the proposed algorithm has been tested on two different contrast ratios (CRs). The CR_{th} calculated using equation (4.2) is used to define the image quality. The results (axis accuracy, success rates, calculation time) for high CR

data (Fig. 5-1 (a)) are reported in Fig. 5-5. The RANSAC only method with AxShp and IntDstr model has the lowest success rate. Previously described ROI-RK method is faster than the RANSAC with ML algorithm, but the axis accuracy is also a little larger. The new method using different classifiers has the success rate lager than 90 %, and with the cascade classifier it can be as fast as the earlier methods.

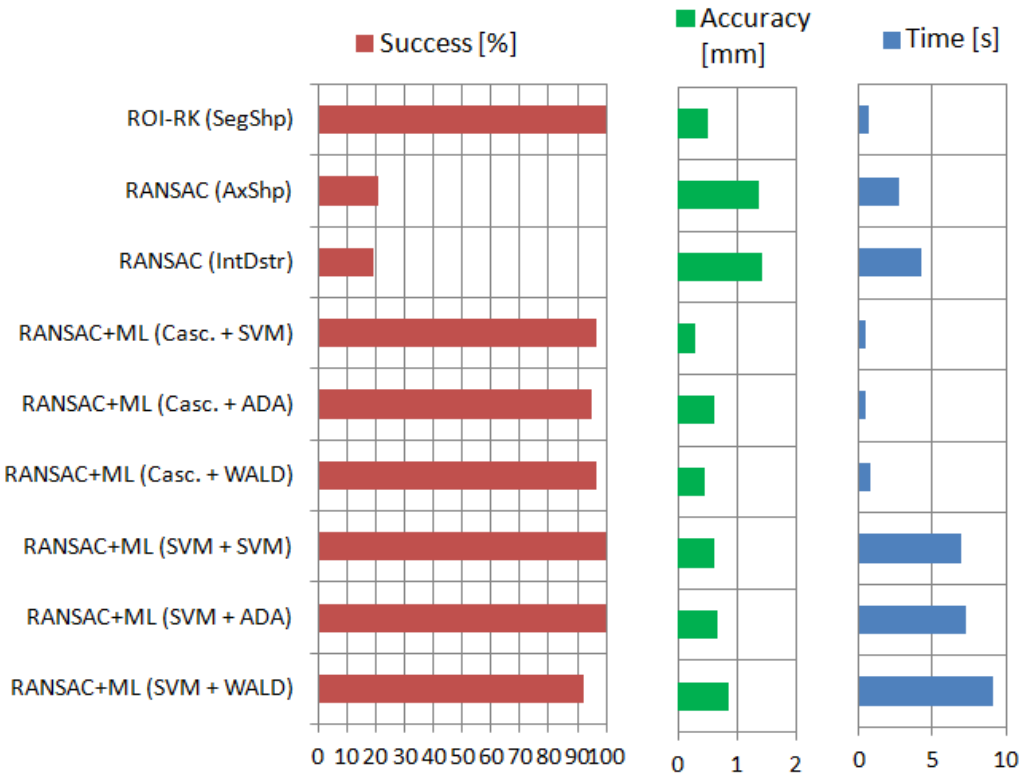

Fig. 5-5 Results of the different tool localization methods on simulated data with high CR (CR_{th} = 1.26). The first column is the success rate for all the methods expressed as a percentage; the second column is the axis accuracy in mm; the third column is the calculation time for each method.

Fig. 5-6 shows the results for more difficult synthetic data with a low CR (see Fig. 5-1 (b) for an example). The methods using only RANSAC algorithms have a low success rate. The best performance among RANSAC with ML methods is achieved using the combination of SVM + ADA classifiers; the following is the SVM + SVM classifier. The cascaded classifier decreases the overall time but increases the number of failures.

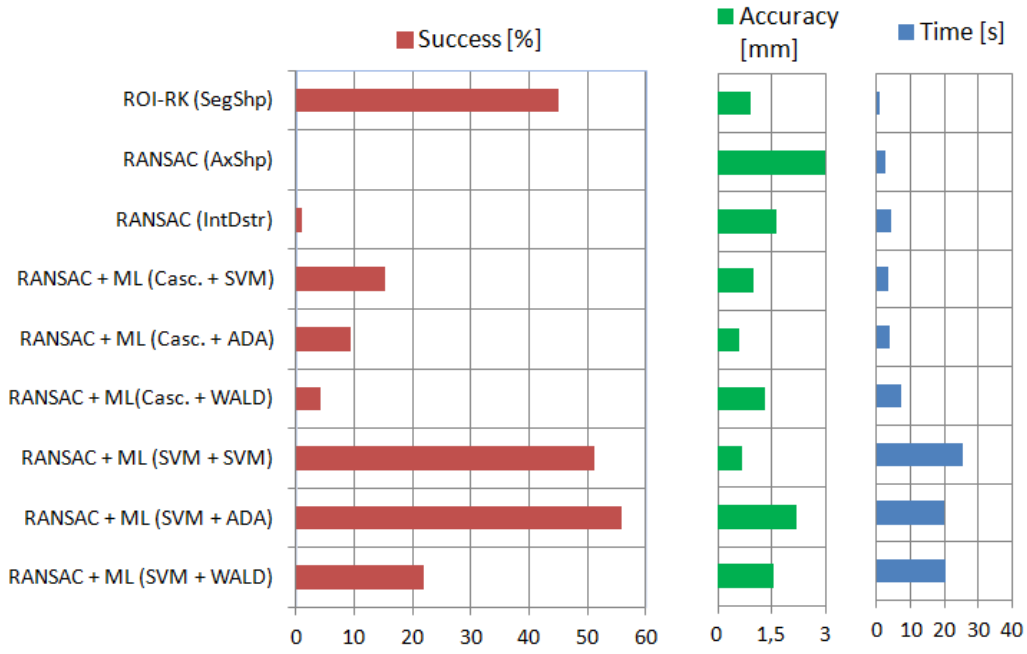

Fig. 5-6 Results of the different tool localization methods on simulated data with low CR (CR_{th} = 0.94). The first column is the failure rate for all the methods expressed as a percentage; the second column is the axis accuracy in mm; the third column is the calculation time for each method.

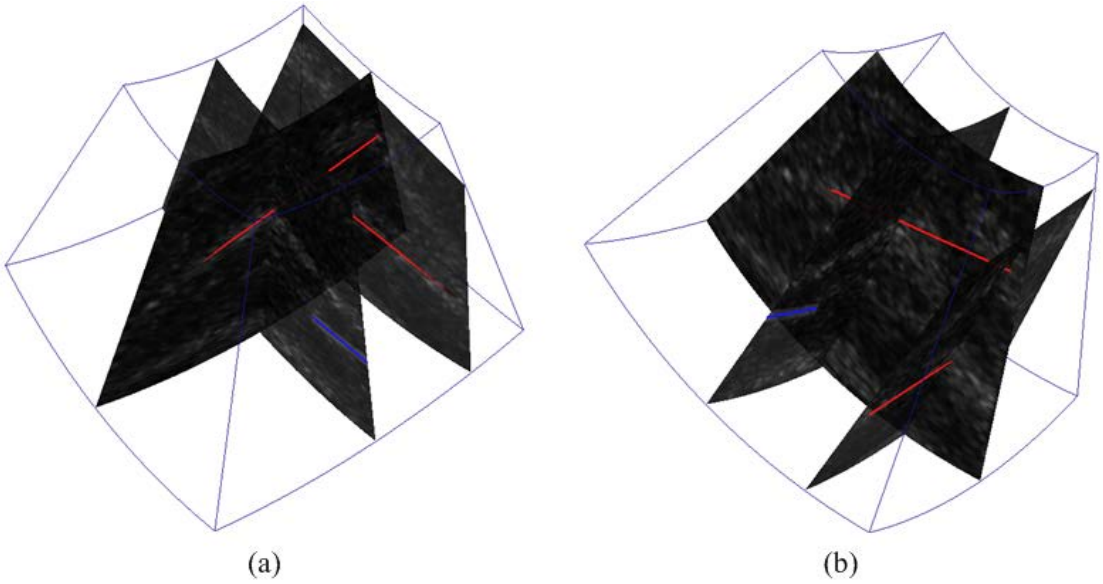

Fig. 5-7 Visualization of the localization results in simulated 3D US data with a low CR. The blue line shows the correct position computed using RANSAC with ML algorithm (using SVM classifiers). Two red lines show examples of failures using RANSAC only (tool model AxShp).

5.5.4 Tool localization on real data

The results on real data of the PVA phantom are shown in Fig. 5-8 and an example of a localization result using RANSAC with ML algorithm and RANSAC only algorithm is shown in Fig. 5-9. All methods not using line filters fail in 80% - 100% of cases, mostly because of a presence of a highly echogenic 2D interface. The best performance with respect to the number of failures is achieved by using the combinations of Casc + ADA, Casc + WALD and SVM + ADA classifiers. The use of a cascade classifier in the pre-segmentation phase reduces the calculation time; consequently, considering the time aspect, the Casc + ADA and Casc + WALD classifiers are better than the SVM+ADA classifier.

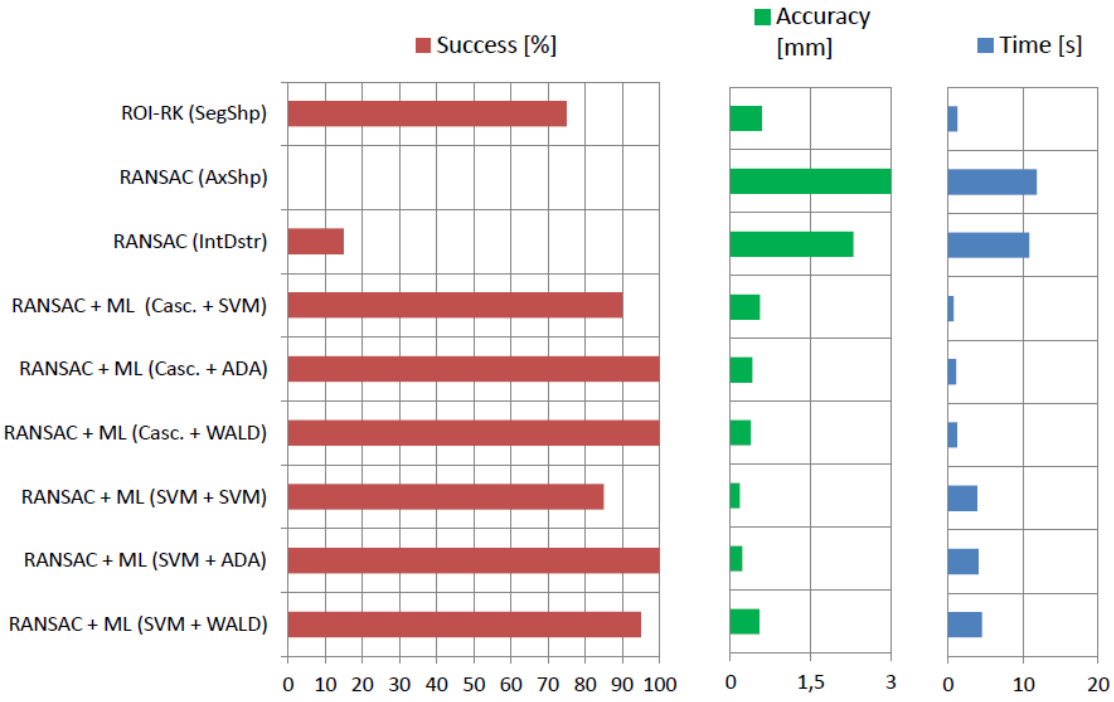

Fig. 5-8 Results of tool localization on the PVA cryogel phantom. The first column is the failure rate for all the methods expressed as a percentage; the second column is the axis accuracy in mm; the third column is the calculation time for each method.

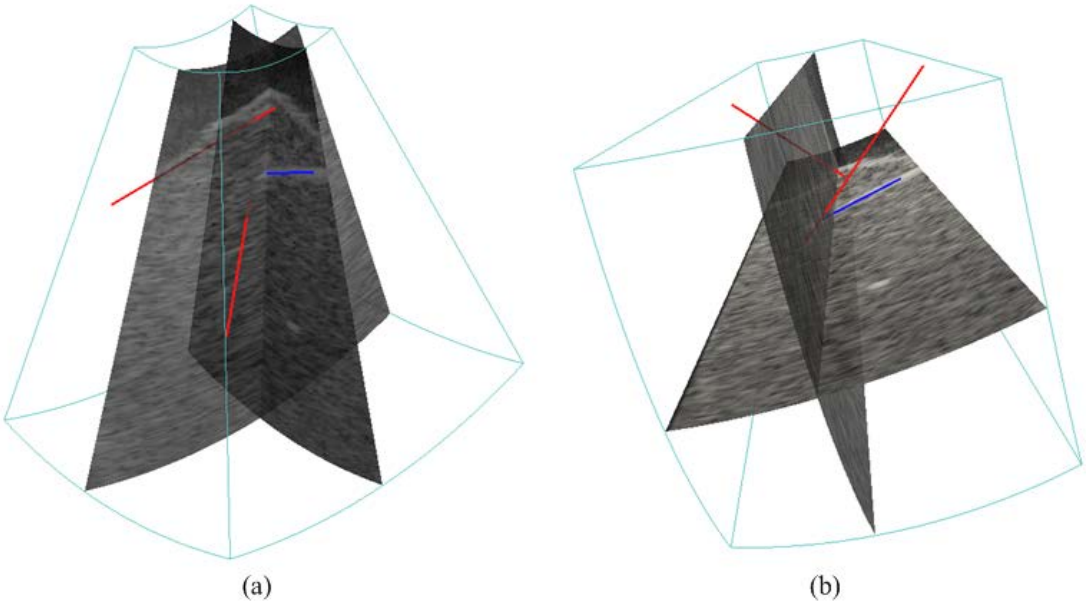

Fig. 5-9 Visualization of the localization results in 3D US data of the PVA phantom. The blue line shows the correct needle position computed using RANSAC with ML algorithm (using SVM classifiers). Two red lines show examples of failures using only RANSAC (tool model AxShp) — the localization method was confused by the high intensity layer on the top or in the data volume.

Finally, the results on the three breast biopsy data sets are presented in Fig. 5-10. An example of a localization result using the previous method, and an example of the line-filtering localization method are demonstrated in Fig. 5-11. Methods using only RANSAC algorithm fail most and with a large axis accuracy. Among the line-filtering methods, combining Casc + ADA classifiers works best. Following is the combination of SVM + ADA classifiers, which has a success rate of 90 % However, the calculation time for ML algorithms using SVM classifiers are all longer than 400 s.

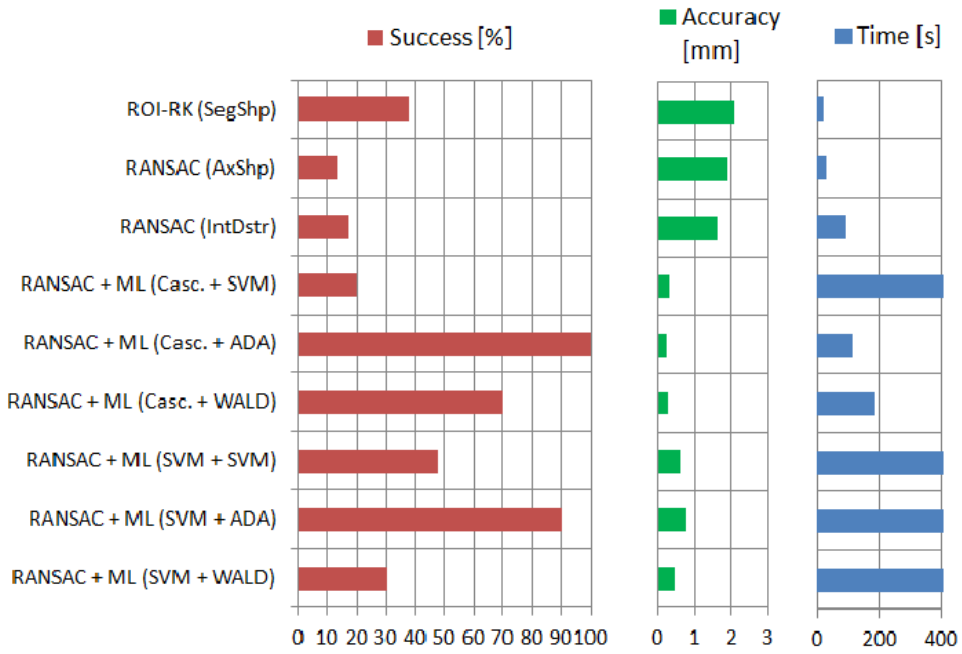

Fig. 5-10 Results of tool localization on real data of breast biopsy. The first column is the success rate for all the methods expressed as a percentage; the second column is the axis accuracy in mm; the third column is the calculation time for each method.

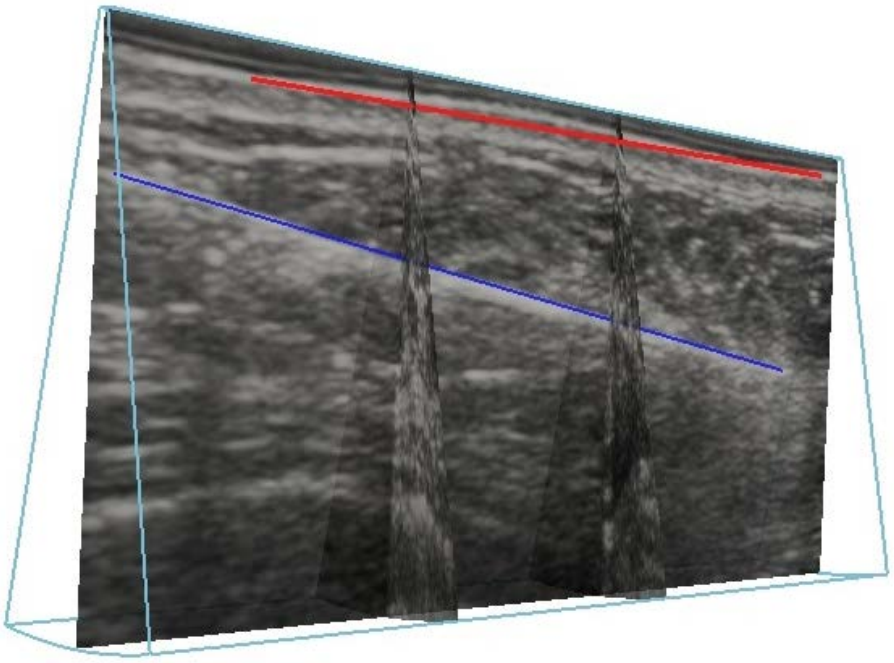

Fig. 5-11 Visualization of the localization result in 3D US data of the breast biopsy. The blue line shows the correct tool position computed using RANSAC with ML algorithm (using

SVM classifiers). The red line shows an example of failures using RANSAC only (tool model AxShp) — the localization method was confused by the high intensity layer on the top.

5.6 Discussion

The Hessian based line structure enhancement method presented herein was only used to calculate the tubular feature of a straight needle. It is also capable of enhancing the contrast between needle and background (for example for visualization purposes) even in the case of a curved needle (C-like deformation or deformation of a higher degree). Such curvatures can typically appear for thin micro-electrodes (diameter < 0.3 mm). However, in this chapter, the assumption that the biopsy needle is thick enough and does not have a deformation is used, and the tool model for the RANSAC algorithm is defined as a straight line. Extending model fitting to n = 3 (polynomial curves of order 3, equation (3.15) section 3.2.2), using the result of locally line-filtered 3D volumes could make it possible to detect curved tools. Fig. 5-12 demonstrates one example with a curved needle in which line filtering improves the contrast of the tool under the assumption of local linearity. The advantage of this research is that the method proposed in Chapter 3 and this chapter can be extended to curved model fitting in the future. Note, however, that in biopsies, the needle is quite thick and bending of the needle is extremely rare.

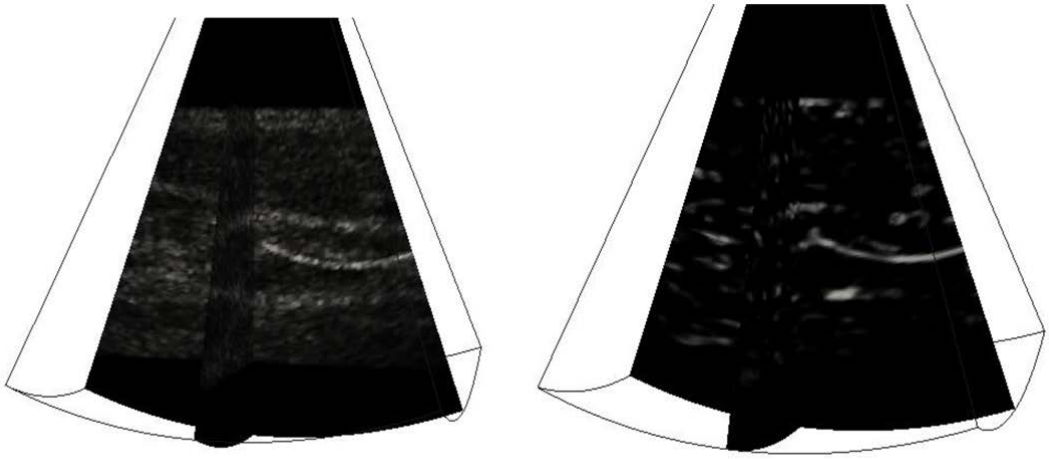

Fig. 5-12 Example of the line-filtering results with a curved needle: a) original 3D US image simulated using FIELD II, b) the output of line filtering using Frangi's method.

Table 5-6 Mean contrast ratio improvement (equation (3.14)) for the three line-enhancement methods using the simulated volume with a curved needle. Frangi's measurement has the best performance.

Data type	Line-enhancement methods		
	Frangi	Sato	Li
Simulation curved	**4.25**	2.97	2.71

5.7 Conclusion

In this chapter, the RANSAC with ML algorithm is proposed. Unlike the ROI-RK method which uses a fixed tool model for RANSAC algorithm to localize the needle position, the RANSAC with ML algorithm uses the statistic feature model. This method uses the different combinations of classifiers and the features extracted from the 3D US volume to classify the needle voxels from the background voxels, thus locate the position of the needle. The experiments have been done using the simulated and real US volumes, and the result shows that the RANSAC with ML algorithm has high success rate and accuracy, however, in some situation, the calculation time is a bit long.

PART III

Conclusion and Perspective

Chapter 6

Conclusion and Perspective

Contents

6.1 Conclusion

The main contribution of this thesis is the development of an automatically localization and tracking method for biopsy needle navigation using 3D ultrasound – the ROI-RK method. Different series of 3D US volumes with an inhomogeneous background simulated from a real scatter map and an added needle for ground truth have been generated to test the performance of the proposed method. These first simulation results show that this method is robust and fast enough to be adapted for real-time clinical applications.

The ROI-RK method involves two steps: the ROI initialization step and the micro tool localization and tracking step. In the first step, the Hessian based line filter method has been implemented to reduce the speckle noise of the whole 3D volume, meanwhile enhance the line structure of the biopsy needle. Thus a ROI can be well initialized and it helps to obtain an accurately localization and tracking result. The localization error for tip position is within 1 mm, and the axis accuracy within 1.4 mm. The shift of the two orientation angles α and β is less than 2°. The localization result is accurate enough for clinical applications.

In order to fit a dynamic situation, the Kalman filter and speckle tracking strategy have been implemented in the ROI-RK method. Therefore, the movement of the needle can be estimated and the ROI can be properly predicted and updated in the new coming 3D US volume, and this leads to a robust performance for the ROI-RK method in dynamic situations. An error diagnosis system has also been implemented in case of the situation that a sudden disappearance of needle occurs in one volume during the tracking procedure. When the localization difference between the present step and the previous step is larger than 3 mm, this system can use the previous

information to re-generate the ROI in the new-coming US volume and thus keeps the robustness of the ROI-RK method.

The ROI choosing strategy also helps to reduce the running time for the biopsy needle localization procedure because most part of outliers are eliminated. In the ROI, the processing part is effectively limited and it leads to an average calculation time of around 0.1 s for one 3D volume, which satisfies the demand of real-time applications.

Another biopsy needle localization method, the RANSAC with ML algorithm is also proposed in this thesis. In situations where the speckle noise is too strong and using only the intensity value, it is impossible to classify the needle voxels from the background. This method uses not only the intensity of the voxels, but also the structure information extracted from the volume to construct the feature vector of the voxels. Then different ML algorithms have been implemented to classify the feature vectors thus separate the needle voxels. The cross validation has been done using simulated volumes to evaluate the performance of the different classifiers, and they all have better performance than the threshold classifier using only the intensity value. The RANSAC with ML algorithm has also been tested using synthesized and real data, and the results show that it has a lower failure rate and higher localization accuracy.

6.2 Perspective

The ROI-RK method can be further improved by using the model of polynomial curves with order 3 or higher so that it can also localize the thinner micro tools like electrodes, which could have a problem of bending during the insertion.

More experiments on the *in-vitro* and *in-vivo* US data volumes should be done to further validate the performance of the ROI-RK method. For the *in-vitro* experiments, an inhomogeneous phantom could be made for mimicking the structures of the tissue. Moreover, the transparent or semi-transparent material can be used for an easy measurement of the ground truth position of the inserted biopsy needle. A mechanical insertion system could be employed to perform the constant velocity inserting procedure of the needle, thus verify the tracking loop of ROI-RK method. Possible collaborations could be carried out with Lab. Irisa using their robotic systems. After the *in-vitro* validation, this method can pass to *in-vivo* data. However, in the *in-vivo* situation, for example, the liver, the movement of the tissue caused by respiration will increase the risk of losing the biopsy needles during the tracking procedure. The further research on the tissue motion model could be done. Because the respiration is a regular movement, the ROI-RK method can be improved by adding the model of the respiration to the control matrix and control vector in the Kalman filter. The *in-vivo* experiments with an experienced clinician are also expected in future work.

The ROI-RK method will be further implemented on a commercial US machine to test the *ex-vivo*, *in-vitro* and *in-vivo* applications. As it is known that in the real US

volume, the appearance of the biopsy needle could be influenced by the point spread function (PSF) of the system. As a consequence it might be interesting to do some further research on deconvolution methods to improve the resolution of the real 3D US volume and make the structure of the micro tools clearer.

On this step, the 2D mechanical probe is used to obtain the 3D US volumes. The average time for generating a volume is several seconds. This reduces the advantage of real time for US systems. In order to satisfy the real-time applications, a fast imaging technology should also be implemented in the commercial US system to get a high volume rate, for example, using 2D array probes to generate 3D US volumes is much faster than 2D mechanical probes.

New envelope detecting technology can also be implemented to enhance the contrast between the metal biopsy needle and background tissue. An algebraic framework for 3D analytical signals have been proposed in [Wang *et al.* (2012)]. Their results show that the 3D envelope detection technology performs better than the traditional 1D envelope result (Hilbert transform).

Due to the electronic noise, sometimes the speckle tracking method cannot find the proper region to fit the kernel region, and this induces error in the motion estimation thus lost the target. So, a better motion estimation method could be applied to improve the result of motion estimation. For example, the mean-shift tracking algorithm is proved to be a simple and efficient approach used in computer vision [Ning *et al.* (2012)]. It could be implemented to track the needle tip in the series of 3D US volumes.

PART IV

Version Brève en Français

Chapter 7

Résumé Français

Contents

7.1 Introduction

7.1.1 Motivation

Dans les examens médicaux et les actes de thérapie, les techniques minimalement invasives sont de plus en plus utilisées. Des mini instruments sont utilisés pour extraire des échantillons de cellules (comme des aiguilles de biopsie) ou pour effectuer des traitements.

Pour réduire les traumatismes et améliorer la précision de leur localisation, différentes modalités d'imagerie médicale, comme la tomodensitométrie, l'imagerie par résonance magnétique (IRM) et l'échographie, sont employées pour guider les micro-outils insérés dans les tissus humains. La tomodensitométrie et l'IRM ont quelques avantages comme (i) une résolution des images élevée ; (ii) la possibilité d'imager tous les types d'organes humains. Néanmoins, les inconvénients de ces deux techniques ne peuvent être ignorés. La tomodensitométrie délivre une dose relativement élevée de rayonnement pour le patient. Le scanner IRM produit un bruit fort, et le patient est dans un espace clos rendant sa position inconfortable. Le mouvement affecte la qualité des images d'IRM, donc le patient doit rester immobile pendant une longue période. De plus, les machines d'IRM sont très coûteuses, ce qui conduit à un coût élevé des examens.

Pour éviter les inconvénients ci-dessus, l'échographie est sélectionnée pour suivre l'insertion des aiguilles de biopsie. En effet, il y a plusieurs avantages pour l'imagerie ultrasonore (US): (i) le système bénéficie d'un temps d'acquisition court, l'imagerie est effectuée en temps réel, (ii) il n'existe pas de rayonnement ionisant, il est totalement sûr pour le patient et le praticien; (iii) la qualité des images délivrées par les échographes modernes a été beaucoup améliorée; (iv) le coût d'un échographe ultrasonore est raisonnable par rapport à des systèmes de tomodensitométrie ou d'IRM, et les frais d'examen sont réduits; (v) les appareils sont portables. Pour toutes ces raisons, on a choisi la technique de l'image ultrasonore comme méthode d'aide à la navigation de micro-outils.

Habituellement, les radiologues utilisent des transducteurs ultrasonore 1D pour balayer la région cible, et obtenir l'image ultrasonore 2D affichée sur l'écran. Il est par contre difficile d'aligner le plan de balayage avec l'axe de l'aiguille pour obtenir la visualisation complète de l'aiguille [K Chin *et al.* (2008)]. Il existe principalement deux approches pour l'insertion de l'aiguille de biopsie aidées par l'échographie 2D: guidées ou à main levée [Allen *et al.* (2006)]. Dans l'approche guidée, un dispositif fixé à la sonde est utilisé pour guider l'aiguille dans le plan de balayage de la sonde ultrasonore. En revanche, l'approche à main levée est techniquement plus difficile et prend plus de temps à maitriser, mais elle offre une plus grande flexibilité. Dans cette approche, le radiologue manipule la sonde ultrasonore avec une main tandis que l'autre tient l'aiguille. Durant la procédure, il est nécessaire de glisser, incliner, tourner la sonde en permanence de manière à aligner le faisceau ultrasonore et l'axe de l'aiguille [KJ Chin (2012)]. Mais, les aiguilles et les tissus biologiques ont des structures en trois dimensions (3D), et la plupart du temps les aiguilles ne correspondent pas parfaitement au plan d'acquisition ultrasonore 2D. Une seule partie de l'aiguille est visible. D'autres fois, le radiologue peut voir les tissus et les organes clairement, mais la visualisation de l'aiguille est très difficile. Cela augmente le risque de traumatisme. En conséquence, l'échographie 3D associée à des techniques de localisation présente un intérêt majeur pour aider ces gestes médicaux.

Nous proposons d'utiliser un système ultrasonore 3D pour localiser et suivre l'aiguille de biopsie. Le volume 3D peut être obtenu avec une sonde 1D classique déplacé mécaniquement par un moteur, par mains libres à l'aide d'un calibreur, ou d'une sonde matricielle 2D [Fenster *et al.* (2001)]. A l'intérieur d'un volume 3D, une meilleure position relative de l'aiguille de biopsie et du tissu peut être obtenue. De plus, grâce à l'acquisition 3D, un plan qui contient l'aiguille peut toujours être extrait du volume et visualisé. Cependant, il est encore difficile pour les radiologues de localiser l'aiguille dans un volume 3D sans l'aide de logiciels qui peuvent localiser automatiquement les micro-outils.

Dans le but d'une localisation précise et d'un suivi de l'aiguille de biopsie robuste dans des volumes ultrasonore 3D, nous proposons de développer un algorithme qui localise automatiquement la position de l'aiguille dans le volume 3D, et affiche le plan contenant l'outil et le plan perpendiculaire à l'outil au niveau de l'extrémité. Comme le processus d'insertion dans les tissus humains est un processus dynamique, l'algorithme doit être capable de suivre automatiquement l'aiguille dans des situations dynamiques.

7.1.2 Objectif de la thèse

Notre objectif est de développer un algorithme robuste qui peut localiser et suivre une aiguille de biopsie insérée dans le tissu humain en utilisant une imagerie 3D ultrasonore temps réel. Il ya plusieurs tâches à réaliser:

- **La réduction du bruit**. L'imagerie ultrasonore souffre d'un bruit granulaire (« speckle »). Ce type de bruit réduit le taux de contraste (CR) de l'image ultrasonore. Il influence l'imagerie des objets minuscules, comme en particulier l'extrémité de l'aiguille, et peut conduire à un résultat de localisation inexacte. L'algorithme implique une stratégie de réduction de bruit granulaire.
- **Précision.** La navigation précise d'outils chirurgicaux est cruciale, car l'algorithme développé sera utilisé dans des applications cliniques, la précision de la méthode ne peut pas être négligée. Pour les biopsies cliniques, une erreur de quelques millimètres peut être acceptable [Mari *et al.* (2011)]. Dans notre travail, la précision de localisation de l'aiguille de biopsie souhaitée est de 2 à 3 mm avec un fond non homogène.
- **Robustesse.** Notre algorithme doit localiser et suivre l'aiguille de biopsie dans une situation dynamique. Parfois, la mauvaise qualité d'image ultrasonore mène à l'échec de la localisation des instruments médicaux. Donc, un système de prédiction de position robuste doit être mis en œuvre.
- **L'application en temps réel.** L'un des principaux intérêts des systèmes ultrasonores est que les images sont affichées en temps réel. Les systèmes traditionnels ultrasonores ont une cadence d'imagerie de 20 à 50 images/s. Les méthodes d'imagerie 3D doivent conserver ces caractéristiques, ou au minimum une acquisition d'une dizaine de volumes/s. Les sondes 3D mécaniques disponibles actuellement prennent quelques secondes pour acquérir un volume 3D ultrasonore. Les sondes matricielles 2D en cours de développement devraient atteindre cet objectif. Ainsi, pour satisfaire la contrainte temps réel, notre algorithme doit être capable de traiter un volume 3D en un dixième de seconde.

7.2 Contributions

7.2.1 La méthode de « ROI-RK »

Il est très difficile pour les radiologues de détecter le plan correct qui contient l'aiguille dans le volume ultrasonore 3D. Par conséquent, les méthodes de détection automatique d'une aiguille dans des volumes ultrasonores 3D sont devenues très importantes. Il ya plusieurs défis pour les algorithmes existants de localisation de l'aiguille. Tout d'abord, le volume ultrasonore 3D a un bruit de texture, et certaines parties du tissu peuvent avoir le même niveau d'intensité que l'aiguille; dans ce cas, les algorithmes de localisation ne parviennent pas à détecter la position correcte de l'aiguille. En second lieu, il existe des dizaines de milliers de voxels dans une série de volumes 3D ultrasonores, ce qui conduit à une grande quantité de calculs. En troisième lieu, la plupart des méthodes de localisation détecte l'aiguille dans un seul volume. Mais aucune méthode n'est testée dans une situation dynamique. Pour une tâche de suivi, le procédé de localisation doit être suffisamment robuste pour suivre la position de l'aiguille dans une série de volumes. De plus, le temps de traitement doit être suffisamment court pour une application en temps réel. Dans le but de répondre à ces trois contraintes, nous proposons une méthode basée sur un algorithme RANSAC et un filtre de Kalman. De même l'étude est limitée à une région d'intérêt (ROI) pour obtenir une localisation robuste et le suivi de la position de l'aiguille de biopsie en temps réel. Une abréviation anglaise pour cette méthode est ROI-RK. La méthode ROI-RK est principalement basée sur trois hypothèses :

H.1. L'intensité des voxels de l'aiguille est plus élevée que l'intensité des voxels de fond.

H.2. L'aiguille est considérée comme un objet long, droit et cylindrique.

H.3. La trajectoire d'insertion reste toujours suivant la même direction. Même si un mouvement relatif peut se produire, il n'influence pas la direction principale d'insertion.

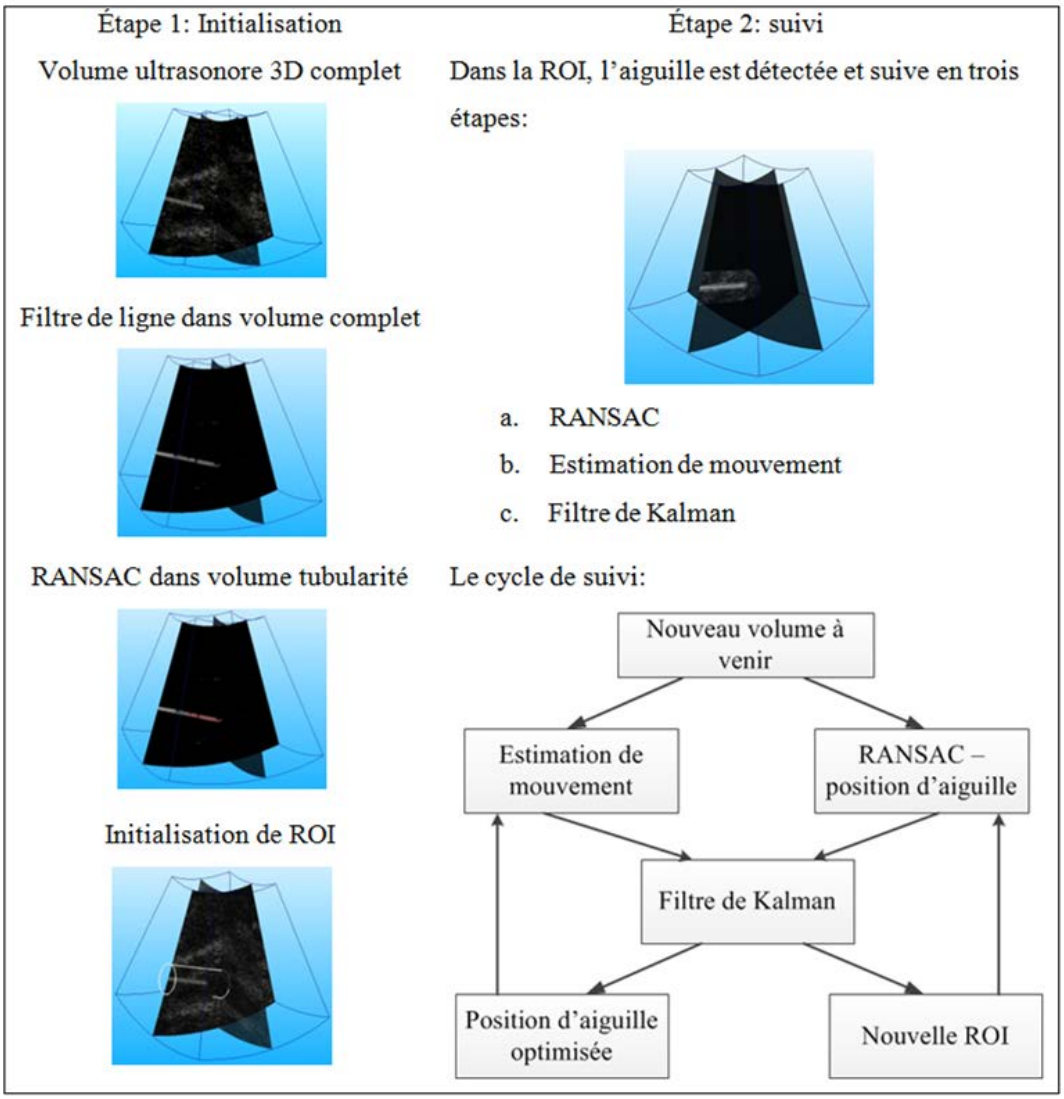

Fig. 7-1 Vision globale de la méthode ROI-RK: étape 1: initialisation, et étape 2: cycle de suivi.

Il existe principalement deux étapes dans le processus ROI-RK (Fig. 7-1):

Étape 1: l'étape d'initialisation - Pour améliorer le contraste entre l'aiguille et le fond, un filtre de ligne (« line filter »)3D [Frangi *et al.* (1998)] est utilisé dans le volume 3D complet pour obtenir un volume dit de tubularité. L'algorithme RANSAC s'exécute dans ce volume pour obtenir une position initiale de l'aiguille. En utilisant cette position, la ROI est initialisée automatiquement.

Étape 2: l'étape de suivi - Les opérations suivantes ne sont exécutées qu'à l'intérieur de la ROI. L'aiguille de biopsie est détectée et elle est suivi en trois étapes: (a) l'algorithme de RANSAC est utilisé pour détecter la position de l'aiguille dans la ROI ; (b) une méthode d'estimation de mouvement est utilisée pour estimer la vitesse

de l'extrémité de l'aiguille ; (c) le filtre de Kalman est utilisé pour mettre à jour la ROI et affiner la position de l'aiguille.

(a) L'algorithme RANSAC proposé se compose de quatre sous-étapes:

1. Classification par seuillage - cette étape vise à réduire le nombre de voxels sur la base de l'hypothèse H.1. Dans un volume 3D ultrasonore, les voxels d'aiguilles représentent moins de 1% de l'ensemble du volume. Par conséquent, le plus petit seuillage est fixé pour conduire à ce que 99 % des voxels de plus faible intensité soient considérés comme le fond.
2. Localisation de l'axe - cette étape utilise l'algorithme RANSAC pour estimer une position approximative de l'axe de l'aiguille. Cette étape renvoie la position approximative de l'aiguille définie par deux points.
3. Optimisation locale - cette étape utilise un algorithme d'optimisation locale pour trouver une position de l'aiguille plus précise en utilisant le résultat de RANSAC.
4. Localisation de l'extrémité - cette étape utilise le changement brusque de l'intensité le long de l'axe estimé à l'étape 3 pour identifier son extrémité.

(b) On utilise la méthode de mise en correspondance de bloc (« block matching ») pour mesurer la vitesse de l'extrémité de l'aiguille. Tout d'abord, une petite région 3D à proximité de l'extrémité de l'aiguille est choisie dans le premier volume comme le noyau. Ensuite, une région plus grande est choisie comme zone de recherche dans le volume suivant. Au cours de la procédure de poursuite, la région du noyau glisse voxel par voxel dans la région de recherche, et la corrélation croisée normalisée est calculée pour comparer la ressemblance entre les deux régions. La différence de coordonnées entre la région de noyau et la meilleure région de concordance indique le déplacement de l'aiguille. La vitesse de l'extrémité est obtenue en divisant le déplacement par le temps.

(c) On a choisi un modèle de vitesse constante pour le filtre de Kalman. Avec ce modèle, le vecteur d'état $\mathbf{s}$ du système est $\mathbf{s}=[\beta,\alpha,v_\beta,v_\alpha,\mathbf{p}_t,\mathbf{v}_t]^T$, et les équations de mise à jour de temps sont:

$$\hat{\mathbf{s}}_k^- = \mathbf{F}\hat{\mathbf{s}}_{k-1} \tag{7.1}$$

$$\mathbf{P}_k^- = \mathbf{F}\mathbf{P}_{k-1}\mathbf{F}^T + \mathbf{Q} \tag{7.2}$$

avec $\mathbf{F}=\begin{bmatrix}\mathbf{I}_{2\times2} & dt\times\mathbf{I}_{2\times2} & \mathbf{0}_{2\times6}\\ \mathbf{0}_{2\times2} & \mathbf{I}_{2\times2} & \mathbf{0}_{2\times6}\\ \mathbf{0}_{3\times4} & \mathbf{I}_{3\times3} & dt\times\mathbf{I}_{3\times3}\\ \mathbf{0}_{3\times4} & \mathbf{0}_{3\times3} & \mathbf{I}_{3\times3}\end{bmatrix}$, $\mathbf{p}_t=\left(x_t,y_t,z_t\right)$ est le repère de position de l'extrémité de l'aiguille, et $\mathbf{v}_t=[v_{tx},v_{ty},v_{tz}]$ est le vecteur vitesse de l'extrémité de l'aiguille. *dt* représente l'intervalle de temps. Le bruit de traitement est supposé gaussien. Le vecteur de mesure est défini comme $\mathbf{z}=\left[\beta,\alpha,\mathbf{p}_t,\mathbf{v}_t\right]^T$. Les vitesses

angulaires v_α , v_β ne sont pas inclues pour les raisons suivantes: (i) le chemin d'insertion est toujours sur la direction de l'axe, les vitesses angulaires sont considérées comme $v_\alpha = v_\beta = 0$; (ii) il n'y a pas de méthode appropriée pour mesurer les vitesses angulaires. Les deux angles α , β et la position $\mathbf{p}_t$ peuvent être mesurés par l'algorithme de RANSAC. La vitesse de l'extrémité $\mathbf{v}_t$ peut être estimée par la méthode d'estimation de mouvement. La matrice de mesure est $\mathbf{H} = \begin{bmatrix} \mathbf{I}_{2\times2} & \mathbf{0}_{2\times8} \\ \mathbf{0}_{6\times4} & \mathbf{I}_{6\times6} \end{bmatrix}$. Le bruit de mesure est aussi une distribution de Gauss qui est estimée par un grand nombre d'essais répétitifs.

Pour évaluer les performances de la méthode ROI-RK, différentes séries de volumes 3D ultrasonores sont simulés. Dans chaque série, la longueur de l'aiguille est changée pour simuler une situation dynamique. Le premier groupe compare la robustesse de la méthode ROI-RK par rapport à la méthode RANSAC avec des angles d'insertion différents et un rapport de contraste (« contrast ratio »). La Fig. 7-2 montre une comparaison de résultats de localisation et de suivi utilisant deux méthodes différentes : l'algorithme RANSAC unique et la méthode ROI-RK. D'après la Fig. 7-2, il est évident que la méthode ROI-RK est robuste et précise, mais l'algorithme de RANSAC est faible pour un procédé de suivi.

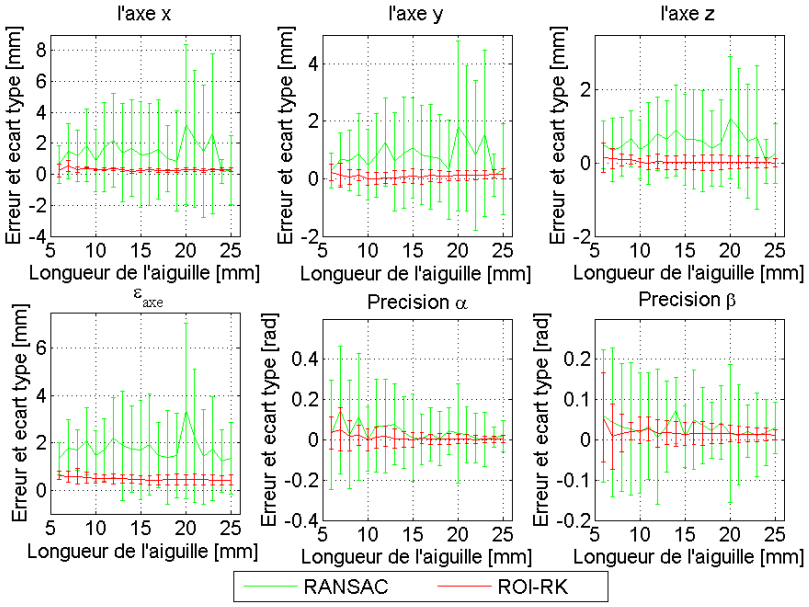

Fig. 7-2 La moyenne et l'écart type de l'erreur de l'extrémité (première ligne), $\varepsilon_{\text{axis}}$ (deuxième ligne, à gauche), α (deuxième ligne, au milieu) et β (deuxième ligne, à droite) pour les méthodes de RANSAC et ROI-RK avec $\alpha = 30^\circ$, $\beta = 73^\circ$.

L'influence du RC sur les conditions de défaillance de ROI-RK est aussi évaluée. Pour l'évaluation de la méthode, si une distance euclidienne supérieure à 3 mm est obtenue entre le bout estimé et le bout réel, ou entre l'axe estimé et l'axe réel, le procédé est considéré comme échec. Les RC sont entre 0.90 – 1.33. La Fig. 7-3 présente la courbe du taux de réussite de la méthode ROI-RK avec différents RC.

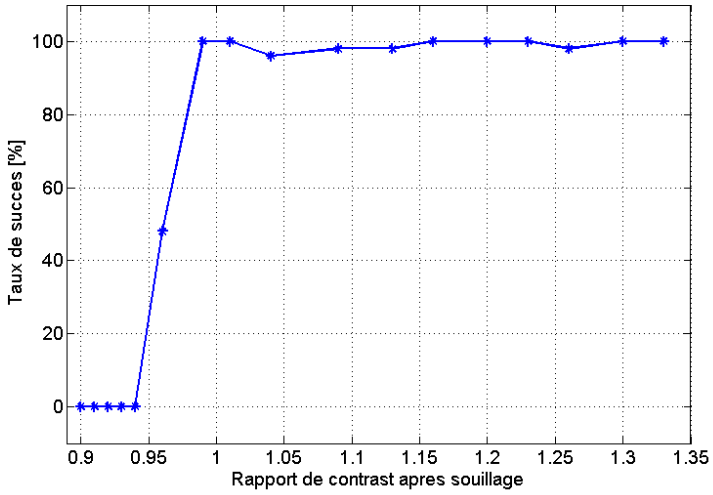

Fig. 7-3 Taux de réussite pour la méthode ROI-RK avec une valeur de RC différente. Ici, le pourcentage de seuillage est égal que 99% des voxels.

7.2.2 L'algorithme RANSAC avec apprentissage automatique

Dans la tâche de localisation d'un micro-outil à l'aide de systèmes ultrasonores 3D, certaines parties du tissu ont le même niveau d'intensité que l'aiguille de biopsie. Dans cette situation, l'utilisation seulement d'un seuil sur l'intensité des voxels pour classer l'aiguille et le tissu de fond n'est pas suffisante. Nous proposons d'extraire des caractéristiques de forme de l'aiguille pour aider à la localisation dans notre application. Le filtre de ligne à base de Hesse, qui est utilisé pour calculer le volume tubulaire de la méthode ROI-RK, a été mis en œuvre ici pour calculer les paramètres dits de tubularité des voxels. Plusieurs algorithmes d'apprentissage automatique (AA), comme le classifieur linéaire (CL), la machine à vecteurs de support (MVS), AdaBoost, ont été mis en œuvre dans l'algorithme de RANSAC pour une classification plus précise.

La procèdure de RANSAC comporte encore quatre étapes : (a) classification des voxels; (b) estimation de l'axe; (c) optimisation locale, et (d) localisation de l'extrémité. Dans l'étape (a), le vecteur de caractéristiques $\mathbf{m}_1(M)$ est utilisé :

$$\mathbf{m}_1(M) = \left[I(M), J(M) \right] \tag{7.3}$$

ici, M représente un voxel. $I(M)$ et $J(M)$ représentent l'intensité et la valeur de tubularité d'un voxel, respectivement.

Dans l'étape (b), un autre vecteur de caractéristiques $\mathbf{m}_2(M)$ est généré pour précisément classer les voxels d'aiguille comme des voxels « inliers »:

$$\mathbf{m}_2(M) = \left[I(M), J(M), d(M; \mathbf{A}), \delta(M; \mathbf{A}) \right] \tag{7.4}$$

ici, $\mathbf{A}$ est la matrice des coefficients d'une ligne choisie au hasard l ; $d(M; \mathbf{A})$ est la distance euclidienne du voxel à la ligne ; $\delta(M; \mathbf{A})$ est calculé comme :

$$\delta(M, \mathbf{e}_1) = \frac{\partial^2 f_V(M)}{\partial \mathbf{e}_2^2} + \frac{\partial^2 f_V(M)}{\partial \mathbf{e}_3^2} \tag{7.5}$$

ici, $f_V(\cdot)$ est la fonction de l'image. $\mathbf{e}_1$, $\mathbf{e}_2$ et $\mathbf{e}_3$ sont trois vecteurs unitaires orthogonaux, où $\mathbf{e}_1$ est le vecteur unitaires de l. Les étapes (c) et (d) sont les même que précédemment.

On a évalué les classifieurs : CL, MVS, AdaBoost, WaldBoost et Cascade en utilisant 18 volumes simulés différents. Dans les résultats de validations croisées, pour la classification des voxels, AdaBoost fonctionne mieux. Pour l'estimation de l'axe, le meilleur classifieur est MVS.

L'algorithme RANSAC avec AA est testé en utilisant des combinaisons différentes de classifieurs. Sur des données simulées avec un fort rapport de contraste (RC), la combinaison de Cascade plus MVS donne la localisation d'aiguille estimée avec la meilleure précision et le plus court temps de calcul. En testant sur les données simulées avec un faible RC et les données *ex-vivo*, la combinaison de MVS plus AdaBoost donne la meilleure précision de l'axe, mais avec un temps de calcul long (simulé bas RC : 40 s, ex-vivo : 280 s). La Fig. 7-4 présente un exemple de resultat de localisation en utilisant RANSAC avec AA et RANSAC seul.

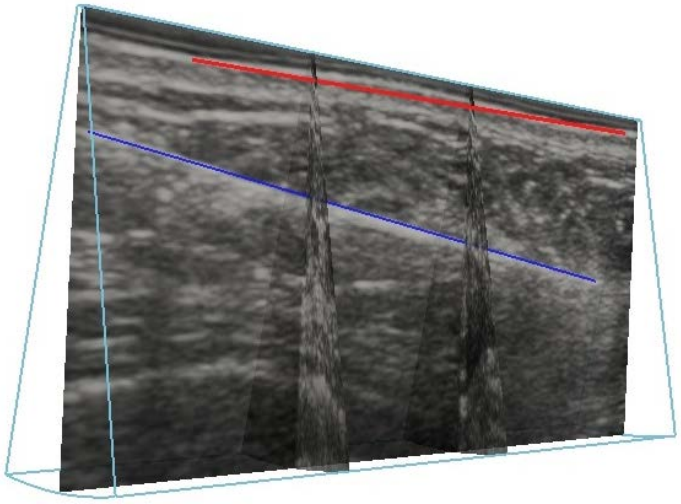

Fig. 7-4 Visualisation du résultat de la localisation dans les données de biopsie du sein en 3D. La ligne bleue montre la position de l'outil correctement calculée en utilisant des classifieurs MVS plus AdaBoost. La ligne rouge montre un exemple de défaillances sans apprentissage automatique - la méthode de localisation a confondu l'aiguille avec la bordure haute intensité au niveau d'un interface.

7.3 Conclusion et perspective

7.3.1 Conclusion

La principale contribution de cette thèse est le développement d'une méthode de localisation automatique et de suivi d'aiguille de biopsie en utilisant des ultrasons 3D - la méthode ROI-RK. Différentes séries de volumes ultrasonores 3D avec un fond hétérogène simulé ont été générées pour tester les performances de la méthode proposée. Ces premiers résultats de simulation montrent que cette méthode est assez robuste et peut être adaptée pour des applications cliniques en temps réel. L'erreur de localisation de l'extrémité de l'aiguille est inferieure à 1 mm. La précision de l'axe est inférieure à 1,4 mm. Le déplacement des deux angles d'orientation et inférieure à 2°. Grace à la stratégie de choix de la ROI, le temps d'exécution moyen de la procédure de localisation de l'aiguille de biopsie dans un volume est à peu près de 0,1 s.

Une autre méthode de localisation de l'aiguille de biopsie – l'algorithme RANSAC avec apprentissage automatique (AA) est aussi proposé dans cette thèse. Dans les cas où le bruit granulaire est trop fort et en utilisant uniquement la valeur d'intensité, il est impossible de classer les voxels de l'aiguille par rapport à l'arrière-plan. Cette méthode utilise non seulement l'intensité des voxels, mais aussi l'information de structure extraite à partir du volume pour construire le vecteur de caractéristiques des voxels. Ensuite, différents algorithmes AA ont été mis en œuvre pour classer les

vecteurs de caractéristiques pour séparer les voxels d'aiguilles. La validation croisée a été effectuée en utilisant des volumes simulés pour évaluer la performance des différents classifieurs, et ils ont tous de meilleures performances que le classifieur de seuillage en utilisant uniquement la valeur d'intensité. Le RANSAC avec AA a également été testé en utilisant des données de synthèse et réelles, et les résultats montrent qu'il a un faible taux d'échec et une plus grande précision de localisation.

7.3.2 Perspective

La méthode ROI-RK peut être améliorée en utilisant le modèle de courbes polynomiales de l'ordre de trois ou plus, aux cas où l'électrode pourrait avoir un problème de flexion au cours de l'insertion. Des expériences sur des volumes de données *l'in-vitro* et *l'in-vivo* aux ultrasons doivent être effectuées pour valider davantage les performances de la méthode ROI-RK.

Cette méthode sera encore mise en œuvre sur une machine ultrasonore. Comme il est connu l'apparition de l'aiguille de biopsie peut être influencée par la fonction d'étalement du point (PSF) du système. En conséquence, il pourrait être intéressant de faire des recherches sur les méthodes de dé-convolution pour améliorer la résolution du volume réel 3D US et rendre la structure des micro-outils clairs.

Sur cette étape, la sonde mécanique 2D est utilisée pour obtenir les volumes ultrasonores 3D. Le temps moyen pour générer un volume prend quelques secondes. Cela réduit l'avantage du temps réel pour les systèmes ultrasonores. Afin de satisfaire les demandes en temps réel, la technologie d'imagerie rapide devrait également être mis en œuvre dans le système commercial pour obtenir un taux de volume élevé, par exemple, en utilisant des sondes matricielles à générer des volumes ultrasonores en 3D est beaucoup plus rapide que 2D sondes mécaniques.

La nouvelle technologie de détection d'enveloppe peut aussi être mise en œuvre pour améliorer le contraste entre l'aiguille de biopsie et le tissu de fond. Un cadre algébrique des signaux analytiques 3D ont été proposées dans [Wang *et al.* (2012)]. Leurs résultats montrent que la technologie de détection d'enveloppe 3D fonctionne mieux que le résultat de l'enveloppe 1D traditionnelle (transformée de Hilbert).

À cause du bruit électronique, parfois la méthode de mise en correspondance de bloc ne peut pas trouver la bonne région pour s'adapter à la région du noyau, ce qui induit une erreur dans l'estimation de mouvement ainsi perdu la cible. Une meilleure méthode peut être appliquée afin d'améliorer le résultat de l'estimation de mouvement. Par exemple, l'algorithme de mean shift est avéré être la simplicité et l'efficacité dans les visions par ordinateur [Ning *et al.* (2012)]. Il pourrait être mise en œuvre pour suivre la pointe de l'aiguille dans la série de volumes 3D ultrasonores.

Appendix

A. Online demonstration of 2D ROI-RK algorithm

Ultrasound Advanced Open Platform (ULA-OP) is a system developed by the MSD-Lab of Florence University. This system is designed to allow the test of new ultrasound (US) methods including original bean forming strategies, real-time image processing, pulsed Doppler, etc. The real time application of 2D ROI-RK algorithm is based on this system.

Localization methods

In this application, the ROI-RK method is implemented and when connecting with the ULA-OP, it can locate and track the needle inserted in a phantom in real time. The 2D **AxShp** and **SegShp** tool model have been implemented.

The advantages of these two tool models are no parameters learning procedures are needed during the tracking procedure.

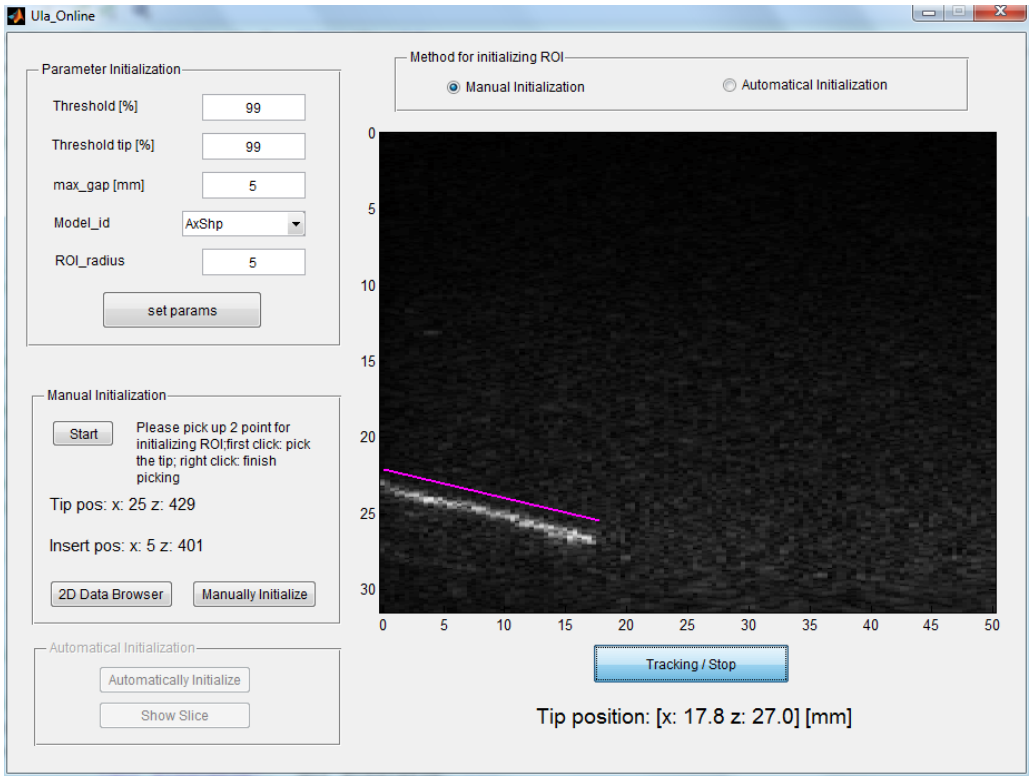

Figure 1 The GUI on-line for needle localization in MATLAB. Note that the pink line represents the position detected. To well observe the original position of the needle and the detected position, a deviation of 1.5 mm of the horizontal direction has been voluntarily added.

Software implementation

This application is implemented using MATLAB. A real time application module of ULA-OP is implemented in the source codes. This module helps to get the original data from the system ULA-OP. The whole implementation is based on the MATLAB GUI and it is user friendly.

How to use

The applied GUI of ULA-Online has a main window, and it is separated in 3 parts: the Parameter Initialization part, the ROI Initialization part and the result part. To begin the application, we should first set the parameters for the ROI-RK method. The original parameters are the proposed ones, while the users can change them as needed.

After the parameters are initialized, the users can initialize the ROI by two methods: manual initialization or automatical initialization. With the manual initialization, when click the button “Start”, a real time image containing the needle will appeared in a new window. Through left clicking on the image, we can pick two points who present the tip point and the insert point of the needle. The right click finishes the points picking. Then, on clicking the button “Initialize”, the ROI will be automatically set according to the points chosen. With the automatically initialization, on clicking the button “Automatically initialize”, the algorithm will initialize the ROI automatically without any manual part and the initialized result will be shown at the right image part.

After the ROI is initialized, we can use the ROI-RK algorithm to detect and track the position of the needle. The “Tracking / Stop” button can start and end the algorithm loop. The pink line shown on the result image illustrates the position of the needle. Note that in order to well observe the original position of the needle and the detected position, a deviation of 1.5 mm of the horizontal direction has been voluntarily added. Below the button, it shows the needle tip position under the Cartesian coordinate.

B. AxShp model and IndDstr model for RANSAC algorithm

These two models have been proposed in [Uherčík (2011)].

Model AxShp

This model only evaluates the distances of the voxels $M(x,y,z) \in V_{th}$ to the estimated line $l(t;\mathbf{A})$. This model does not need any a priori information on the intensity values. A classifier function $q_{Ax}(M;\mathbf{A}) \in \{0,1\}$ is defined as

$$q_{Ax}(M;\mathbf{A}) = \begin{cases} 1, & \text{if } d(M;\mathbf{A}) < r \\ 0, & \text{otherwise} \end{cases} \quad (1)$$

r is the expected radius of the needle in the image. The point to curve distance d is defined as the Euclidean distance from the point M and its projection on the line $l(t;\mathbf{A})$. To simplify the calculation of the point-to curve distance d, the following approximation is used:

$$d(M;\mathbf{A}) = \left\| M - l(t;\mathbf{A}) \right\|, \; t = \frac{(M - N_1)\mathbf{u}}{\|\mathbf{u}\|} \quad (2)$$

Here, $\mathbf{u}$ is the principal direction of the line $l(t;\mathbf{A})$. All the voxels satisfying $q_{Ax}(M;\mathbf{A}) = 1$ are called the inliers V_{inl}, the other records are outliers. To evaluate the fitness of the inliers V_{inl} with respect to $l(t;\mathbf{A})$, a cost function is defined as

$$C(V_{inl};\mathbf{A}) = \sum_{M \in V_{inl}} d(M;\mathbf{A}) \quad (3)$$

Once $l(t;\mathbf{A})$ is chosen, $C(V_{inl};\mathbf{A})$ is calculated. According to the value of cost function, the best-fitting model can be chosen. This best value is used in the step of optimization.

Model IntDstr

This model not only use the position information of voxel M, but also the prior information about the intensity distribution of the voxels located near the needle. This model is based on an estimated likelihood $p(d,i|bg)$ of the observation of a voxel M with an intensity $i = I(M)$ at the distance d from the estimate axis $l(t;\mathbf{A})$, with the different group g: needle (*nd* for short) and background (*bg* for short). We assume that the probability of a voxel to be the needle or the background is the same, namely $p(nd) = p(bg)$, and the classification function q is set as:

$$q_{IntDstr}(M;\mathbf{A}) = \begin{cases} 1, & if\ p(d,i|nd) \geq p(d,i|bg) \\ 0, & \text{otherwise} \end{cases} \quad (4)$$

We suppose that the observations of the voxels are independent, and the cost function of this model $C(\mathbf{A})$ is set as a negative logarithmic likelihood of the observation the inlier set V_{inl} with a given position:

$$C_{IntDstr}(V_{inl};\mathbf{A}) = \sum_{M \in V_{inl}} -\log p(d,i|nd) \quad (5)$$

The likelihood $p(d,i|nd)$ is calculated as following

$$p(d,i|nd) = p(i|d,nd)\,p(d|nd) \quad (6)$$

where $p(d|nd)$ obeys the positive part of a normal distribution with zero mean and variance σ, which corresponds to the expected radius of the needle in the volume. The background intensity distribution $p(d,i|bg)$ is supposed to be spatially independent as:

$$p(d,i|bg) = p(i|bg) \quad (7)$$

$p(i|d,nd)$ and $p(i|bg)$ are estimated from a training set of US volumes with a known ground truth. The estimation steps are as below: a). the needle voxels are collected into *m* uniform bins with the step Δd, as $b_j = [j\Delta d,(j+1)\Delta d]$; b) because the Gamma distribution is sufficient to approximate the real distribution in the US image and it is successfully used for US images generating in [Barva (2007)] and [Tao *et al.* (2003)]. The distribution of $p(i|bg)$ and $p(i|d \in b_j,nd)$, $j = 0,\ldots m$ are modeled as Gamma distribution $\Gamma_{k_{bg},\theta_{bg}}$ and Γ_{k_j,θ_j} respectively; c) determining the parameters σ, k_{bg},θ_{bg} and k_j,θ_j using maximum likelihood estimates [Choi *et al.* (1969)].

Publications

Journal article

Y. Zhao, C. Cachard, H. Liebgott, *Automatic Needle Detection and Tracking in 3D Ultrasound Using an ROI-based RANSAC and Kalman Method*, Ultrasonic Imaging, 2013, Vol. 35 (4), pp 283 – 306.

M. Uherčík, J. Kybic, **Y. Zhao** (Corresponding author), C. Cachard, H. Liebgott, *Line Filter for Surgical Tool Localization in 3D Ultrasound Images*, Computers in Biology and Medicine, 2013, Vol. 43 (12), pp 2036 - 2045.

International conference paper

Y. Zhao, C. Cachard, H. Liebgott, *A New Automatically Biopsy Needle Tracking Method Using 3D Ultrasound*, IEEE - International Ultrasonics Symposium, Prague, Czech Republic, 2013

Y. Zhao, H. Liebgott, C. Cachard, *Tracking Micro Tool in a Dynamic 3D Ultrasound Situation Using Kalman Filter and RANSAC Algorithm*, 9th IEEE International Symposium on Biomedical Imaging (ISBI), 2012: pp 1076 - 1079

Y. Zhao, H. Liebgott, C. Cachard, *Tracking Biopsy Needle Using Kalman Filter and RANSAC Algorithm with 3D Ultrasound*, 11th Proceedings of the Acoustics , Nantes, France, 2012: pp 231 - 236

National communication

Y. Zhao, C. Cachard, H. Liebgott, *ROI-RK: a Fully Automatic and Realtime 3D Needle Guidance Method*, journée SIAM: Signal et Image en Acoustique Médicale, Tours, France, 10 – 11, June, 2013

Bibliography

[Allen *et al.*, (2006)] Allen, P. S. Brady, and T. A. S. Matalon. Ultrasound Guidance in Interventional Radiology. *Contemp. Diagnostic Radiol.*, 2006, vol. 29, no. 3, pp. 2–7

[Angelsen, (2000)] Angelsen. Ultrasound Imaging -- Waves, Signals, and Signal Processing. I. Emantes, 2000, 600 p. ISBN 82-995811-0-9

[Barva, (2007)] Barva. Localization of Surgical Instruments in 3D Ultrasound Images. Ph.D, Czech Technical University, 2007

[Barva *et al.*, (2008)] Barva, M. Uhercik, J.-M. Mari, J. Kybic, J.-R. Duhamel, H. Liebgott, V. Hlavác, and C. Cachard. Parallel Integral Projection Transform for Straight Electrode Localization in 3-D Ultrasound Images. *Ultrason. Ferroelectr. Freq. Control. IEEE Trans.*, 2008, vol. 55, no. 7, pp. 1559–1569

[Bell *et al.*, (2012)] Bell, B. C. Byram, E. J. Harris, P. M. Evans, and J. C. Bamber. In Vivo Liver Tracking with a High Volume Rate 4D Ultrasound Scanner and a 2D Matrix Array Probe. *Phys. Med. Biol.*, 2012, vol. 57, no. 5, pp. 1359–74

[Bradley, (2001)] Bradley. An In-Vitro Study to Understand Successful Free-Hand Ultrasound Guided Intervention. 2001, pp. 495–498

[Building, (2000)] Building. Speckle Tracking for Multi-Dimensional Flow Estimation. *Ultrasonics*, 2000, vol. 38, pp. 369–375

[Burckhardt, (1978)] Burckhardt. Speckle in Ultrasound B-Mode Scans. *IEEE Trans. Sonics Ultrason.*, 1978, vol. 25, no. 1, pp. 1–6

[Burges, (1998)] Burges. A Tutorial on Support Vector Machines for Pattern Recognition. *Data Min. Knowl. Discov.*, 1998, vol. 2, no. 2, pp. 121–167

[Caliano *et al.*, (2005)] Caliano, R. Carotenuto, E. Cianci, V. Foglietti, A. Caronti, A. Iula, and M. Pappalardo. Design, Fabrication and Characterization of a Capacitive Micromachined Ultrasonic Probe for Medical Imaging. *Ultrason. Ferroelectr. Freq. Control. IEEE Trans.*, 2005, vol. 52, no. 12, pp. 2259–2269

[Chang *et al.*, (1984)] Chang and J. Tabaczynski. Application of State Estimation to Target Tracking. 1984, vol. 29, no. 2, pp. 98–109

[X Chen *et al.*, (2004)] X. Chen, C. Lehman, and E. Dee. MRI-Guided Breast Biopsy: Clinical Experience with 14-Gauge Stainless Steel Core Biopsy Needle. *Am. J. Roentgenol.*, 2004, vol. 182, no. 4, pp. 1075–1080

[Z Chen, (2003)] Z. Chen. Bayesian Filtering : From Kalman Filters to Particle Filters , and Beyond. *Statistics (Ber).*, 2003, vol. 182, no. 1, pp. 1 – 69

[KJ Chin, (2012)] K. J. Chin. Utrasound Guided Needle Insertion and Injection Skills. *9th Annual International Symposium of Ultrasound for Regional Anesthesia and Pain Medicine (ISURA)*, 2012. 2012, pp. 1–8

[K Chin *et al.*, (2008)] K. Chin, a Perlas, V. Chan, and R. Brull. Needle Visualization in Ultrasound-Guided Regional Anesthesia: Challenges and Solutions. *Reg. Anesth. Pain Med.*, 2008, vol. 33, no. 6, pp. 532–544

[Choi *et al.*, (1969)] Choi and R. Wette. Maximum Likelihood Estimation of the Parameters of the Gamma Distribution and Their Bias. *Technometrics*, 1969, vol. 11, no. 4, pp. 683 – 690

[Crow, (1984)] Crow. Summed Area Tables for Texture Mapping. *Comput. Graph. SIGGRAPH Proc.*, 1984, vol. 11, no. 3, pp. 200–220

[Diarra *et al.*, (2013)] Diarra, M. Robini, P. Tortoli, C. Cachard, and H. Liebgott. Design of Optimal 2-D Non-Grid Sparse Arrays for Medical Ultrasound. *Biomed. Eng. IEEE Trans.*, 2013, vol. 60, no. 11, pp. 3093–3102

[Dimaio *et al.*, (2003)] Dimaio and S. E. Salcudean. Needle Steering and Model-Based Trajectory. 2003, pp. 33–40

[Ding *et al.*, (2003)] Ding and A. Fenster. A Real-Time Biopsy Needle Segmentation Technique Using Hough Transform. *Med. Phys.*, 2003, vol. 30, no. 8, pp. 2222–2233

[Draper *et al.*, (2000)] Draper, C. C. Blake, L. Gowman, D. B. Downey, and A. Fenster. An Algorithm for Automatic Needle Localization in Ultrasound-Guided Breast Biopsies. *Med. Phys.*, 2000, vol. 27, no. 8, pp. 1971–1979

[Duboeuf *et al.*, (2009)] Duboeuf, A. Basarab, H. Liebgott, E. Brusseau, P. Delachartre, and D. Vray. Investigation of PVA Cryogel Young's Modulus Stability with Time, Controlled by a Simple Reliable Technique. *Med. Phys.*, 2009, vol. 36, no. 2, pp. 656–661

[Duda *et al.*, (2001)] Duda, P. E. Hart, and D. G. Stork. Pattern Classification. Second. Wiley Interscience, 2001,

[Dutt, (1995)] Dutt. Statistical Analysis of Ultrasound Echo Envelope. The Mayo Graduate School, Rochester, MN, 1995, 197 p.

[Fenster *et al.*, (2001)] Fenster, D. B. Downey, and H. N. Cardinal. Three-Dimensional Ultrasound Imaging. *Phys. Med. Biol.*, 2001, vol. 46, no. 5, pp. R67–99

[Fischler *et al.*, (1981)] Fischler and R. C. Bolles. Random Sample Consensus: a Paradigm for Model Fitting with Applications to Image Analysis and Automated Cartography. *Commun. ACM*, 1981, vol. 24, no. 6, pp. 381–395

[Florack *et al.*, (1992)] Florack, B. M. ter Haar Romeny, J. J. Koenderink, and M. a Viergever. Scale and the Differential Structure of Images. *Image Vis. Comput.*, 1992, vol. 10, no. 6, pp. 376–388

[Franc *et al.*, (2009)] Franc and S. Sonnenburg. Optimized Cutting Plane Algorithm for Large-Scale Risk Minimization. *J. Mach. Learn. Res.*, 2009, vol. 10, pp. 2157–2192

[Frangi *et al.*, (1998)] Frangi, W. J. Niessen, K. L. Vincken, and M. A. Viergever. Multiscale Vessel Enhancement Filtering. *Medical Image Computing and Computer-Assisted Interventation—MICCAI'98*, 1998. 1998, pp. 130–137

[Freund *et al.*, (1997)] Freund and R. Schapire. A Desicion-Theoretic Generalization of on-Line Learning and an Application to Boosting. *Comput. Syst. Sci.*, 1997, vol. 55, pp. 119–139

[Fronheiser *et al.*, (2008)] Fronheiser, S. F. Idriss, P. D. Wolf, and S. W. Smith. Vibrating Interventional Device Detection Using Real-Time 3-D Color Doppler. *Ultrason. Ferroelectr. Freq. Control. IEEE Trans.*, 2008, vol. 55, no. 6, pp. 1355–1362

[Gallant, (1990)] Gallant. Perceptron-Based Learning Algorithms. *Neural Networks, IEEE Trans.*, 1990, vol. 1, no. 2, pp. 179–191

[Hall *et al.*, (1999)] Hall, A. Martin, H. Liu, E. Nussbaum, R. Maxwell, and C. Truwit. Brain Biopsy Using High-Field Strength Interventional Magnetic Resonance Imaging. *Neurosurgery*, 1999, vol. 44, no. 4, pp. 807–813

[Hartmann *et al.*, (2009)] Hartmann, M. Baumhauer, J. Rassweiler, and H.-P. Meinzer. Automatic Needle Segmentation in 3D Ultrasound Data Using a Hough Transform Approach. *Bild. Für Die Medizin 2009*, 2009, vol. 37, no. 2, pp. 341–345

[Haykin, (2003)] Haykin. Adaptive Filter Theory. Fouth edit. Prentice Hall, New York, 2003,

[Hong *et al.*, (2004)] Hong, T. Dohi, M. Hashizume, K. Konishi, and N. Hata. An Ultrasound-Driven Needle-Insertion Robot for Percutaneous Cholecystostomy. *Phys. Med. Biol.*, 2004, vol. 49, no. 3, pp. 441–55

[Jensen, (1996)] Jensen. Field: A Program for Simulating Ultrasound Systems. *Conf. Biomed. IMAGING, VOL. 4,*, 1996, vol. 34, pp. 351– 353

[Jensen, (2001)] Jensen. Users' Guide for the Field II Program, 2001

[Jensen *et al.*, (1992)] Jensen and N. B. Svendsen. Calculation of Pressure Fields from Arbitrarily Shaped, Apodized, and Excited Ultrasound Transducers. *IEEE Trans. Ultrason. Ferroelectr. Freq. Control*, 1992, vol. 39, no. 2, pp. 262–267

[Joachims, (1999)] Joachims. Making Large-Scale SVM Learning Practical, in *Advances in Kernel methods - Support Vector Learning*, 1999, pp. 41–56

[Jolliffe, (2002)] Jolliffe. Principal Component Analysis. 2nd Ed. New York: Springer, 2002, 1–6 p. ISBN 978-0-387-95442-4

[Kalman, (1960)] Kalman. A New Approach to Linear Filtering and Prediction Problems. *Trans. ASME--Journal Basic Eng.*, 1960, vol. 82, no. Series D, pp. 35–45

[Krupa *et al.*, (2002)] Krupa, M. De Mathelin, C. Doignon, J. Gangloff, G. Morel, L. Soler, J. Leroy, and J. Marescaux. Automatic 3-d Positioning of Surgical

Instruments During Robotized Laparoscopic Surgery Using Automatic Visual Feedback. *Medical Image Computing and Computer-Assisted Intervention—MICCAI 2002*, 2002. 2002, pp. 9–16

[Kultanen *et al.*, (1990)] Kultanen, L. Xu, and E. Oja. Randomized Hough Transform (RHT). *Pattern Recognition, 1990. Proceedings., 10th International Conference On*, 1990. 1990, pp. 631–635 vol.1

[Lewis, (1995)] Lewis. Fast Normalized Cross-Correlation. *Vision Interface*, 1995. 1995, pp. 120–123

[Li *et al.*, (2003)] Li, S. Sone, and K. Doi. Selective Enhancement Filters for Nodules, Vessels, and Airway Walls in Two-and Three-Dimensional CT Scans. *Med. Phys.*, 2003, vol. 30, p. 2040

[Lindseth *et al.*, (2013)] Lindseth, T. Langø, T. Selbekk, R. Hansen, I. Reinertsen, C. Askeland, O. Solheim, G. Unsgård, R. Mårvik, and T. A. N. Hernes. Ultrasound-Based Guidance and Therapy,, in *Advancements and Breakthroughs in Ultrasound Imaging*, GUNARATHNE 2013, pp. 28–82

[Mari *et al.*, (2011)] Mari and C. Cachard. Ultrasonic Scanning of Straight Micro Tools in Soft Biological Tissues: Methodology and Implementation. *Ultrasonics*, 2011, vol. 51, no. 5, pp. 632–8

[Maybeck, (1979)] Maybeck. Stochastic Models, Estimation, and Control. New York: Academic Press, 1979, 1–423 p.

[Nelder *et al.*, (1965)] Nelder and R. Mead. A Simplex Method for Function Minimization.pdf. *Comput. J.*, 1965, vol. 7, no. 4, pp. 308–313

[Nichols *et al.*, (2003)] Nichols, L. B. Wright, T. Spencer, and W. C. Culp. Changes in Ultrasonographic Echogenicity and Visibility of Needles with Changes in Angles of Insonation. *J. Vasc. Interv. Radiol.*, 2003, vol. 14, no. 12, pp. 1553–1557

[Ning *et al.*, (2012)] Ning, L. Zhang, D. Zhang, and C. Wu. Robust Mean-Shift Tracking with Corrected Background-Weighted Histogram. *IET Comput. Vis.*, 2012, vol. 6, no. 1, p. 62

[Novell *et al.*, (2009)] Novell, M. Legros, N. Felix, and A. Bouakaz. Exploitation of Capacitive Micromachined Transducers for Nonlinear Ultrasound Imaging. *Ultrason. Ferroelectr. Freq. Control. IEEE Trans.*, 2009, vol. 56, no. 12, pp. 2733–2743

[Novotny *et al.*, (2003)] Novotny, J. Cannon, and R. Howe. Tool Localization in 3D Ultrasound Images. *Medical Image Computing and Computer-Assisted Intervention - MICCAI 2003 6th International Conference, Montréal, Canada*, 2003. 2003, pp. 969–970

[Novotny *et al.*, (2007)] Novotny, J. A. Stoll, N. V Vasilyev, P. J. Del Nido, P. E. Dupont, and R. D. Howe. GPU Based Real-Time Instrument Tracking with

Three-Dimensional Ultrasound. *Med. Image Anal.*, 2007, vol. 11, no. 5, pp. 458–464

[Ohno *et al.*, (2003)] Ohno, H. Hatabu, D. Takenaka, T. Higashino, H. Watanabe, C. Ohbayashi, and K. Sugimura. CT-Guided Transthoracic Needle Aspiration Biopsy of Small (≤ 20 Mm) Solitary Pulmonary Nodules. *Am. J. Roentgenol.*, 2003, vol. 180, no. 6, pp. 1665–1669

[Plecha *et al.*, (1997)] Plecha, D. W. Goodwin, D. Y. Rowland, M. E. Varnes, and J. R. Haaga. Liver Biopsy: Effects of Biopsy Needle Caliber on Bleeding and Tissue Recovery. *Radiology*, 1997, vol. 204, no. 1, pp. 101–104

[Qiu *et al.*, (2008)] Qiu, M. Ding, and M. Yuchi. Needle Segmentation Using 3D Quick Randomized Hough Transform. *Intelligent Networks and Intelligent Systems, 2008. ICINIS'08. First International Conference On*, Nov.2008. 2008, pp. 449–452

[Roberts, (1988)] Roberts. A New Representation for a Line. *Computer Vision and Pattern Recognition, 1988. Proceedings CVPR '88., Computer Society Conference On*, 1988. 1988, pp. 635–640

[Robinson *et al.*, (1982)] Robinson, F. Chen, and L. S. Wilson. Measurement of Velocity of Propagation from Ultrasonic Pulse-Echo Data. *Ultrasound Med. Biol.*, 1982, vol. 8, no. 4, pp. 413–420

[Rotemberg *et al.*, (2011)] Rotemberg, M. Palmeri, S. Rosenzweig, S. Grant, D. Macleod, and K. Nightingale. Acoustic Radiation Force Impulse (ARFI) Imaging-Based Needle Visualization. *Ultrason. Imaging*, 2011, vol. 33, no. 1, pp. 1–16

[Sato *et al.*, (1998)] Sato, S. Nakajima, N. Shiraga, H. Atsumi, S. Yoshida, T. Koller, G. Gerig, and R. Kikinis. Three-Dimensional Multi-Scale Line Filter for Segmentation and Visualization of Curvilinear Structures in Medical Images. *Med. Image Anal.*, 1998, vol. 2, no. 2, pp. 143–168

[Schapire *et al.*, (1999)] Schapire and Y. Singer. Improved Boosting Algorithms Using Confidence-Rated Predictions. *Mach. Learn.*, 1999, vol. 37, no. 3, pp. 297–336

[Smith *et al.*, (1991)] Smith, H. G. J. Pavy, and O. T. Von Ramm. High-Speed Ultrasound Volumetric Imaging System. I. Transducer Design and Beam Steering. *Ultrason. Ferroelectr. Freq. Control. IEEE Trans.*, 1991, vol. 38, no. 2, pp. 100–108

[Sochman *et al.*, (2005)] Sochman and J. Matas. WaldBoost — Learning for Time Constrained Sequential Detection. *Computer Vision and Pattern Recognition, 2005. CVPR 2005. IEEE Computer Society Conference On*, 2005. 2005, pp. 150–156

[Stoer *et al.*, (1993)] Stoer, R. Bulirsch, R. Bartels, W. Gautschi, and C. Witzgall. Introduction to Numerical Analysis. New York: Springer, 1993,

[Suzuki, (2012)] Suzuki. Pixel-Based Machine Learning in Medical Imaging. *Int. J. Biomed. Imaging*, 2012, vol. 2012, p. 792079

[Svoboda *et al.*, (2007)] Svoboda, J. Kybic, and V. Hlavac. Image Processing, Analysis & and Machine Vision-A MATLAB Companion. First edit. Thomson Learning, 2007,

[Szabo, (2004)] Szabo. Diagnostic Ultrasound Imaging: Inside Out. Elsevier, 2004, 213–220 p.

[Tao *et al.*, (2003)] Tao, C. C. Jaffe, and H. D. Tagare. Tunnelling Descent: A New Algorithm for Active Contour Segmentation of Ultrasound Images, in *Information processing in medical imaging*, Springer, 2003, pp. 246 – 257

[Tommasi *et al.*, (2010)] Tommasi and T. Deselaers. The Medical Image Classification Task, in *ImageCLEF --Experimental Evaluation in Visual Information Retrieval*, 2010, pp. 221–238

[Torr *et al.*, (1998)] Torr, a Zisserman, and S. . Maybank. Robust Detection of Degenerate Configurations While Estimating the Fundamental Matrix. *Comput. Vis. Image Underst.*, 1998, vol. 71, no. 3, pp. 312–333

[Trahey *et al.*, (1987)] Trahey, J. W. Allison, and O. T. Von Ramm. Angle Independent Ultrasonic Detection of Blood Flow. *IEEE Trans. Biomed. Eng.*, 1987, vol. 34, no. 12, pp. 965–967

[Uherčík, (2011)] Uherčík. Surgical Tools Localization in 3D Ultrasound Images. Ph.D, Czech Technical University, 2011

[Uherčík *et al.*, (2009)] Uherčík, J. Kybic, C. Christian, and H. Liebgott. Line Filtering for Detection of Microtools in 3D Ultrasound Data. *IEEE International Ultrasonics Symposium*, 2009. 2009, pp. 594–597

[Uherčík *et al.*, (2008)] Uherčík, J. Kybic, H. Liebgott, and C. Cachard. Multi-Resolution Parallel Integral Projection for Fast Localization of a Straight Electrode in 3D Ultrasound Images. *Biomedical Imaging: From Nano to Macro, 2008. ISBI 2008. 5th IEEE International Symposium On*, 2008. 2008, pp. 33–36

[Uherčík *et al.*, (2010)] Uherčík, J. Kybic, H. Liebgott, and C. Cachard. Model Fitting Using RANSAC for Surgical Tool Localization in 3-D Ultrasound Images. *Biomed. Eng. IEEE Trans.*, 2010, vol. 57, no. 8, pp. 1907–1916

[Uherčík *et al.*, (2013)] Uherčík, J. Kybic, Y. Zhao, C. Cachard, and H. Liebgott. Line Filtering for Surgical Tool Localization in 3D Ultrasound Images. *Comput. Biol. Med.*, 2013, vol. 43, no. 12, pp. 2036–2045

[Wang *et al.*, (2012)] Wang, P. R. Girard, A. Bernard, Z. Liu, P. Clarysse, and P. Delachartre. 3-D BIQUATERNIONIC ANALYTIC SIGNAL AND APPLICATION TO ENVELOPE DETECTION IN 3-D ULTRASOUND IMAGING. *3D Imaging (IC3D), International Conference On*, 2012. 2012, pp. 1 – 8

[Wei *et al.*, (2005)] Wei, M. Ding, D. Downey, and A. Fenster. 3D TRUS Guided Robot Assisted Prostate Brachytherapy. *Medical Image Computing and Computer-Assisted Intervention--MICCAI 2005*, Jan.2005. 2005, pp. 17–24

[Wei *et al.*, (2004)] Wei, L. Gardi, D. B. Downey, and A. Fenster. Oblique Needle Segmentation for 3D TRUS-Guided Robot-Aided Transperineal Prostate Brachytherapy. *Biomedical Imaging Nano to Macro, IEEE International Symposium On*, 2004. 2004, pp. 960–963

[BL Welch, (1947)] B. L. Welch. The Generalization Ofstudent's' Problem When Several Different Population Variances Are Involved. *Biometrika*, 1947, vol. 34, no. 1/2, pp. 28–35

[G Welch *et al.*, (2006)] G. Welch and G. Bishop. An Introduction to the Kalman Filter, Department of Computer Science; University of North Carolina at Chapel Hill, Chapel Hill, 2006, 16 p.

[Zhao *et al.*, (2013)] Zhao, C. Cachard, and H. Liebgott. Automatic Needle Detection and Tracking in 3D Ultrasound Using an ROI-Based RANSAC and Kalman Method. *Ultrason. Imaging*, 2013

[Zhou *et al.*, (2007)] Zhou, W. Qiu, M. Ding, and S. Zhang. Automatic Needle Segmentation in 3D Ultrasound Images Using 3D Hough Transform. *SPIE 5th International Symposium on Multispectral Image Processing and Pattern Recognition*, 2007. 2007, p. 6789: 67890R

[Zhou *et al.*, (2008)] Zhou, W. Qiu, M. Ding, and S. Zhang. Automatic Needle Segmentation in 3D Ultrasound Images Using 3D Improved Hough Transform. *Med. Imaging 2008 Vis. Image-Guided Proced. Model. Proc. SPIE*, 2008, vol. 6918, no. 2008, pp. 691821–691821–9

FOLIO ADMINISTRATIF
THESE SOUTENUE DEVANT L'INSTITUT NATIONAL DES SCIENCES APPLIQUEES DE LYON

NOM : ZHAO DATE de SOUTENANCE : 05/02/2014
(avec précision du nom de jeune fille, le cas échéant)
Prénoms : Yue

TITRE : Biopsy Needles Localization and Tracking Methods in 3D Medical Ultrasound with ROI-RANSAC-KALMAN

NATURE : Doctorat Numéro d'ordre : 2014-ISAL-0015

École doctorale : École Doctorale Mécanique, Énergétique, Génie Civil, Acoustique (MEGA)

Spécialité : Images et Systèmes

RESUME :

In medical examinations and surgeries, minimally invasive technologies are getting used more and more often. Some specially designed surgical instruments, like biopsy needles or electrodes are operated by radiologists or robotic systems and inserted in human's body for extracting cell samples or deliver radiation therapy. To reduce the risk of tissue injury and facilitate the visual tracking, some medical vision assistance systems, for example, ultrasound (US) systems have been used during the surgical procedure.

Due to the strong speckle noise of US images and the large calculation load involved as soon as 3D data are involved, it is a challenge to locate the biopsy needle accurately and tracking its position in real time in 3D US. In order to solve the two main problems above, we proposed a region of interest (ROI) based RANSAC and Kalman (RK) method to robustly localize and track the position of the biopsy needle in real time.

The ROI-RK method consists of two steps: the initialization step and the tracking step. In the first step, a ROI initialization strategy using Hessian based line filter measurement is implemented. This step can efficiently suppress the speckle noise of the ultrasound volume, and enhance line-like structures as biopsy needles. In the second step, after the ROI is initialized, a tracking loop begins. The RK algorithm can robustly localize and track the biopsy needles in a dynamic situation. The RANSAC algorithm is used to estimate the position of the micro-tools and the Kalman filter helps to update the ROI and auto-correct the needle localization result. Because the ROI-RK method is involved in a dynamic situation, a motion estimation strategy is also implemented to estimate the insertion speed of the biopsy needle.

3D US volumes with inhomogeneous background have been simulated to verify the performance of the ROI-RK method. The method has been tested under different conditions, such as inserting orientations angles, and contrast ratio (CR). The localization accuracy is within 1 mm no matter what the inserting direction is. Only when the CR is very low, the proposed method could fail to track because of an incomplete ultrasound imaging of the needle.

Another methodology, i.e. RANSAC with machine learning (ML) algorithm has been presented. This method aims at classifying the voxels not only depending on their intensities, but also the structure features of the biopsy needle. The simulation results show that the RANSAC with ML algorithm can separate the needle voxels and background tissue voxels with low CR.

MOTS-CLES : 3D, ultrasound, biopsy needle, Kalman, RANSAC, speckle tracking, classification, machine learning

Laboratoire (s) de recherche : CREATIS (CNRS UMR 5220, INSERM U1044)
Directeur de thèse: Christian CACHARD / Hervé LIEBGOTT
Président de jury :
Composition du jury :

Co-directeurs de thèse:
Christian CACHARD, Professeur des Universités, Université Claude Bernard, Lyon I
Hervé LIEBGOTT, Maître de Conférences, HDR, Université Claude Bernard, Lyon I

Rapporteurs:
Pascal HAIGRON, Professeur des Universités, Université de Rennes I
Jean-Marc GIRAULT, Maître de Conférences, HDR Université François-Rabelais, Tours

Examinateurs:
Didier VRAY, Professeur des Universités, INSA de Lyon
Laurent SARRY, Professeur des Universités, Université Clermont-Ferrand